




# Paired Explicit Relaxation Runge-Kutta Methods: Entropy-Conservative and Entropy-Stable High-Order Optimized Multirate Time Integration

Daniel Doehring <sup>a,\*</sup>, Hendrik Ranocha <sup>b</sup>, and Manuel Torrilhon <sup>a</sup>

<sup>a</sup>*Applied and Computational Mathematics, RWTH Aachen University, Germany.*

<sup>b</sup>*Institute of Mathematics, Johannes Gutenberg University Mainz, Germany.*

---

## Abstract

We present novel entropy-conservative and entropy-stable multirate Runge-Kutta methods based on Paired Explicit Runge-Kutta (P-ERK) schemes with relaxation for conservation laws and related systems of partial differential equations. Optimized schemes up to fourth-order of accuracy are derived and validated in terms of order of consistency, conservation of linear invariants, and entropy conservation/stability. We demonstrate the effectiveness of these P-ERRK methods when combined with a high-order, entropy-conservative/stable discontinuous Galerkin spectral element method on unstructured meshes. The Paired Explicit *Relaxation* Runge-Kutta methods (P-ERRK) are readily implemented for partitioned semidiscretizations arising from problems with equation-based scale separation such as non-uniform meshes. We highlight that the relaxation approach acts as a time-limiting technique which improves the nonlinear stability and thus robustness of the multirate schemes. The P-ERRK methods are applied to a range of problems, ranging from compressible Euler over compressible Navier-Stokes to the visco-resistive magnetohydrodynamics equations in two and three spatial dimensions. For each test case, we compare computational load and runtime to standalone relaxed Runge-Kutta methods which are outperformed by factors up to four. All results can be reproduced using a publicly available repository.

**Keywords:** Entropy Stability, Multirate Time Integration, Runge-Kutta Methods, Method of Lines, High-Order

**2008 MSC:** 65L06, 65M20, 76-04, 70K20

---

## 1. Introduction

The concept of entropy is of pivotal importance in both analysis and numerical discretization of hyperbolic conservation laws and related systems of partial differential equations (PDEs). This insight dates back to the seminal works by Oleĭnik [1], Lax [2], and Kružkov [3] who realized that entropy provides the sought guidance to resolve the non-uniqueness issue caused by shocks. Employing entropy principles allowed the aforementioned authors to answer questions originally raised by Riemann, Rankine, and Hugoniot which remained open for more than 70 years. Besides being an indispensable tool for the analysis of conservation laws [4, 5], entropy is at its heart a physical, thermodynamic quantity. All physical processes are irreversible, i.e., carry an inherent direction and thus lead to an increase of the physical entropy. A prominent example from hydrodynamics is the entropy increase across shocks [6]. Another notoriously complicated hydrodynamic feature are scale-spanning turbulent flows which continue to challenge various branches of science and engineering. Recent studies on entropy-conservative/entropy-stable (EC/ES) numerical schemes [7–11] have shown how EC/ES schemes can be used to obtain more

---

\*Corresponding author

robust simulations for under-resolved turbulent flows. Thus, to accurately simulate such and even more intricate phenomena, entropy can and should be employed as a guiding principle in addition to the traditional balance laws governing mass, momentum, and energy.

The construction of EC/ES finite volume schemes has been pioneered by Tadmor [12, 13] and was since then extended to a variety of high-order accurate discretization schemes, see for instance [14–17] and references therein. In this work we focus on the discontinuous Galerkin spectral element method (DGSEM) method, i.e., a nodal Discontinuous Galerkin (DG) method [18] with spatially collocated interpolation/quadrature points [19, 20]. These in principle arbitrarily high-order accurate schemes achieve entropy conservation/stability by computing the volume integral with summation-by-parts (SBP) operators and flux-differencing techniques [7, 15, 16, 21, 22]. In addition, to conserve entropy, inviscid surface flux functions [23–26] must be used. Entropy stability however, i.e., monotone decay of the mathematical entropy, is guaranteed for instance by standard dissipative Lax-Friedrichs type surface fluxes [27].

In the previous paragraph we briefly outlined the building blocks of an EC/ES *spatial* discretization. To obtain a (fully) discrete EC/ES scheme for an unsteady problem, it remains to discretize the *temporal* derivative in a way that preserves this property. Examples of EC/ES space-time methods can be found in [28–30]. If the method of lines (MoL) technique [31] is employed, different techniques to ensure the conservation of nonlinear functionals of the ordinary differential equation (ODE) system (such as the mathematical entropy) need to be employed. Options for this are projection-based methods [32, Chapter IV.4], [33–35], the incremental direction technique (IDT) [36], or the relaxation methodology developed in [37, 38]. As pointed out in [39–41], a relaxation approach to ensure conservation of energy and other quadratic invariants was already proposed in [42, 43]. Therein, the authors consider a modified Leapfrog scheme and apply it to the Korteweg–de Vries and nonlinear Schrödinger equation. The relaxation idea was also presented in [44].

In this work we combine the relaxation methodology [37, 38, 41] and the Paired Explicit Runge-Kutta (P-ERK) methods [45–47] to obtain an optimized multirate time integration scheme that is EC/ES, which we accordingly label Paired Explicit Relaxation Runge-Kutta (P-ERRK). The closest related work to the present study is [39], where the authors extend the second-order accurate multirate Runge-Kutta method from [48] with the relaxation methodology. Therein, however, the authors consider besides pure ODEs only the Burgers equation and do not quantify speed-up of the relaxed multirate methods over the baseline relaxed time integration methods. In contrast, we demonstrate in this work speed-up and reduced computational effort for up to fourth-order discretizations of the compressible Navier-Stokes-Fourier, visco-resistive Magnetohydrodynamics (VRMHD) and inviscid Euler equations.

The paper is organized as follows: We begin by briefly sketching out the considered PDE systems, P-ERK methods, the notion of the (global) solution entropy, and the relaxation approach in Section 2. Then, we proceed to the construction of P-ERRK methods in Section 3 which includes a detailed discussion on how the relaxation approach can act as a time-limiting technique to improve the robustness of the multirate scheme. The obtained methods are thoroughly validated in Section 4 where conservation of entropy and linear invariants is demonstrated without impairing the accuracy, i.e., order of consistency, of the schemes. In Section 5, the P-ERRK schemes are applied to a laminar, effectively incompressible flow around the SD7003 airfoil, a Mach 0.5 flow of a visco-resistive magnetized fluid around a cylinder, an inviscid, transonic flows around the NACA0012 airfoil and ONERA M6 wing, and a viscous, transonic flow across the NASA Common Research Model (CRM). For each test case, we demonstrate improved performance of the P-ERRK schemes over single-rate relaxed Runge-Kutta methods. Furthermore, we showcase increased robustness of the relaxed multirate P-ERRK schemes over the standard P-ERK methods, especially for under-resolved simulations. We conclude the paper in Section 6.

## 2. Preliminaries

### 2.1. Scope

In this work we consider PDE systems of the form

$$\mathbf{u}(t_0) = \mathbf{u}_0 \quad (2.1a)$$

$$\partial_t \mathbf{u}(t, \mathbf{x}) + \nabla \cdot \mathbf{f}(\mathbf{u}, \nabla \mathbf{u}) + \mathbf{g}(\mathbf{u}, \nabla \mathbf{u}) = \mathbf{s}(t, \mathbf{x}; \mathbf{u}), \quad t \in [t_0, t_f], \quad \mathbf{x} \in \Omega \subset \mathbb{R}^d \quad (2.1b)$$

where  $\mathbf{u} \in \mathbb{R}^V$  denotes the vector of conserved variables and  $\mathbf{f} \in \mathbb{R}^{V \times d}$  is a flux function which may contain diffusive terms. Nonconservative terms are collected in  $\mathbf{g}$  and  $\mathbf{s}$  is a source term. The classic theory of entropy conservation evolved around hyperbolic conservation laws, i.e., system (2.1) with  $\mathbf{f} = \mathbf{f}(\mathbf{u})$ ,  $\mathbf{g} = \mathbf{s} = \mathbf{0}$ . Examples for entropy conservation problems with non-conservative terms, i.e.,  $\mathbf{g} \neq \mathbf{0}$  are the shallow water equations [49] or the coupled Burgers equation [50]. In the presence of viscous terms, i.e.,  $\mathbf{f} = \mathbf{f}(\mathbf{u}, \nabla \mathbf{u})$  entropy is not conserved, but expected to decay monotonically/stable, assuming suitable boundary conditions.

Here, we employ the DGSEM [18–20] to obtain the semidiscretization of (2.1):

$$\mathbf{U}(t_0) = \mathbf{U}_0 \quad (2.2a)$$

$$\mathbf{U}'(t) = \mathbf{F}(t, \mathbf{U}(t)), \quad \mathbf{U} \in \mathbb{R}^M. \quad (2.2b)$$

The  $M$  unknowns of (2.2) are the nodal DG solution polynomial coefficients. Throughout this work we mainly consider convection-dominated problems, i.e., configurations for which the spectral radius  $\rho_{\mathbf{F}}$  of the Jacobian of the fully discrete system (2.2b)  $J_{\mathbf{F}}(\mathbf{U}) := \frac{\partial \mathbf{F}}{\partial \mathbf{U}}$  scales as

$$\rho \sim \frac{|a|}{h} \gg \frac{|d|}{h^2}, \quad (2.3)$$

where  $h$  denotes the smallest characteristic size of a grid cell, which is for the quadrilaterals and hexahedra considered in this work estimated based on the minimal distance between corner nodes. In (2.3)  $a, d$  are suitable quantifiers for the influence of convection and diffusion, respectively.

### 2.2. Paired Explicit Runge-Kutta Methods

P-ERK methods have been developed in [45] and consecutively extended to third- [46] and fourth-order [47] of consistency. Furthermore, an embedded scheme based on the second-order method has been proposed in [51] which enables error-based timestep control.

The central idea of the P-ERK methods is to pair Runge-Kutta schemes with different domains of stability and computational cost in an efficient way. These schemes belong to the class of Partitioned Runge-Kutta methods (PRKMs) [52–54] and are naturally applicable to semidiscretizations (2.2) which may be partitioned according to different characteristic timescales:

$$\mathbf{U}(t_0) = \mathbf{U}_0, \quad (2.4a)$$

$$\mathbf{U}'(t) = \begin{pmatrix} \mathbf{U}^{(1)}(t) \\ \vdots \\ \mathbf{U}^{(R)}(t) \end{pmatrix}' = \begin{pmatrix} \mathbf{F}^{(1)}(t, \mathbf{U}^{(1)}(t), \dots, \mathbf{U}^{(R)}(t)) \\ \vdots \\ \mathbf{F}^{(R)}(t, \mathbf{U}^{(1)}(t), \dots, \mathbf{U}^{(R)}(t)) \end{pmatrix} = \mathbf{F}(t, \mathbf{U}(t)). \quad (2.4b)$$

Here,  $R$  denotes the number of *partitions/levels*. Based on the local characteristic speed

$$\nu(\mathbf{x}_m) \sim \max_{i=1, \dots, d} \frac{(k+1) \cdot \rho_i(\mathbf{x}_m)}{h(\mathbf{x}_m)} > 0, \quad m = 1, \dots, M \quad (2.5)$$

the unknowns  $\{\mathbf{U}_m\}_{m=1, \dots, M}$  are assigned to different partitions  $r = 1, \dots, R$  which are integrated with different schemes. In (2.5)  $d$  denotes the number of spatial dimensions,  $h$  is a measure for

the smallest characteristic cell size,  $k$  is the DG solution polynomial degree, and  $\rho_i$  is the spectral radius of the Jacobian of the directional flux  $\mathbf{f}_i$ :

$$J_i := \frac{\partial \mathbf{f}_i}{\partial \mathbf{u}} \quad (2.6)$$

cf. (2.1b).

In the following, the superscript  $(\cdot)^{(r)}$  denotes quantities corresponding to the  $r$ 'th partition. These may be a subset of unknowns  $\mathbf{U}^{(r)} \in \mathbb{R}^{M_r}$ , or a method used for solving the corresponding system with right-hand side (RHS)  $\mathbf{F}^{(r)}$ . Note that for the sake of readability we oftentimes pad the vectors  $\mathbf{U}^{(r)}, \mathbf{K}^{(r)} \in \mathbb{R}^{M^{(r)}}$  with zeros to match the dimensionality  $\mathbb{R}^M$  of the full system (2.2). Evaluations of the corresponding RHS  $\mathbf{F}^{(r)}$  are, however, only performed on the actual index set  $M^{(r)}$  with property  $\cup_{r=1}^R M^{(r)} = M$ . ODE systems of the form (2.4) encourage the use of PRKMs, which, in Butcher form, are given by [55, Chapter II.15]

$$\mathbf{U}_0 = \mathbf{U}(t_0), \quad (2.7a)$$

$$\mathbf{K}_i^{(r)} = \mathbf{F}^{(r)} \left( \underbrace{t_n + c_i^{(r)} \Delta t}_{=: t_{n,i}}, \underbrace{\mathbf{U}_n + \Delta t \sum_{j=1}^S \sum_{k=1}^R a_{i,j}^{(k)} \mathbf{K}_j^{(k)}}_{=: \mathbf{U}_{n,i}} \right), \quad i = 1, \dots, S; \quad r = 1, \dots, R \quad (2.7b)$$

$$\mathbf{U}_{n+1} = \mathbf{U}_n + \Delta t \sum_{i=1}^S \sum_{r=1}^R b_i^{(r)} \mathbf{K}_i^{(r)}, \quad (2.7c)$$

where  $S$  denotes the number of stages  $\mathbf{K}_i \in \mathbb{R}^M$ .

When integrating (2.2) with an explicit method, the maximum linearly stable timestep is restricted by some form of the Courant-Friedrichs-Lewy (CFL) condition:

$$\Delta t \stackrel{!}{\leq} \text{CFL} \cdot \min_{\mathbf{x} \in \Omega} \frac{1}{\nu(\mathbf{x})}. \quad (2.8)$$

In contrast to local time-stepping methods [56–62], which reduce the timestep  $\Delta t$  in regions with high characteristic speeds  $\nu(\mathbf{x})$  (2.5), P-ERK schemes increase the CFL stability bound locally to avoid reduction in the global timestep  $\Delta t$ :

$$\Delta t = \text{CFL}^{(r)} \cdot \frac{1}{\nu^{(r)}}, \quad \forall r = 1, \dots, R. \quad (2.9)$$

This is achieved by optimizing the stability polynomials of the composing schemes  $(A^{(r)}, b^{(r)})$  to achieve larger  $\text{CFL}^{(r)}$ . In particular, equipped with the spectrum  $\sigma$  of the Jacobian of the fully-discrete system (2.2)  $J_{\mathbf{F}}$  the stability polynomials  $P^{(r)}(z)$  can be optimized to yield the maximum timestep  $\Delta t$  for this particular spectrum  $\sigma(J_{\mathbf{F}})$  [63, 64]. The key insight here is that the number of free coefficients of the  $P^{(r)}(z)$  stability polynomial is equal to  $E^{(r)} - p$ , where  $E^{(r)}$  denotes the number of stage *evaluations* of the  $r$ -th scheme and  $p$  is the order of the method. Thus, computationally demanding methods with a higher number of stage evaluations  $E^{(r)}$  and larger domain of stability are applied in regions with higher characteristic speeds  $\nu^{(r)}$ , while less expensive methods with a smaller domain of stability are used in regions with lower characteristic speeds  $\nu^{(r)}$ . This concept is schematically illustrated in Fig. 1. Standard, i.e., non-reducible [65, Chapter IV.12] Runge-Kutta methods have  $E = E^{(1)} = S$  stage evaluations, i.e., every stage present in e.g. the Butcher tableau is actually computed and utilized in the final update step or for the computation of subsequent stages.



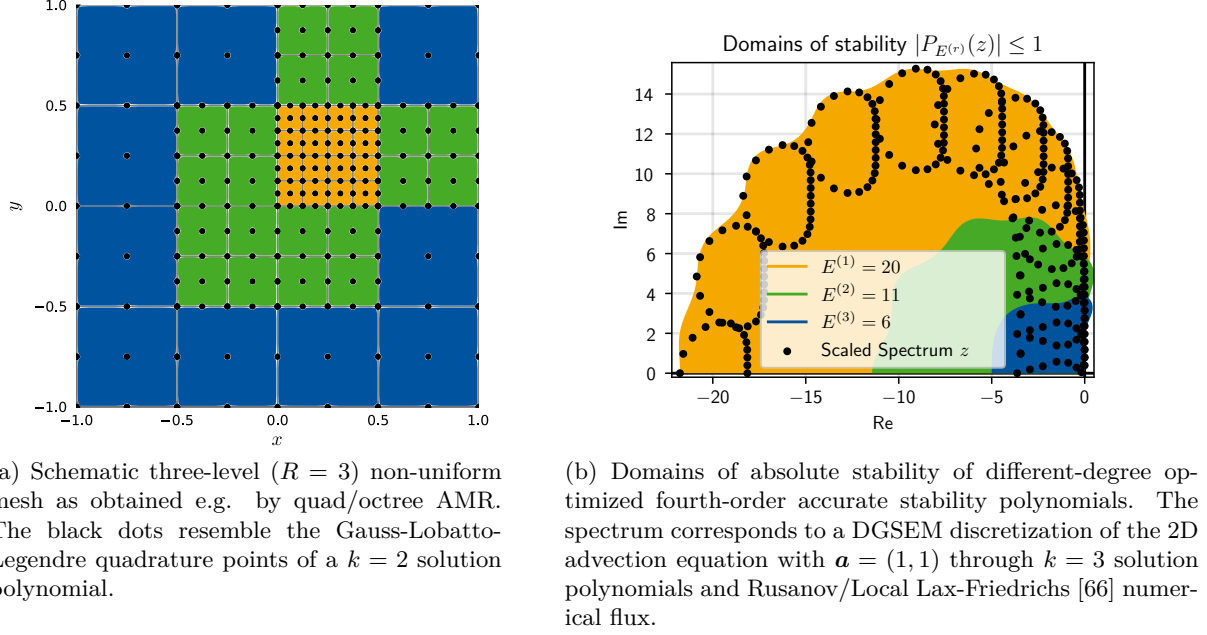


Figure 1: Illustration of the concept of multirate time integration with P-ERK methods. In Fig. 1a a non-uniform mesh as obtained e.g. by classic quad/octree AMR is shown. In Fig. 1b the domains of absolute stability of optimized stability polynomials are presented. These methods could be combined into a  $R = 3$  P-ERK scheme to integrate a PDE on meshes like the one shown in Fig. 1a efficiently.

To foster the understanding of P-ERK schemes, we present the Butcher tableaux of a second-order,  $S = 6$  stage,  $E = \{E^{(1)}, E^{(2)}\} = \{6, 3\}$  stage evaluation P-ERK method:

$i$	$\mathbf{c}$	$A^{(1)}$						$A^{(2)}$					
1	0												
2	$1/10$	$1/10$						$1/10$					
3	$2/10$	$2/10 - a_{3,2}^{(1)}$	$a_{3,2}^{(1)}$					$2/10$	0				
4	$3/10$	$3/10 - a_{4,3}^{(1)}$	0	$a_{4,3}^{(1)}$				$3/10$	0	0			
5	$4/10$	$4/10 - a_{5,4}^{(1)}$	0	0	$a_{5,4}^{(1)}$			$4/10$	0	0	0		
6	$5/10$	$5/10 - a_{6,4}^{(1)}$	0	0	0	$a_{6,4}^{(1)}$		$5/10 - a_{6,5}^{(2)}$	0	0	0	$a_{6,5}^{(2)}$	
	$\mathbf{b}^T$	0	0	0	0	0	1	0	0	0	0	0	1

(2.10)

The first method  $r = 1$  with Butcher matrix  $A^{(1)}$  requires computation of all six stages  $\mathbf{K}_i^{(1)}$ ,  $i = 1, \dots, 6$  while the second method  $r = 2$  with  $A^{(2)}$ , however, requires only the computation of stages  $\mathbf{K}_1^{(2)}, \mathbf{K}_5^{(2)}, \mathbf{K}_6^{(2)}$ , i.e., three evaluations  $E^{(2)} = 3$  of  $\mathbf{F}^{(2)}$ . When looking at the second method in isolation, it resembles a reducible [65, Chapter IV.12] method, i.e., the stages  $\mathbf{K}_2^{(2)}, \mathbf{K}_3^{(2)}, \mathbf{K}_4^{(2)}$  do not influence the final solution  $\mathbf{U}_{n+1}^{(2)}$  and the Butcher tableau could be truncated to a three-stage method. In the context of PRKMs, however, the second to fourth stage guarantee an internally consistent [67] update of the intermediate state  $\mathbf{U}_{n,i}$ , cf. (2.7b). This is assured for identical abscissae  $\mathbf{c}^{(r)} = \mathbf{c} \forall r = 1, \dots, R$  fulfilling the usual convention

$$\sum_{j=1}^{i-1} a_{i,j}^{(r)} \stackrel{!}{=} c_i \quad \forall i = 1, \dots, S; \quad \forall r = 1, \dots, R. \quad (2.11)$$

The intermediate, cheap update of the inactive partitions is essential for the overall accuracy of the method [67].

The particular form of the Butcher tableaux (2.10) comes with three benefits:

1. The P-ERK methods are low-storage, requiring only storage of two Runge-Kutta stages  $\mathbf{K}_i$  at the same time.
2. The computational costs per stage are not increasing if higher stage (evaluation) methods are used, as always at most two stages are used for computation of the intermediate state  $\mathbf{U}_{n,i}$ .
3. The sparse structure of both  $A^{(r)}$  and  $\mathbf{b}^{(r)}$  allows for a simplified computation of the coefficients  $a_{i,j}^{(r)}$  from an optimized stability polynomial  $P^{(r)}(z)$

In previous works [47, 68] we discussed how results derived for partitioned Runge-Kutta methods (PRKMs) extend to P-ERK methods. In particular, we show that criteria for linear stability, order of accuracy, internal consistency, and conservation of linear invariants are met by the P-ERK methods proposed in [45–47]. The archetypes of these third- and fourth-order P-ERK methods are given by (A.2) and (A.4), respectively. Thus, we omit this discussion here except that we remark that for a conservative PRKM (2.7) the weight vector  $\mathbf{b}^T$  must be identical across partitions [67] [32, Chapter IV.1], i.e.,

$$b_i^{(r_1)} = b_i^{(r_2)} = b_i, \quad \forall i = 1, \dots, S; \quad \forall r_1, r_2 = 1, \dots, R. \quad (2.12)$$

Thus, in the following we only consider an identical weight vector  $\mathbf{b}^T$ .

### 2.3. The Notion of Entropy

In the context of this work, we are interested in ODE systems (2.2) with states  $\mathbf{U} \in \mathbb{R}^M$  with standard Euclidian inner product  $\langle \cdot, \cdot \rangle$  and norm. Additionally, we assume a smooth convex global entropy functional

$$H : \mathbb{R}^M \rightarrow \mathbb{R} \quad (2.13)$$

whose temporal evolution is tied to a physical meaningful solution of (2.2) and thus also (2.1). By the chain rule, the evolution over time of  $H(\mathbf{U})$  is given by

$$\frac{d}{dt} H(\mathbf{U}(t)) = \left\langle \frac{\partial H(\mathbf{U})}{\partial \mathbf{U}}, \frac{d}{dt} \mathbf{U}(t) \right\rangle \stackrel{(2.4b)}{=} \left\langle \frac{\partial H(\mathbf{U})}{\partial \mathbf{U}}, \mathbf{F}(t, \mathbf{U}(t)) \right\rangle. \quad (2.14)$$

Entropy-conservative systems (e.g. appropriately discretized Euler equations) thus satisfy

$$\forall \mathbf{U} \in \mathbb{R}^M, t \in [0, T] : \quad \left\langle \frac{\partial H(\mathbf{U})}{\partial \mathbf{U}}, \mathbf{F}(t, \mathbf{U}) \right\rangle = 0 \quad (2.15)$$

with discrete equivalent

$$H(\mathbf{U}_{n+1}) = H(\mathbf{U}_n) = H(\mathbf{U}_0) \quad \forall n \in \mathbb{N}. \quad (2.16)$$

For entropy-dissipative systems (e.g. correspondingly discretized Navier-Stokes-Fourier equations) these equalities are replaced by inequalities, usually by the convention that the (mathematical) entropy decreases over time, i.e.,

$$\left\langle \frac{\partial H(\mathbf{U})}{\partial \mathbf{U}}, \mathbf{F}(t, \mathbf{U}) \right\rangle \leq 0 \quad \Rightarrow \quad H(\mathbf{U}_{n+1}) \leq H(\mathbf{U}_n) \leq H(\mathbf{U}_0) \quad \forall n \in \mathbb{N}. \quad (2.17)$$

In this work we are concerned with the compressible flows of ideal gases described by the Euler, Navier-Stokes-Fourier, or magnetohydrodynamics (MHD) equations. For these systems, the mathematical entropy  $s$  as a function of the continuous conserved variables  $\mathbf{u}$  is given by

$$s(\mathbf{u}) := - \underbrace{\rho}_{\equiv u_1} \cdot s_{\text{therm}}(\mathbf{u}) = -\rho \cdot \log \left( \frac{p(\mathbf{u})}{\rho^\gamma} \right), \quad (2.18)$$

which is then integrated over the spatial domain  $\Omega$  to obtain the total entropy  $\eta$ :

$$\eta(t) := \eta(\mathbf{u}(t, \mathbf{x})) = \int_{\Omega} s(\mathbf{u}(t, \mathbf{x})) \, d\mathbf{x}. \quad (2.19)$$

Note that we denote with  $\eta : \mathbb{R} \rightarrow \mathbb{R}$  the continuous equivalent of the discrete global entropy  $H : \mathbb{R}^M \rightarrow \mathbb{R}$ .

#### 2.4. Relaxation Runge-Kutta Methods

The term Relaxation Runge-Kutta method (RRKM) was coined in [37] for Runge-Kutta methods whose final update step (2.7c) is scaled by the *relaxation parameter*  $\gamma_n \in \mathbb{R}$ :

$$\mathbf{U}_{n+1}(\gamma_n) = \mathbf{U}_n + \Delta t \gamma_n \sum_{i=1}^S b_i \mathbf{K}_i. \quad (2.20)$$

Recall that  $\mathbf{K}_i$  denotes the  $i$ -th stage of the Runge-Kutta method, i.e.,

$$\mathbf{K}_i = \mathbf{F}(t_{n,i}, \mathbf{U}_{n,i}), \quad i = 1, \dots, S \quad (2.21)$$

with intermediate state  $\mathbf{U}_{n,i} = \mathbf{U}_n + \Delta t \sum_{j=1}^S a_{i,j} \mathbf{K}_j$  and time  $t_{n,i} = t_n + c_i \Delta t$ , cf. (2.7b).

The introduction of this relaxation parameter allows to satisfy exact entropy conservation, i.e.,

$$H(\mathbf{U}_{n+1}(\gamma_n)) \stackrel{!}{=} H(\mathbf{U}_n) + \gamma_n \Delta t \sum_{i=1}^S b_i \left\langle \frac{\partial H(\mathbf{U}_{n,i})}{\partial \mathbf{U}_{n,i}}, \mathbf{K}_i \right\rangle. \quad (2.22)$$

It is worthwhile to examine (2.22) for a trivial function  $\mathbf{H}$ , for instance  $\mathbf{H}(\mathbf{U}) = \mathbf{I}\mathbf{U}$  where  $\mathbf{I}$  is the identity matrix  $\mathbf{I} \in \mathbb{R}^{M \times M}$ . Thus, for a single component  $k$  of  $\mathbf{U}$  we have  $H_k(\mathbf{U}) = U^{(k)} = \sum_{m=1}^M \delta_{km} U^{(m)}$  with Kronecker delta  $\delta_{km}$ . In this case (2.22) corresponds to the well-known linear-invariant (i.e., mass) conservation property of Runge-Kutta methods, as for every component  $k$  of  $\mathbf{U}$  we have

$$H_k(\mathbf{U}_{n+1}(\gamma_n)) = U_{n+1}^{(k)}(\gamma_n) = U_n^{(k)} + \gamma_n \Delta t \sum_{i=1}^S b_i \langle \mathbf{e}_k, \mathbf{K}_i \rangle \quad (2.23)$$

$$\stackrel{(2.20)}{\Leftrightarrow} \sum_{m=1}^M \delta_{km} \left[ \mathbf{U}_n + \Delta t \gamma_n \sum_{i=1}^S b_i \mathbf{K}_i \right] = U_n^{(k)} + \gamma_n \Delta t \sum_{i=1}^S b_i K_i^{(k)} \quad (2.24)$$

where  $\mathbf{e}_k \in \mathbb{R}^M$  is the  $k$ -th (Euclidian) unit vector. Additionally, we immediately see that arbitrary linear invariants are conserved for every choice of  $\gamma_n$ . The same holds of course also for linear functions resulting in a scalar entropy, such as  $H(\mathbf{U}) = \mathbf{q}^T \mathbf{U}$  where  $\mathbf{q} \in \mathbb{R}^M$  could resemble a vector corresponding to quadrature weights.

For nonlinear functions  $H(\mathbf{U})$  such as the (mathematical) entropy (2.22) does not trivially hold, however. In this scenario, we search for a relaxation parameter  $\gamma_n$  such that the true change in entropy

$$\Delta H_n := \Delta t \sum_{i=1}^S b_i \left\langle \frac{\partial H(\mathbf{U}_{n,i})}{\partial \mathbf{U}_{n,i}}, \mathbf{K}_i \right\rangle \quad (2.25)$$

matches the entropy of the relaxed update state  $\mathbf{U}_{n+1}(\gamma_n)$ :

$$H(\mathbf{U}_{n+1}(\gamma_n)) = H \left( \mathbf{U}_n + \Delta t \gamma_n \sum_{i=1}^S b_i \mathbf{K}_i \right) \stackrel{!}{=} H(\mathbf{U}_n) + \gamma_n \Delta H_n(\mathbf{U}_n). \quad (2.26)$$

For entropy-conservative systems the the scalar product in (2.25) is thus exactly zero, i.e.,

$$\left\langle \frac{\partial H(\mathbf{U}_{n,i})}{\partial \mathbf{U}_{n,i}}, \mathbf{K}_i \right\rangle \stackrel{(2.21)}{=} \left\langle \frac{\partial H(\mathbf{U}_{n,i})}{\partial \mathbf{U}_{n,i}}, \mathbf{F}(t_{n,i}, \mathbf{U}_{n,i}) \right\rangle = 0 \quad (2.27)$$

Note that we demand the equality (2.26) also for entropy diffusive systems, i.e., systems with  $\langle \partial \mathbf{U} H, \mathbf{F} \rangle \leq 0$  to suppress erroneous additional changes in entropy due to the time integration method.

We can rewrite (2.25) by introducing the *entropy variables* [27]

$$\mathbf{w}(\mathbf{u}) := \frac{\partial s(\mathbf{u})}{\partial \mathbf{u}} \in \mathbb{R}^V \quad (2.28)$$

with (2.19) as

$$\Delta H_n = \Delta t \sum_{i=1}^S b_i \left\langle \int_{\Omega} \mathbf{W}_{n,i} \, d\Omega, \mathbf{K}_i \right\rangle \quad (2.29)$$

which will be used in the remainder. The vector of discretized entropy variables  $\mathbf{W}$  is obtained by evaluating the entropy variables at every node of the mesh and then re-assembling them into a vector of dimension  $\mathbb{R}^M$ . Note that integration of discrete integrands is denoted by the differential form  $d\Omega$ , while for integration of continuous quantities we employ  $d\mathbf{x}$ , cf. (2.19).

It is well-known that the first order condition for a Runge-Kutta method is that  $\sum_{i=1}^S b_i = 1$ . Thus, we interpret  $\gamma_n$  as acting on the timestep  $\Delta t$  rather than on the weights  $\mathbf{b}^T$ . Consequently, the obtained update  $\mathbf{U}_{n+1}(\gamma_n)$  is understood as an approximation at time  $t_{n+1} = t_n + \gamma_n \Delta t$  [37, 38].

Conversely, when interpreting the relaxed result  $\mathbf{U}_{n+1}(\gamma_n)$  as an approximation to  $t_{n+1} = t_n + \Delta t$  the RRKM can be viewed as a projection method [32, Chapter IV.4] [37]. In that case, the relaxation mechanism can be interpreted as an instance of the incremental direction technique (IDT) [36–38].

At this point, numerous questions arise, concerning for instance existence and uniqueness of  $\gamma_n$ , order of the method, and stability properties. Here, we briefly state the main results obtained in [37, 38, 41] which settle these concerns.

- **Existence and uniqueness of  $\gamma_n$ :** Clearly (2.26) is trivially fulfilled for  $\gamma_n = 0$ . A positive (i.e., nontrivial) unique solution which is close to unity exists for  $\gamma_n$  for strictly convex entropy functionals  $H$  coupled with at least second-order accurate schemes for sufficiently small  $\Delta t$ .
- **Accuracy:** Given a Runge-Kutta method of order  $p$ , the relaxed update  $\mathbf{U}_{n+1}(\gamma_n)$  is an order  $p$  approximation of the true solution at time  $t_{n+1} = t_n + \gamma_n \Delta t$  for relaxation parameters  $\gamma_n = 1 + \mathcal{O}(\Delta t^{p-1})$  (which follows from the existence and uniqueness of  $\gamma_n$ ). We validate this property in Section 4.3.
- **Linear Stability:** For  $\gamma_n \leq 1$  the relaxed method is linearly stable for a given timestep  $\Delta t$  if the standard method is linearly stable for this  $\Delta t$ . We provide a brief illustration on this manner by means of a concrete example in Section 3.2.
- **Nonlinear Stability:** We remark that also e.g. strong stability preserving (SSP) methods [69, 70] can be relaxed while maintaining their nonlinear stability properties.

We are now equipped with the necessary tools to introduce the P-ERK methods with relaxation.

### 3. Paired Explicit Relaxation Runge-Kutta Methods

The generalization of the relaxation methodology to P-ERK schemes is straightforward. Due to the shared weight vector cf. (2.12) all stages  $i$  with  $b_i \neq 0$  are evaluated across all partitions  $r = 1, \dots, R$ . Thus, the *direction*

$$\mathbf{d}_n := \sum_{i=1}^S b_i \mathbf{K}_i \quad (3.1)$$

and entropy change  $\Delta H$  (cf. (2.26)) are computed completely analogous to standard Runge-Kutta methods. As we are only concerned with P-ERK methods of order two and higher, the conditions for existence and uniqueness of a solution  $\gamma_n$  are fulfilled. Furthermore, the P-ERK

schemes considered in [45–47, 68] have nonnegative weights  $b_i \geq 0$  which ensures that the relaxed update is dissipation preserving for such problems [38] and avoids stage downwinding [71].

The sparsity in the weight vector  $\mathbf{b}^T$  renders P-ERK methods especially attractive for the relaxation methodology. The vanilla second-order method as proposed in [45] has only  $b_S = 1$  with all other entries being zero. The third-order method proposed in [46] has non-zero  $b_{S-1} = 0.75, b_S = 0.25$ . The third-order variant proposed in [68] adds  $b_1 = 1/6$  to  $b_{S-1} = 1/6, b_S = 2/3$  which avoids a negative entry in Butcher array of the original scheme [46], thus there is no downwinding of stages [71]. Finally, the fourth-order method developed in [47] has  $b_{S-1} = b_S = 0.5$ . Archetypes for the Butcher tableaux of these methods are provided in Appendix A.

This sparsity in  $\mathbf{b}^T$  is a very attractive feature as this reduces the number of integrations involved in a sequential computation of  $\Delta H$ , cf. (2.25). Of course, with the usual computation-storage tradeoff one can always reduce (2.25) to a single integration if all intermediate approximations  $\mathbf{U}_{n,i}$  and stages  $\mathbf{K}_i$  are stored, even though they are not required for the actual update (2.7c). We remark that the transform from conserved  $\mathbf{U}_{n,i}$  to entropy variables  $\mathbf{W}_{n,i}$  would also be required for this approach. In our implementation of the P-ERRK methods we opt for the sequential computation of (2.25) to avoid unnecessary memory overhead.

In practice, we compute (2.29) as

$$\Delta H_n = \Delta t \sum_{i=1}^S b_i \sum_j \int_{\Omega_j} \sum_l \langle \mathbf{w}_{n,i,j,l}, \mathbf{k}_{i,j,l} \rangle d\Omega_j \quad (3.2)$$

which follows from interchanging the scalar product and the integral (a quadrature rule on the discrete level). Thus, for every element  $\Omega_j$  in the mesh we compute the dot product  $\langle \mathbf{w}_{n,i,j,l}, \mathbf{k}_{i,j,l} \rangle$  for each node  $l$  in the element. Note that on every node we have exactly  $V$  variables, thus the inner product in (3.2) is a scalar product on  $\mathbb{R}^V$ .

### 3.1. Solving the Relaxation Equation

To ensure an entropy-stable time update the scalar nonlinear equation

$$r(\gamma_n) := H(\mathbf{U}_n + \gamma_n \Delta t \mathbf{d}_n) - H(\mathbf{U}_n) - \gamma_n \Delta H_n \stackrel{!}{=} 0 \quad (3.3)$$

needs to be solved for  $\gamma_n$ . In the preparation of this work we considered three main approaches to solve (3.3). These are a standard bisection procedure which is quite robust and easy to implement. The drawback of this method is, however, that one needs to supply a bracketing interval  $[\gamma_{\min}, \gamma_{\max}]$ . As the bisection method converges only linearly, the choice of this bracketing interval heavily influences the number of iterations taken to solve (3.3) to some desired accuracy. Second, we considered the secant method which can be seen as a middle-ground between the bisection method and Newton-Raphson method. In particular, the secant method is of similar computational complexity as the bisection method, but offers a higher convergence rate. As for bisection, however, the secant method also requires two initial guesses  $\gamma_0, \gamma_1$  which are used to compute the first update. The presence and significance of these hyperparameters render the secant method only a fallback option for our purposes.

Thus, we mainly considered variants of the Newton-Raphson method which converge quadratically near the root. The required derivative of  $\frac{dr}{d\gamma_n}$  is given by [38]

$$r'(\gamma_n) = \int_{\Omega} \langle \mathbf{w}(\mathbf{U}_n + \gamma_n \Delta t \mathbf{d}_n), \Delta t \mathbf{d}_n \rangle d\Omega - \Delta H_n. \quad (3.4)$$

To determine the stepsize in the Newton-Raphson procedure we experimented with different line-search methods. In practice (see Section 4.1) we found that the vanilla Newton-Raphson procedure with trivial stepsize 1 converges extremely fast (1 to 3 iterations) and additional line-search methods are not necessary. In the very first timestep we set  $\gamma_1 = 1$  while in subsequent timesteps we use the previously obtained value for the relaxation parameter as the initial guess

for the Newton-Raphson iteration. As stopping criteria we employ the residual of the relaxation equation (3.3), the magnitude of the update step and a maximum number of iterations to prevent iterating divergent sequences.

### 3.2. Entropy Relaxation as Time Limiting

The traditional discretization of a hyperbolic PDE involves a spatial discretization that is total variation diminishing (TVD)/total variation bounded (TVB) or offers at least some form of control over oscillations at discontinuities. This is then paired with an SSP time integration scheme to prevent the introduction of spurious oscillations due to the time marching mechanism [70, 71]. The latter scheme may be explicit or implicit, however, even for unconditionally linearly stable (A-stable) implicit methods of order  $p > 1$ , the nonlinearly stable, i.e., stability-preserving timestep is finite [70]. In order to render implicit schemes more efficient than their explicit counterparts timesteps beyond the SSP stability limit are often employed. Since in this case global non-oscillarity can no longer be guaranteed, localized *time-limiting* strategies have been studied [72–74] with some recent contributions [75–77]. The central idea in the referenced works is to blend a high-order implicit scheme with the first-order, unconditionally nonlinearly stable implicit/backward Euler method.

In order to determine the limiting factor/blending coefficient different criteria based e.g. on temporal derivatives [73, 76] have been employed. Recently, an indicator based on the local numerical entropy production

$$\Delta s_{n,j} := \frac{1}{\Delta t} \left[ s(\mathbf{U}_{n+1,j}) - s(\mathbf{U}_{n,j}) - \frac{\Delta t}{\Delta x} \sum_{i=1}^S b_i \left( \Psi_{i,j-\frac{1}{2}} - \Psi_{i,j+\frac{1}{2}} \right) \right] \quad (3.5)$$

was proposed in [77]. Derived in the context of one-dimensional finite-volume schemes, (3.5) denotes the entropy production on cell  $j$  due to numerical entropy fluxes  $\Psi_{i,j\pm\frac{1}{2}}$  exchanged from time  $t_n$  to  $t_{n+1}$ . The numerical entropy fluxes are required to be consistent with the entropy flux  $\psi(\mathbf{u})$  [27] which corresponds to the entropy  $s(\mathbf{u})$  in the sense that  $\left(\frac{\partial \psi}{\partial \mathbf{u}}\right)^T = \mathbf{w}^T \frac{\partial \mathbf{f}}{\partial \mathbf{u}}$  [27]. Equation (3.5) can be understood as a localized version of the relaxation equation (2.22) as both determine the change in entropy due to the numerical scheme. In fact, by integrating (3.5) over all cells and time interval  $[t_n, t_{n+1}]$  we recover (2.22) for a suitable choice of the numerical entropy flux function  $\Psi$ .

We would like to remark that the relaxation methodology can also be applied to local entropies, i.e., convex functionals that are defined on subdomains  $\Omega_j \subset \Omega$  [40]. In the extreme, these subdomains could be reduced to single cells, resulting in local entropy changes  $\Delta H_j$  which can be computed analogous to (3.5).

In [77], the authors employ (3.5) as an indicator if the timestep needs to be reduced to avoid oscillations. Similarly, the relaxation mechanism as discussed above can act as a limiter for monotonicity violations due to discontinuities in the partitioned Runge-Kutta scheme. This is particularly attractive as we have demonstrated in [68] that at the intersection of partitions spurious oscillations may occur. These are intensified for larger differences in active stage evaluations  $E^{(1)} - E^{(2)}$ , larger timesteps, and reduced grid resolution [68]. In the next section we follow up on this insights and demonstrate in what sense the relaxation methodology can act as a time-limiting mechanism for P-ERK methods.

#### 3.2.1. 1D Advection Equation

We consider the standard advection equation

$$u_t + u_x = 0 \quad (3.6)$$

on a non-uniform grid with periodic boundaries. As a first motivation we present the advection of a Gaussian pulse  $u_0(x) = \exp(-x^2)$  on  $\Omega = [-4, 4]$ . The base mesh size is  $\Delta x^{(2)} = 0.5$  while

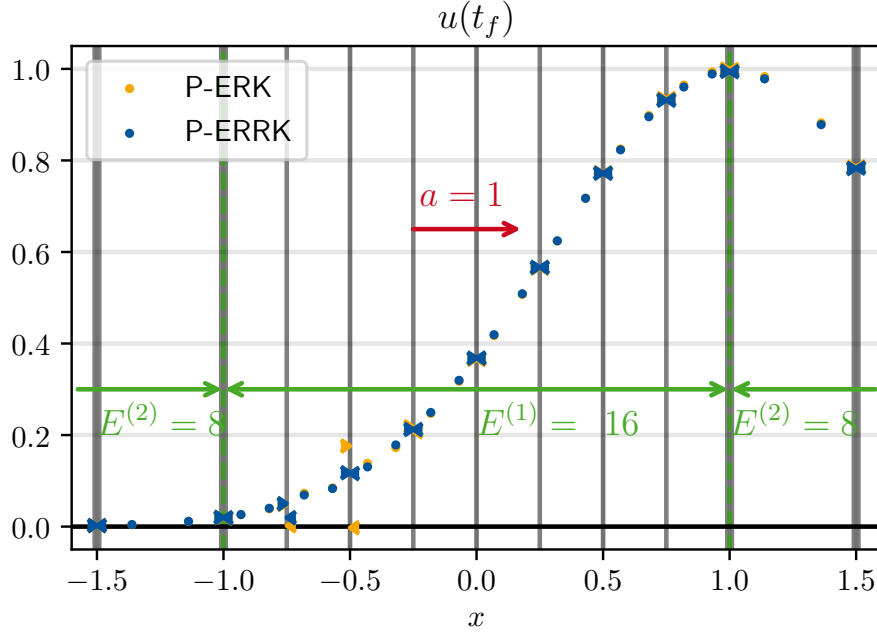
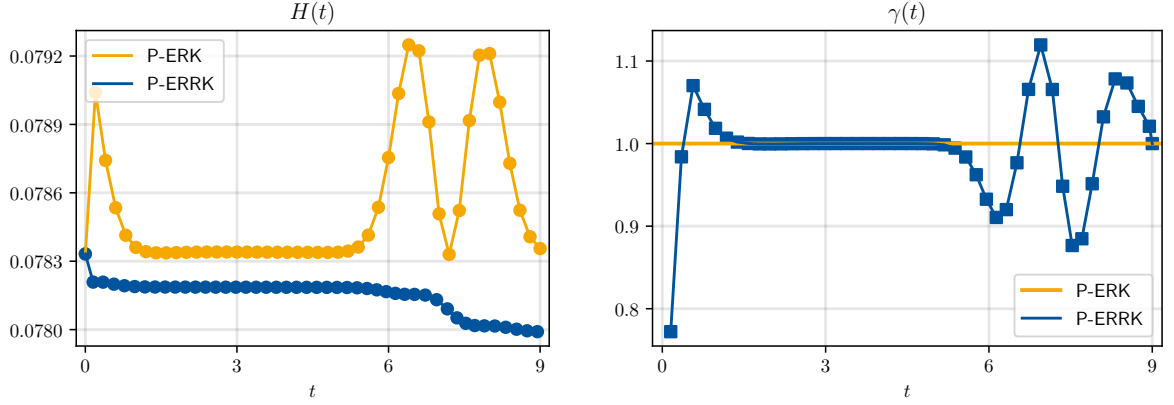


Figure 2: Relaxation as time-limiting: Advection equation (3.6) on two-level, non-uniform mesh solved with standard (orange) and relaxed (blue) P-ERK methods. The interpolated solution is displayed at the Gauss-Lobatto-Legendre nodes values at  $t_f = 9$  on the interval  $[-1.6, 1.6]$ . Cell boundaries are indicated by the vertical lines and contain  $k + 1 = 4$  nodes. To distinguish the nodes at cell boundaries, left boundary nodes are indicated by left-pointing triangles, while right boundary nodes are indicated by right-pointing triangles. Interior nodes are indicated by circles.

cells in  $[-1, 1]$  are refined once, i.e., have length  $\Delta x^{(1)} = 0.25$ . We optimize  $E = \{8, 16\}$  second-order accurate methods for a  $k = 3$  DGSEM discretization with Upwind/Godunov surface flux. We run the simulation with  $\Delta t = 0.2$  until  $t_f = 9$ , i.e., the Gaussian pulse has traversed the domain once and is now centered at  $x = 1$ , with left tail in the refined region. For the standard P-ERK method we observe severe oscillations in the second and third refined cell, Fig. 2. In fact, these oscillations are strong enough to violate the positivity of the solution. Next, we consider the P-ERRK method. For the standard scalar advection equation (3.6) a suitable mathematical entropy is given by  $s(u) = u^2$  which coincides with the energy of the solution. We solve the relaxation equation (3.3) using the Newton-Raphson method which is limited to 10 iterations and also stops if the function residual is less or equal  $10^{-14}$  or the update step is less than  $10^{-15}$ . If the Newton iteration does not converge to a root, a non-relaxed step is taken corresponding to  $\gamma = 1$ . This is, however, not observed for this simulation. Furthermore, on average only three Newton iterations per simulation step are performed.

It is evident from Fig. 2 that the relaxation approach greatly reduces oscillations in the second cell in direction of the advection velocity at the coarse-fine intersection. In order to better visualize Gauss-Lobatto-Legendre nodes at the cell interfaces, we employ right-pointing triangles for the right boundary nodes and left-pointing triangles for the left boundary nodes, while interior nodes are indicated by circles. By closely examining Fig. 2 we observe that the entropy-stable relaxed scheme manages to preserve positivity of the solution, while the standard P-ERK method shows negative nodal values. This comes at the expense, however, that we observe slight global diffusion of the solution, which is visible at the tip of the Gaussian pulse.

By examining the temporal evolution of the global entropy  $H(t)$  Fig. 3a for the two methods it is evident that the relaxation methodology adds diffusion only when required, i.e., when the entropy for the standard P-ERK scheme increases. In particular, these are the first timestep and the traversal of the refined region by the Gaussian pulse happening roughly in the  $t \in [5, 9]$  time interval. This is also reflected in the evolution of the relaxation parameter  $\gamma_n$  Fig. 3b which deviates from 1 only when the entropy of the standard P-ERK method changes. Noticeably,  $\gamma$



(a) Entropy evolution for standard (orange) and relaxed (b) Relaxation parameter  $\gamma$  over the course of the simulation. (blue) two-level multirate methods.

Figure 3: Relaxation as time-limiting: Advection equation (3.6) on two-level, non-uniform mesh. The temporal evolution of the entropy  $H(t)$  is depicted in Fig. 3a for the standard (orange) and relaxed (blue) P-ERK method. The relaxation parameter  $\gamma(t)$  is shown in Fig. 3b for the relaxed method.

is negatively correlated with the change in entropy  $H$ , i.e., for increasing entropy  $\gamma_n$  is reduced and vice versa, which is related to the convexity of the entropy functional. To some extent, the relaxation methodology acts in this case also as a timestep adapting mechanism which is based on a nonlinear solution functional instead of the deviation between a higher- and a lower-order embedded method. The relaxation methodology thus ensures that the entropy dissipative nature of the spatial discretization is preserved. In particular, we cannot expect an entropy conservation scheme here as we employ the diffusive Upwind/Godunov flux and not e.g. the central flux.

To shed further light on the stabilizing effect due to relaxation we consider the fully discrete system

$$\mathbf{U}_{n+1} = \begin{pmatrix} \mathbf{U}_{n+1}^{(1)} \\ \mathbf{U}_{n+1}^{(2)} \end{pmatrix} = \begin{pmatrix} D^{(1)}(\gamma_{n+1}) \\ D^{(2)}(\gamma_{n+1}) \end{pmatrix} \mathbf{U}_n = D(\gamma_{n+1}) \mathbf{U}_n \quad (3.7)$$

which is obtained by applying the  $p = 2, E = \{8, 16\}$  two-level P-ERK method (2.7) to

$$\mathbf{U}'(t) = \begin{pmatrix} \mathbf{U}^{(1)}(t) \\ \mathbf{U}^{(2)}(t) \end{pmatrix}' = \begin{pmatrix} L^{(1)} \\ L^{(2)} \end{pmatrix} \mathbf{U}(t) = L \mathbf{U}(t) \quad (3.8)$$

which is the linear equivalent of (2.4b). The update matrix  $D(\gamma)$  can now be used to confirm linear stability by assessing whether all eigenvalues of  $D(\gamma)$  are inside the unit circle. This is indeed the case for both the standard P-ERK method, i.e.,  $\gamma = 1$  and the relaxed method with  $\gamma \neq 1$ , which confirms the discussion on linear stability from Section 2.4. Note that for the standard P-ERK method  $D(\gamma) \equiv D(1)$  for all times, i.e., the update matrix remains constant. For the P-ERRK methods, however,  $D(\gamma_n)$  is in general not identical among timesteps due to the relaxation parameter  $\gamma_n$ . We provide plots of the spectra of the constant  $D(1)$  and  $D(\gamma_1)$  matrices in the appendix, see Fig. B.18. Furthermore, one may employ  $D$  to examine the nonlinear stability of the time integration methods. It is well-known that the fully-discrete method is monotonicity-preserving in the sense of Harten [78] if and only if

$$D_{ij} \geq 0 \quad \forall i, j = 1, \dots, N. \quad (3.9)$$

Since the underlying spatial discretization is a fourth-order DGSEM scheme we cannot expect (3.9) to hold. Nevertheless, it is interesting to examine the minimum and maximum entries of  $D(1)$  and  $D(\gamma_1)$  to see if the relaxation mechanism has a stabilizing effect. For the standard



P-ERK method we have  $\min_{i,j} D_{i,j}(1) \approx -0.370$  and  $\max_{i,j} D_{i,j}(1) \approx 1.115$ . For the relaxed method we have for  $\gamma_1 \approx 0.772$  that  $\min_{i,j} D_{i,j}(\gamma_1) \approx -0.286$  and  $\max_{i,j} D_{i,j}(\gamma_1) \approx 0.86$ . Clearly, the relaxation mechanism nudges the entries of  $D$  closer to the  $[0, 1]$  interval. Additionally, we would like to remark that for both cases the row-sums equal one, i.e.,  $\sum_j D_{ij} = \mathbf{1}$ , thereby reflecting the conservation property of the P-ERK/P-ERRK methods. This is discussed in more detail in Section 4.2.

### 3.2.2. Kelvin-Helmholtz Instability with Adaptive Mesh Refinement

Motivated by these insights we reconsider a numerical example conducted in [68], wherein we studied the applicability of the standard P-ERK schemes to the Kelvin-Helmholtz instability on an adaptively refined mesh. We employ the setup from [79] with initial condition at  $t_0 = 0$  given by

$$\begin{pmatrix} \rho \\ v_x \\ v_y \\ p \end{pmatrix} = \begin{pmatrix} \frac{1}{2} + \frac{3}{4}b \\ \frac{1}{2}(b-1) \\ \frac{1}{10} \sin(2\pi x) \\ 1 \end{pmatrix}, \quad b := \tanh(15y + 7.5) - \tanh(15y - 7.5)$$

on periodic domain  $\Omega = [-1, 1]^2$  which we simulate up to  $t_f = 3.2$ . The compressible Euler equations are discretized using the DGSEM with  $k = 3$  local polynomials, Harten-Lax-Van Leer-Einfeldt (HLLC) surface-flux [80], subcell shock-capturing [81] to avoid spurious oscillations, and entropy-conserving volume flux [26]. Initially, the domain is discretized with  $2^4 \times 2^4$  cells which are allowed to be refined five times, i.e., the finest cells may have edge length  $h = 2^{-8}$ . The indicator for AMR coincides in this case with the shock-capturing indicator [81] and is based on the density  $\rho$ . In [68] the  $p = 3, E = \{4, 6, 11\}$  scheme was constructed which we employ here as well. The only parameter changed compared to [68] is the AMR interval which is decreased to  $N_{\text{AMR}} = 7$ , i.e., the mesh is allowed to change every 7<sup>th</sup> timestep. The relaxation equation is solved with the Newton-Raphson method with a maximum of 5 iterations, root-residual tolerance of  $10^{-15}$  and stepsize tolerance of  $10^{-13}$ .

We observe significantly improved robustness of the relaxed P-ERRK scheme compared to the standard P-ERK scheme. The relaxed scheme advances the simulation stable up to the final time  $t_f = 3.2$  (see Fig. B.19 for a plot of the density and mesh at final time) while the standard scheme crashes at  $t \approx 2.74$  due to violated positivity of density and pressure. We emphasize that application of the relaxation methodology does not exclusively reduce the timestep, i.e., the relaxation parameter  $\gamma_n$  is not always less than 1. In particular, for the simulation up to  $t_f = 2.73$  we observe in fact reduced number of timesteps for the relaxed scheme (1184) compared to the standard P-ERK scheme (1267). Although very encouraging, this should be taken with a grain of salt due to the highly volatile nature of the Kelvin-Helmholtz instability, especially when paired with AMR.

## 4. Validation

### 4.1. Entropy Conservation

To check for the exact entropy conservation property provided by the P-ERRK methods we consider the compressible Euler equations in conjunction with an entropy-conservative spatial discretization. Here, we always employ the DGSEM [18–20] with entropy-conservative and kinetic energy preserving numerical flux by Ranocha [26] to solve the Riemann problems at cell interfaces. Additionally, the volume integral is computed based on SBP operators and flux-differencing [7, 15, 16, 21, 22] which is required to stabilize the entropy-conservative, i.e., diffusion-free surface flux. For the “volume flux” we use in the examples below also the flux by Ranocha, although we would like to remark that other choices such as the flux by Chandrashekar [23] are possible [25]. All computations presented in this work are performed with Trixi.jl [82–84], an open-source Julia [85] package for high-order, adaptive simulation of conservation laws

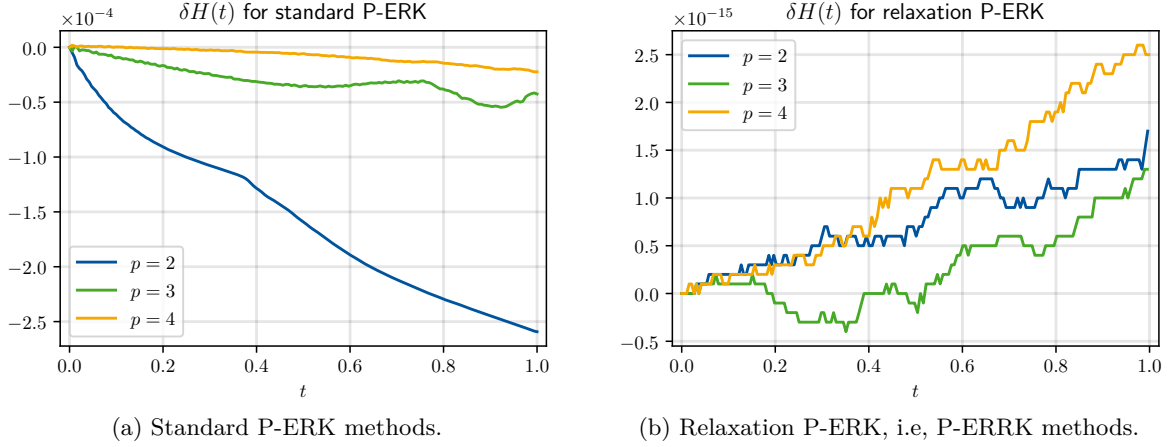


Figure 4: Temporal evolution of the total entropy defect  $\delta H(t)$  (4.2) for the weak blast wave problem (Euler equations) (4.1) for standard P-ERK methods (Fig. 4a) and P-ERRK methods with relaxation (Fig. 4b).

and related systems. We provide a reproducibility repository publicly available on Github [86] for all results discussed in this paper.

#### 4.1.1. Weak Blast Wave: Euler & Ideal MHD Equations

We demonstrate the entropy conservation capabilities of the P-ERRK methods for a discontinuous initial condition. To this end, we consider a 1D variant of the weak blast wave problem as proposed in [81] with discontinuous initial condition

$$\rho_0 = \begin{cases} 1.1691 & |x| \leq 0.5 \\ 1 & |x| > 0.5 \end{cases}, v_0 = \begin{cases} 0.1882 \cdot \text{sgn}(x) & |x| \leq 0.5 \\ 0 & |x| > 0.5 \end{cases}, p_0 = \begin{cases} 1.245 & |x| \leq 0.5 \\ 1 & |x| > 0.5 \end{cases}. \quad (4.1)$$

The isentropic exponent is set to  $\gamma = 1.4$  and we employ  $k = 3$  DG solution polynomials. The domain is  $\Omega = [-2, 2]$  equipped with periodic boundary conditions. We discretize  $\Omega$  with a non-uniform mesh consisting of three-levels which is refined towards the center. Precisely, cells in the  $[-0.5, 0.5]$  interval are of size  $\Delta x^{(1)} = 1/32$ , cells in the  $[-1, -0.5] \cup [0.5, 1]$  interval are of size  $\Delta x^{(2)} = 1/16$ , and cells in the  $[-2, -1] \cup [1, 2]$  interval have size  $\Delta x^{(3)} = 1/8$ . The mesh and initial condition are depicted in Fig. B.20 which is provided in the appendix. We thus construct for every order of consistency  $p = \{2, 3, 4\}$  a P-ERRK scheme for which the maximum admissible timestep  $\Delta t$  doubles for each family member. For the second-order method we use a  $E_2 = \{3, 5, 9\}$  stage-evaluation method, for the third-order method a  $E_3 = \{4, 7, 13\}$  method, and for the fourth-order method a  $E_4 = \{6, 10, 18\}$  method. To solve the equation for the relaxation parameter  $\gamma_n$  we use the standard Newton-Raphson method which is stopped after five steps or if the residual  $r(\gamma_n)$  or steplength  $\Delta \gamma_n$  are less or equal to machine epsilon  $\epsilon \sim 2 \cdot 10^{-16}$ . Here we enforce the first equality in (2.16), i.e., maintained entropy from timestep  $n$  to  $n + 1$ . Across orders of consistency, about two to three Newton iterations are performed on average per timestep.

The evolution of the entropy change

$$\delta H(t) := H(t) - H(t_0) \quad (4.2)$$

is depicted in Fig. 4. For the standard methods we observe entropy dissipation, which is reduced for increasing order of consistency, cf. Fig. 4a. For the P-ERRK methods with relaxation we see that the total entropy is conserved up to orders within the rounding error regime, cf. Fig. 4b.

Additionally, we consider the weak blast wave problem for the ideal MHD equations. Here, we employ a "1.5"-dimensional variant of the MHD equations by enhancing the state vector by

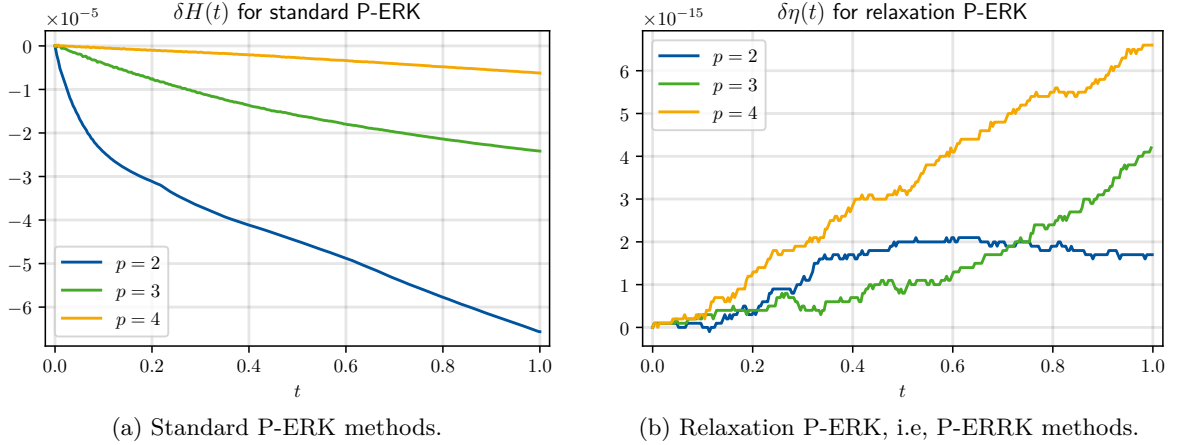


Figure 5: Temporal evolution of the total entropy defect  $\delta H(t)$  (4.2) for the weak blast wave problem (ideal MHD equations) for standard P-ERK methods (Fig. 5a) and P-ERRK methods with relaxation (Fig. 5b).

velocity and magnetic fields in  $y$  and  $z$  direction, while allowing variations only in  $x$  direction. The divergence-free constraint of the magnetic field  $\mathbf{B}$

$$\nabla \cdot \mathbf{B} = 0 \quad (4.3)$$

is automatically satisfied for spatially univariate problems, as the  $x$ -component of the magnetic field stays constant for constant initializations. The hydrodynamic variables are initialized according to (4.1) while all components of the magnetic field  $\mathbf{B}$  are set to unity. The  $y$  and  $z$  components of the velocity  $\mathbf{v}$  are initialized to zero. An entropy-conservative semidiscretization is constructed analogous to the Euler case by means of an extension of the entropy-conservative flux by Ranocha [26] to the MHD equations [87]. The mesh, relaxation equation solver, and time integration schemes are kept identical to the previous example. The mathematical entropy  $H$  of the MHD equations is also the same as in the Euler case. On average, only one to two Newton iterations are performed per timestep for the P-ERRK methods. We depict the evolution of the entropy defect  $\delta H$  for the standard and relaxation P-ERRK methods in Fig. 5.

#### 4.1.2. Isentropic Vortex Advection

As a second testcase for the multirate, entropy conserving P-ERRK methods we consider the classic isentropic vortex advection testcase [69, 88]. Here, we use the parametrization as proposed in [45]. The background flow is set to

$$\rho_\infty = 1, \quad \mathbf{v}_\infty = \begin{pmatrix} 1 \\ 1 \end{pmatrix}, \quad p_\infty := \frac{\rho_\infty^\gamma}{\gamma \text{Ma}_\infty^2} \quad (4.4)$$

with  $\text{Ma}_\infty = 0.4$  and  $\gamma = 1.4$ . To localize the effect of the vortex centered at  $\mathbf{c}(t, \mathbf{x}) := \mathbf{x} - \mathbf{v}_\infty t$  the perturbations are weighted with the Gaussian  $g(t, \mathbf{x}, y) := \exp\left(\frac{1 - \|\mathbf{c}(t, \mathbf{x})\|^2}{2R^2}\right)$  where  $R = 1.5$ . The size of the vortex is governed by  $R$  and the intensity/strength is controlled by  $I = 13.5$ , following [45]. The density is then given by

$$\rho(t, \mathbf{x}) = \rho_\infty \left(1 - \frac{I^2 M^2 (\gamma - 1) g^2(t, \mathbf{x})}{8\pi^2}\right)^{\frac{1}{\gamma-1}} \quad (4.5)$$

and the corresponding perturbed velocities are

$$\mathbf{v}(t, \mathbf{x}) = \mathbf{v}_\infty + \frac{I g(t, \mathbf{x})}{2\pi R} \mathbf{c}(t, \mathbf{x}) \quad (4.6)$$

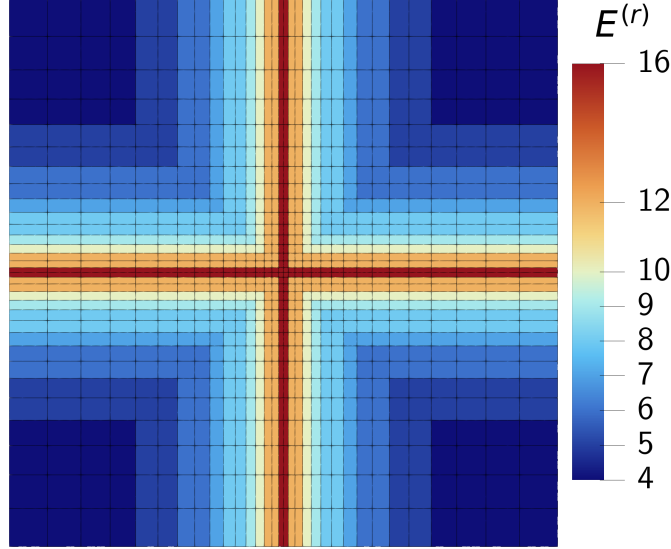


Figure 6: Non-uniform, conforming mesh according to (4.8) for the isentropic vortex testcase to validate entropy conservation. The cells are colored according to the number of active stages  $E_p^{(r)}$  for the third-order method  $E_3$ . The number of active stages  $E_3^{(r)}$  is determined based on the shortest edge length  $h$  of each cell.

while the pressure is computed analogous to the base pressure (4.4) as

$$p(t, \mathbf{x}) = \frac{\rho^\gamma(t, \mathbf{x})}{\gamma \text{Ma}_\infty^2}. \quad (4.7)$$

The vortex is initially centered in the  $\Omega = [-L, L]^2, L = 10$  domain equipped with periodic boundary conditions.

As for the previous testcase, we employ  $k = 3$  local solution polynomials. To discretize  $\Omega$ , a non-uniform, conforming mesh consisting of  $32 \times 32$  cells is used. This is obtained by mapping the uniformly discretized reference coordinates  $\xi \in [-1, 1]^2$  to the physical domain via the transformation

$$\begin{pmatrix} x \\ y \end{pmatrix} = L \begin{pmatrix} \text{sgn}(\xi_1) |\xi_1|^{1.4+|\xi_1|} \\ \text{sgn}(\xi_2) |\xi_2|^{1.4+|\xi_2|} \end{pmatrix} \quad (4.8)$$

which results in ”+”-like refined regions, cf. Fig. 6. The ratio of the smallest to largest element edge length is in this case roughly a factor of eight. To integrate the PDE on this uniform mesh efficiently, the following P-ERK/P-ERRK methods are constructed:  $E_2 = \{4, 6, 8, 10, 12, 16\}$ ;  $E_3 = \{4, 5, 6, 7, 8, 9, 10, 12, 16\}$ ;  $E_4 = \{5, 6, 7, 9, 11, 16\}$ . The mesh according to (4.8) is shown in Fig. 6 with element assignment corresponding to  $E_3$ .

We compute four passes through the domain ( $t_f = 80$ ) with a uniform timestep for all methods. As for the previous testcase we observe that the standard P-ERK methods exhibit entropy dissipation, cf. Fig. 7a, which is more significant for lower order of consistency. In turn, the P-ERRK methods with relaxation conserve the total entropy much better, with entropy fluctuations on the order of  $10^{-15}$ , cf. Fig. 7b. The relaxation parameter is determined using the standard Newton-Raphson method which stops after three iterations, if the residual is less or equal  $10^{-14}$  or the update step is less or equal  $10^{-15}$ . For this case, the second equality in (2.16) is enforced, i.e., the entropy at any timestep  $n$  is forced to be equal to the entropy of the initial condition  $H(U_0)$ . On average, these tolerances are met after one to two iterations.

#### 4.2. Conservation of Linear Invariants

We briefly demonstrate that the P-ERRK schemes do not violate linear invariants. To this end, we resort again to the isentropic vortex testcase as described in the previous section. Here, the compressible Euler equations are discretized on a  $32 \times 32$  uniform mesh with  $k = 3$  solution

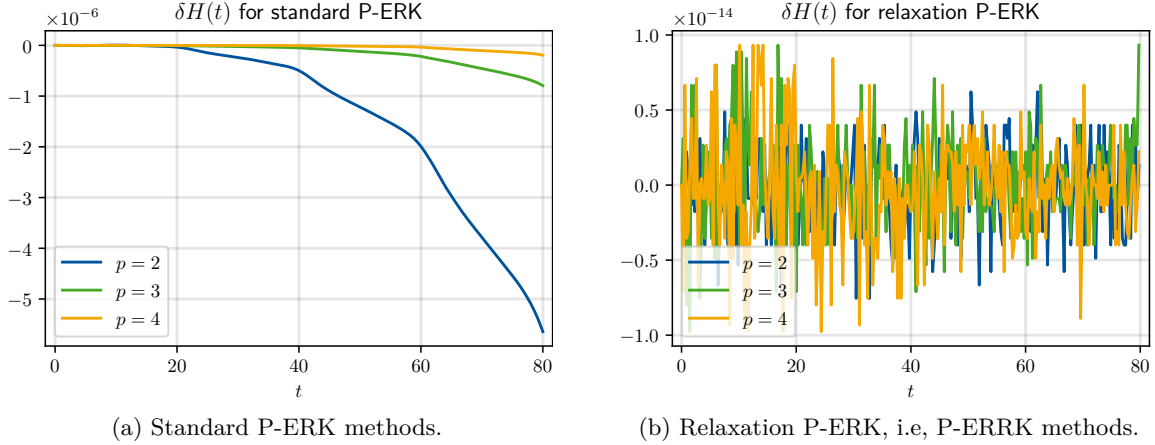


Figure 7: Temporal evolution of the total entropy defect  $\delta H(t)$  (4.2) for the isentropic vortex testcase for standard P-ERK methods (Fig. 7a) and P-ERRK methods with relaxation (Fig. 7b).

Table 1: Conservation-errors for isentropic vortex advection testcase after ten passes through the domain at  $t_f = 200$  for the fourth-order P-ERK scheme with and without relaxation and the ten-stage, fourth-order SSP method [90].

	P-ERK <sub>{5,...,15}</sub>	P-ERRK <sub>{5,...,15}</sub>	SSP <sub>10</sub> [90]
$e_\rho^{\text{Cons}}(t_f)$	$1.58 \cdot 10^{-13}$	$1.57 \cdot 10^{-13}$	$1.10 \cdot 10^{-12}$
$e_{\rho v_x}^{\text{Cons}}(t_f)$	$2.56 \cdot 10^{-14}$	$1.72 \cdot 10^{-14}$	$9.70 \cdot 10^{-13}$
$e_{\rho v_y}^{\text{Cons}}(t_f)$	$1.64 \cdot 10^{-14}$	$2.23 \cdot 10^{-14}$	$9.51 \cdot 10^{-13}$
$e_{\rho e}^{\text{Cons}}(t_f)$	$4.53 \cdot 10^{-13}$	$3.96 \cdot 10^{-13}$	$1.36 \cdot 10^{-11}$

polynomials. The Riemann problems at cell interfaces are solved approximately with the Harten-Lax-Van Leer-Contact (HLLC) flux [89] and we use a standard weak form volume integral. We compute ten passes through the domain, i.e.,  $t_f = 200$  with uniform timestep  $\Delta t = 0.01$  resulting in 20000 time steps. We limit ourselves to fourth-order,  $E = \{5, 6, \dots, 14, 15\}$  P-ERK schemes, both with and without relaxation. The 1024 grid cells are randomly assigned to one of the schemes to maximize the number of interfaces whose neighboring elements are integrated with different schemes. Note that interfaces between cells on different levels are always assigned to the higher-stage method. The conservation error

$$e_u^{\text{Cons}}(t_f) := \left| \int_{\Omega} u(t_f, \mathbf{x}) d\mathbf{x} - \int_{\Omega} u(t_0, \mathbf{x}) d\mathbf{x} \right| \quad (4.9)$$

is computed for mass, momenta and energy at final time and tabulated in Table 1. As the median number of stage evaluations is 10 we compare the conservation errors to the fourth-order, 10-stage, low-storage, SSP method by Ketcheson [90] which is implemented in `OrdinaryDiffEq.jl` [91]. This results in approximately  $2 \cdot 10^5$  ODE RHS calls across all methods, assuming even distribution of the grid cells among the P-ERRK schemes. We see from Table 1 that the conservation violation of both the P-ERK and P-ERRK schemes is on the order of round-off errors for double-precision floating point numbers. In particular, the conservation errors for the 10-stage SSP scheme are larger for every conserved quantity.

#### 4.3. Order of Convergence

To demonstrate that the relaxed P-ERK schemes still meet their designed order of accuracy we consider two classical test cases for compressible flows. These were also used in [38] to validate the relaxation methodology. In contrast to testcases based on manufactured solutions, these tests do not include source terms to match the constructed solution. First, to test inviscid,

i.e., hyperbolic problems we employ the isentropic vortex advection problem [69, 88] as described in the previous section. Second, in order to examine viscous, i.e., hyperbolic-parabolic problems we consider the viscous shock propagation problem [92–94]. For these testcases, the convergence studies are performed on non-uniform meshes, i.e., we employ multirate setups to test the convergence of the relaxed multirate P-ERK methods.

In addition, we test the relaxation methodology for systems involving non-conservative fluxes by means of the generalized Lagrangian multiplier magnetohydrodynamics (GLM-MHD) equations [95–97]. This testcase is performed on a uniform mesh where the cells are randomly assigned to one out of five P-ERRK family member schemes.

#### 4.3.1. Isentropic Vortex Advection

To demonstrate that the P-ERRK methods with relaxation maintain their designed order of accuracy we consider the isentropic vortex advection testcase with minimal spatial errors. To this end we employ  $k = 6$  DG solution polynomials on a  $64 \times 64$  base mesh, which is dynamically refined twice towards the center of the vortex. Precisely, the cells with distance  $r \in [3, 2)$  to the center of the vortex are refined once while the cells with  $r \in [2, 0]$  are refined twice. The vortex is parametrized exactly as in Section 4.1.2 where we demonstrated entropy conservation. Since currently only  $L^2$  projection/interpolation mortars [98] are implemented in Trixi.jl [82–84] this setup with AMR is not exactly entropy-conservative. We remark that a possible remedy to be explored in future work is the flux-correction method proposed in [99].

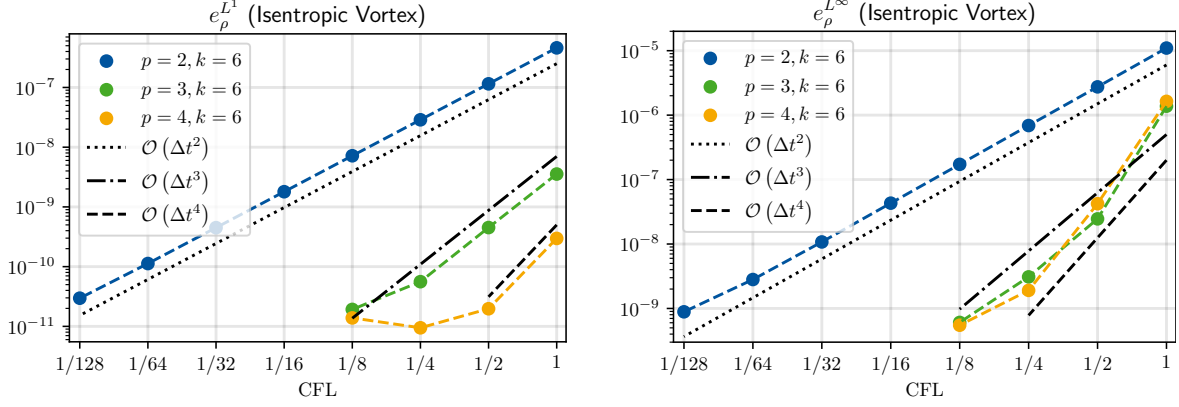
This setup allows for an initial domain-normalized  $L^1$ -error

$$e_{\rho}^{L^1}(t) := \frac{1}{|\Omega|} \int_{\Omega} |\rho(t, \mathbf{x}) - \rho_{\text{exact}}(t, \mathbf{x})| \, d\mathbf{x} \quad (4.10)$$

of order  $10^{-13}$ . This error is computed from the quadrature defect of the solution representation using the  $k = 6$  polynomials to  $\tilde{k} = 2 \cdot k = 12$  degree polynomials. The mesh is adapted 100 times over the course of the simulation, i.e., with time interval  $\Delta t_{\text{AMR}} = 0.2$  which is kept constant over the convergence study. We again use the HLLC [89] flux for the Riemann problems at cell interfaces and a standard weak form volume integral.  $L^1, L^\infty$ -errors of the density  $\rho$  are computed for  $E_2 = \{3, 6, 12\}$ ;  $E_3 = \{4, 8, 16\}$ ;  $E_4 = \{5, 9, 15\}$  P-ERRK schemes after one pass of the vortex. The base timestep  $\Delta t = 4 \cdot 10^{-3}$  is the same for all methods which is halved until the errors in density start to saturate due to the spatial discretization accuracy. To solve the relaxation equation we employ the Newton-Raphson method with a maximum of five iterations, a residual tolerance of  $10^{-13}$  for the  $p = 2$  method and  $10^{-14}$  for the  $p = 3, 4$  methods. For all orders of accuracy we supply a stepsize tolerance of double-precision machine epsilon.

For all schemes we observe the designed order of convergence in both  $L^1$  and  $L^\infty$  density errors, see Fig. 8. While the  $p = 2$  requires a significant reduction of the reference timestep to reach the spatial discretization limit, the  $p = 3$  and especially the  $p = 4$  schemes reach this limit earlier. In particular, we observe for the  $p = 4$  scheme that only the step from CFL = 1 to CFL = 0.5 reduces the  $L^1$  error by the expected factor of 16, before flattening out, cf. Fig. 8a. For the  $L^\infty$  error we observe superconvergence for the  $p = 3, p = 4$  schemes for the first reduction from CFL = 1 to CFL = 0.5, then one step with designed order of convergence, followed by a saturation of the error due to the spatial accuracy.

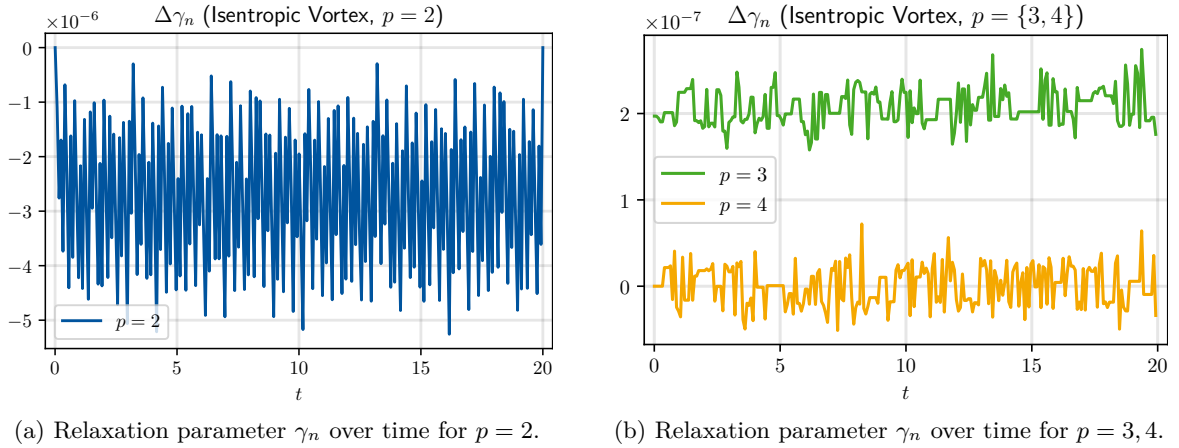
In Section 2.4 we mentioned that the desired order of convergence  $p$  should be reached for relaxation parameters that do not deviate too far from unity, i.e.,  $\gamma_n = 1 + \mathcal{O}(\Delta t^{p-1})$  [37, 38]. Thus, we exemplarily examine the evolution of the relaxation parameter  $\gamma_n$  over time for the CFL = 1 case for all schemes. In Fig. 9 we present the relaxation parameter sampled at every 20th timestep. We observe that the deviations  $\Delta\gamma_n$  from one scale as  $\mathcal{O}(10^{-(4+p)})$ . In particular, we have for the  $p = 4$  scheme that  $\Delta t^3 = 6.4 \cdot 10^{-8}$ , thus we are in safe waters according to theory. For the other two cases, i.e.,  $p = \{2, 3\}$  the deviations are even smaller in relation to  $\Delta t^{p-1}$  and thus convergence with the designed order of accuracy is expected and observed.



(a) Domain-normalized  $L^1$ -error in density  $\rho$ , cf. (4.10).

(b)  $L^{\infty}$  error in density  $\rho$ .

Figure 8:  $L^1$  (Fig. 8a) and  $L^{\infty}$  (Fig. 8b) errors of the density  $\rho$  for the isentropic vortex advection testcase after one pass through the domain for  $p = 2, 3, 4$  P-ERRK schemes.



(a) Relaxation parameter  $\gamma_n$  over time for  $p = 2$ .

(b) Relaxation parameter  $\gamma_n$  over time for  $p = 3, 4$ .

Figure 9: Evolution of the relaxation parameter  $\gamma_n$  for the isentropic vortex convergence testcase with  $\text{CFL} = 1$  for  $p = 2$  (Fig. 9a) and  $p = 3, 4$  (Fig. 9b) P-ERRK schemes. In the plots above, the deviation from unity, i.e.,  $\Delta\gamma_n := \gamma_n - 1$  is shown.

#### 4.3.2. Viscous Shock Propagation

To demonstrate that the P-ERRK methods with relaxation maintain their designed order of accuracy for entropy diffusive problems we consider the viscous shock propagation testcase. This testcase is constructed by balancing shock-formation due to the hyperbolic nonlinearity through diffusion, resulting in a time-invariant shock profile. Becker [92] was the first one to derive the a solution for the shock profile of the 1D Navier-Stokes-Fourier equations, i.e., taking both viscosity and heat conduction into account. This requires setting the Prandtl number  $\text{Pr} = \frac{3}{4} = c_p \frac{\mu}{\kappa} = \frac{\gamma}{\gamma-1} \frac{\mu}{\kappa}$  which is not too far from physical values for air and other gases. Becker's work was revisited by Morduchow and Libby [93] which showed that some of Becker's assumptions could be relaxed.

For a general parametrization, the solution for the 1D shock profile involves a nonlinear equation which needs to be solved numerically to obtain a solution to the Becker equation of motion [93, 94]. In [94], however, the authors show that for the Mach number  $\text{Ma} = \frac{2}{\sqrt{3-\gamma}}$ ,  $1 \leq \gamma \leq \frac{5}{3}$  an explicit solution is available. Here, we set  $\gamma = \frac{5}{3}$  (monatomic ideal gas), dynamic viscosity  $\mu = 0.15$ , reference density  $\rho_0 = 1$ , and shock speed  $v = 1$ . From this, we compute the Mach number, speed of sound ahead of the shock  $c_0 = \frac{v}{\text{Ma}}$ , and the reference pressure  $p_0 = c_0^2 \frac{\rho_0}{\gamma}$  which is computed from the fact that the enthalpy is constant across the shock. Furthermore, we have the length scale  $l = \frac{\mu}{\gamma-1} \frac{2\gamma}{\gamma-1} \frac{1}{\rho_0 v}$  [94]. Since the shock profile is moving with velocity  $v$ , the solution at any time  $t$  can be obtained by tracing back to the solution at initial position  $x_0(x, t) := x - vt$ . With characteristic position

$$\chi(x) := 2 \exp\left(\frac{x}{2l}\right) \quad (4.11)$$

and "effective momentum"

$$w(\chi) := 1 + \frac{1}{2\chi^2} \left(1 - \sqrt{1 + 2\chi^2}\right) \quad (4.12)$$

the primal variables are given by [94]

$$\rho(t, x) = \frac{\rho_0}{w} \quad (4.13a)$$

$$u(t, x) = v(1 - w) \quad (4.13b)$$

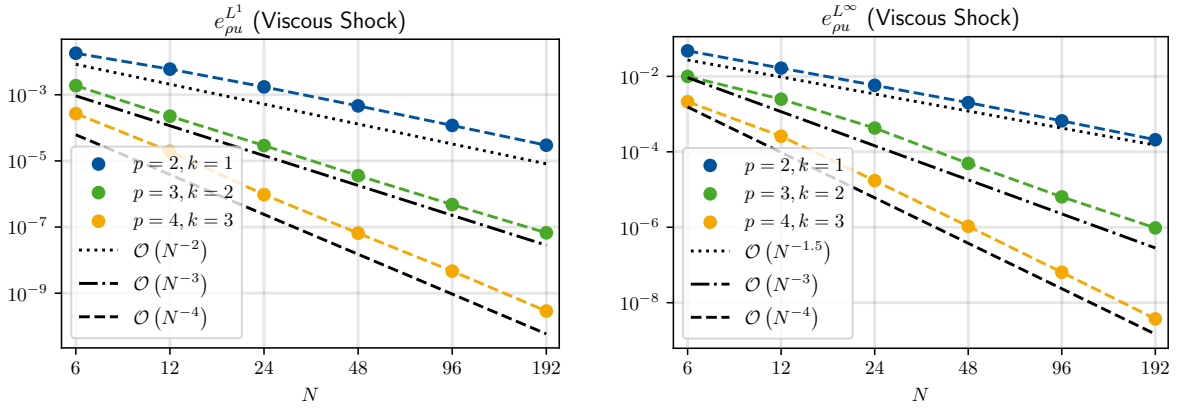
$$p(t, x) = \frac{p_0}{w} \left(1 + \frac{\gamma-1}{2} \text{Ma}^2 (1 - w^2)\right) \quad (4.13c)$$

where we abbreviate  $w \equiv w(\chi(x_0(x, t)))$ . The solution (4.13) at initial time is provided by Fig. B.21 in the appendix.

We solve this problem on  $\Omega = [-2, 2]$  up to  $t_f = 0.5$ . For the hyperbolic boundary conditions, i.e., the values for the inviscid fluxes, we use inflow conditions obtained from the analytical solution at the left boundary and (free) outflow conditions at the right boundary. The parabolic boundary conditions required for the viscous gradient fluxes are realized as moving isothermal, no-slip walls where velocity and temperature are obtained from the analytical solution. The surface fluxes are computed using the HLLE [80] flux and the viscous terms are discretized using the Bassi-Rebay 1 (BR1) scheme [100, 101]. Since this problem is diffusion-dominated we also tested the local Discontinuous Galerkin (LDG) method [102] with zero penalty parameter [103] which yields similar results. For the volume integral we use the standard weak form.

In contrast to the previous example we now refine simultaneously in space and time. The  $p = \{2, 3, 4\}$  P-ERRK schemes are combined with DG representations with polynomial degrees  $k = \{1, 2, 3\}$  to obtain discretizations of matching order of accuracy. The domain is refined in  $[-1, 1]$  by a factor of two and thus two-member P-ERRK families  $E_2 = \{4, 8\}$ ,  $E_3 = \{5, 9\}$ ,  $E_4 = \{6, 10\}$  are constructed for the semidiscretization at hand. Note that the considered flow is diffusion-dominated (with Reynolds number  $\text{Re} = \frac{\rho_0 v l}{\mu} = 1.875$ ) and thus the maximum stable





(a) Domain-normalized  $L^1$ -error in momentum  $\rho u$ , cf. (4.10).

(b)  $L^\infty$  error in momentum  $\rho u$ .

Figure 10:  $L^1$  (Fig. 8a) and  $L^\infty$  (Fig. 8b) errors of the density  $\rho$  for the viscous shock propagation test case at  $t_f = 0.5$  for  $p = 2, 3, 4$  P-ERRK schemes.

timestep scales quadratically with the smallest mesh size. We start the convergence study with a total of  $N = 6$  cells and refine the mesh five times up to  $N = 192$ . The timestep is set for all  $p$  to  $\Delta t = 0.035 \frac{\Delta x_{\min}^2}{v}$ . To solve the relaxation equation (3.3) we resort to the bisection procedure with parameters  $\gamma_{\min} = 0.8, \gamma_{\max} = 1.2$ . The root search is stopped at 25 iterations or if either the length of the bracketing interval or the residual of the relaxation equation is less or equal to  $10^{-15}$ .

$L^1$  and  $L^\infty$  errors of the momentum  $\rho u$  are presented in Fig. 10. We observe the designed order of convergence for all schemes, except for the  $L^\infty$  error of the  $p = 2$  which convergence with order 1.5. This is, however, not due to the P-ERRK scheme but instead a consequence of the linear solution polynomials. If  $k = 2$  degree solution polynomials are employed second order convergence in  $e_{\rho u}^{L^\infty}$  is observed also for the second-order method. We remark that essentially the same convergence results are obtained with the Newton-Raphson method. We also examine the evolution of the relaxation parameter  $\gamma_n$  for the viscous shock test case for  $N = 24$  grid cells. In this case, the deviations of  $\gamma_n$  are of order  $\mathcal{O}(10^{-5})$  for  $p = 2$  and for both  $p = 3, p = 4$  of same magnitude  $\mathcal{O}(10^{-7})$ , see Fig. B.22 in the appendix.

#### 4.3.3. Alfvén Wave

As the final validation study we consider the MHD equations in two spatial dimensions. The divergence constraint for the magnetic field

$$\nabla \cdot \mathbf{B} = 0 \quad (4.3)$$

is enforced using the generalized Lagrange multiplier method [95–97, 104]. The MHD equations with thermodynamically consistent divergence cleaning using the generalized Lagrangian multiplier (GLM) methodology [95–97] read in  $d$  spatial dimensions [104, 105]

$$\partial_t \mathbf{u} + \left[ \sum_{i=1}^d \partial_i \mathbf{f}_i(\mathbf{u}) \right] + \mathbf{g}(\mathbf{u}, \nabla \mathbf{u}) = \mathbf{0} \quad (4.14)$$

with unknown conserved variables  $\mathbf{u} = (\rho, \rho \mathbf{v}, E, \mathbf{B}, \psi)$ . The last variable  $\psi$  is due to the GLM extension of the system and corresponds to the propagation of the divergence errors. For a

two-dimensional problem the inviscid fluxes in  $x$  and  $y$  direction read

$$\mathbf{f}_x(\mathbf{u}) = \begin{pmatrix} \rho v_x \\ \rho v_x^2 + p + E_{\text{mag}} - B_x^2 \\ \rho v_x v_y - B_x B_y \\ v_x \left[ E_{\text{kin}} + \frac{\gamma}{\gamma-1} p + 2E_{\text{mag}} \right] - B_x [\mathbf{v} \cdot \mathbf{B}] \\ 0 \\ v_x B_y - v_y B_x \\ c_h B_x \end{pmatrix}, \quad (4.15a)$$

$$\mathbf{f}_y(\mathbf{u}) = \begin{pmatrix} \rho v_y \\ \rho v_x v_y - B_x B_y \\ \rho v_y^2 + p + E_{\text{mag}} - B_y^2 \\ v_y \left[ E_{\text{kin}} + \frac{\gamma}{\gamma-1} p + 2E_{\text{mag}} \right] - B_y [\mathbf{v} \cdot \mathbf{B}] \\ v_y B_x - v_x B_y \\ 0 \\ c_h B_y \end{pmatrix} \quad (4.15b)$$

with kinetic  $E_{\text{kin}} := \frac{1}{2} \rho \mathbf{v}^2$  and magnetic energy  $E_{\text{mag}} = \frac{1}{2} \mathbf{B}^2$ . The pressure  $p$  is computed via  $p = (\gamma - 1) \left[ E - E_{\text{kin}} - E_{\text{mag}} - \frac{1}{2} \psi^2 \right]$  where  $E = \rho e$  is the total energy. In the equations above,  $c_h$  is the divergence cleaning speed which is computed from a CFL-like condition. The nonconservative Powell term  $\mathbf{g}(\mathbf{u}, \nabla \mathbf{u})$  is given by [97, 104, 106]

$$\mathbf{g} = (\nabla \cdot \mathbf{B}) \begin{pmatrix} 0 \\ B_x \\ B_y \\ \mathbf{v} \cdot \mathbf{B} \\ v_x \\ v_y \\ 0 \end{pmatrix} + \partial_x \psi \begin{pmatrix} 0 \\ 0 \\ 0 \\ v_x \psi \\ 0 \\ 0 \\ v_x \end{pmatrix} + \partial_y \psi \begin{pmatrix} 0 \\ 0 \\ 0 \\ v_y \psi \\ 0 \\ 0 \\ v_y \end{pmatrix} \quad (4.16)$$

which vanishes in the (continuous or one-dimensional) divergence-free case.

To test convergence we consider the propagation of an Alfvén wave in the two-dimensional domain  $\Omega = [0, \sqrt{2}]^2$ . The solution for all  $t \in \mathbb{N}$  is given by [107, 108]

$$\mathbf{u}_{\text{Prim}} = \begin{pmatrix} \rho \\ v_x \\ v_y \\ p \\ B_x \\ B_y \\ \psi \end{pmatrix} = \begin{pmatrix} 1 \\ \frac{-0.1}{\sqrt{2}} \sin(\pi \sqrt{2}(x+y)) \\ \frac{0.1}{\sqrt{2}} \sin(\pi \sqrt{2}(x+y)) \\ 0.1 \\ \frac{1}{\sqrt{2}} - \frac{0.1}{\sqrt{2}} \sin(\pi \sqrt{2}(x+y)) \\ \frac{1}{\sqrt{2}} + \frac{0.1}{\sqrt{2}} \sin(\pi \sqrt{2}(x+y)) \\ 0 \end{pmatrix}. \quad (4.17)$$

Here, we run the simulations up to  $t_f = 2$ . The isentropic exponent is set to  $\gamma = 5/3$ . To discretize (4.14) we resort to the flux-differencing with separate fluxes for surface fluxes and volume fluxes. For these, again different fluxes are used for the conserved and inviscid fluxes. To begin, the conserved interface flux is simply the central flux, while for the non-conservative Powell term we use the specialized flux described in [97, 104]. For the conservative volume fluxes the Rusanov/Local Lax-Friedrichs flux [66] is employed while the non-conservative fluxes are discretized analogous to the surface fluxes.

Similar to the previous example simultaneous refinement in space and time is performed. Here, however, the spatial discretization is always of increased accuracy, i.e., we choose  $k = 2$

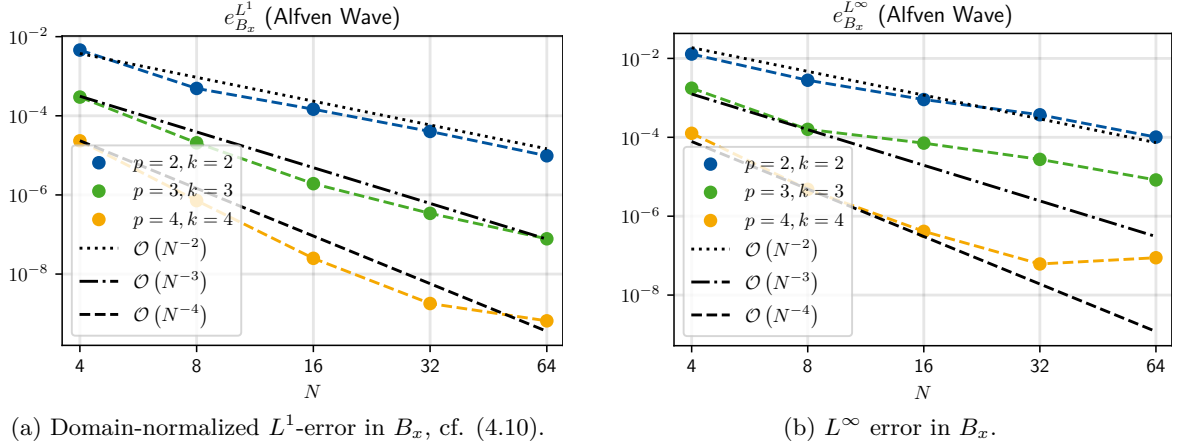


Figure 11:  $L^1$  (Fig. 8a) and  $L^\infty$  (Fig. 8b) errors of the  $x$ -component of the magnetic field  $B_x$  for the Alfvén wave test case at  $t_f = 2$  for  $p = 2, 3, 4$  P-ERRK schemes with random assignment.

polynomials for the  $p = 2$  P-ERRK scheme,  $k = 3$  polynomials for the  $p = 3$  scheme, and  $k = 4$  polynomials for the  $p = 4$  scheme. This way we ensure that the temporal errors should dominate the spatial errors in the asymptotic limit. For every order of consistency,  $E = \{10, 11, 12, 13, 14\}$  P-ERRK schemes are constructed which are randomly assigned to the uniform grid cells, similar to the test case for preservation of linear invariants Section 4.2. The relaxation equation is solved with the Newton-Raphson method with a maximum of 10 iterations, root-residual tolerance and minimum step tolerance of  $10^{-15}$ .

As for the previous test cases, the expected order of convergence is observed for all schemes for the  $L^1$  (4.10) error in  $x$ -component of the magnetic field  $B_x$ , cf. Fig. 11a. For the  $L^\infty$  error we observe for  $p = 3$  and  $p = 4$  a reduced order of convergence which we attribute to the random assignment of the schemes to the grid cells. In particular, the constituting schemes of the P-ERRK schemes possess different error constants. Since the individual schemes are no longer assigned to the same cells/locations across the convergence study, schemes with different error constants appear at points with different solution features during the study. Thus, convergence in  $L^\infty$  is not guaranteed, as observed for the  $p = 3$  scheme and the last refinement of the  $p = 4$  scheme. We remark that this is not an issue inherent to the relaxation approach, as we observe the same behaviour for the standard/non-relaxed schemes. Plots of the relaxation parameter  $\gamma_n$  for the  $N = 64^2$  discretization are provided by Fig. B.23 in the appendix. Interestingly,  $\gamma$  shows for  $p = 2$  and  $p = 3$  a periodic behaviour, in contrast to the chaotic behaviour observed for the other examples and the  $p = 4$  scheme.

In addition, we also studied the convergence for a round-robin assignment of the  $R = 5$  schemes to the grid cells for  $t_f = 4$ . For  $R = 5$  schemes this results for  $N = 2^n$ ,  $n = 3, \dots, 6$  grid cells in interfaces between schemes for every cell, both in  $x$  and in  $y$  direction. As for the random assignment, we observe the expected order of convergence in  $L^1$  while the  $L^\infty$  error deviates from the expected asymptotic convergence for the  $p = 3$  and  $p = 4$  scheme for the last two refinement steps, cf. Fig. B.24. As for the random assignment, this is due to the different error constants of the schemes and not an artifact of the relaxation approach, as we confirmed by performing the same convergence study with the standard P-ERRK schemes.

## 5. Applications

In this section we apply the P-ERRK methods to a range of different flow regimes of increasing complexity. We begin by considering three two-dimensional examples. First, we study the laminar, viscous, effectively incompressible flow over the SD7003 airfoil in Section 5.1. This problem can be seen as an extended test case as it allows validating the P-ERRK methods by

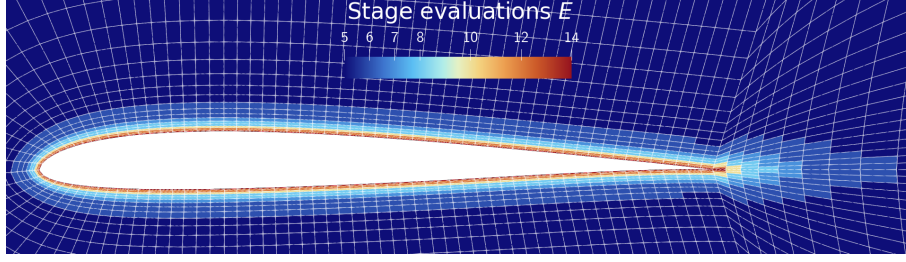


Figure 12: Method distribution for the SD7003 airfoil integration with the  $E = \{5, 6, 7, 8, 10, 12, 14\}$  multirate P-ERK family.

comparing aerodynamic coefficients to reference data and is not characterized by complicated flow features. Next, we consider the flow of a magnetized, viscous, compressible fluid around a cylinder in Section 5.2, which is described by the VRMHD equations [104, 105]. Then, we turn our attention to the inviscid, transonic flow around the NACA0012 airfoil. The testcase discussed in Section 5.3 corresponds to case C1.2 of the third international workshop on high-order computational fluid dynamics methods held in 2015 [109]. We apply AMR to this problem to resolve the steady standing shock on the airfoil top surface. Coming to three-dimensional problems, we consider the classic ONERA M6 wing [110, 111] in Section 5.4 for an inviscid, compressible gas, i.e., also a steady setup. Additionally, we investigate the robustness of the relaxed multirate schemes by means of a viscous transonic flow across the NASA CRM on a very coarse grid in Section 5.5.

All computations are performed using the Trixi.jl [82–84] package and can be reproduced using the repository [86].

### 5.1. Viscous Laminar Flow over SD7003 Airfoil

#### 5.1.1. Setup

As a first application case, we reconsider the laminar, viscous flow over the SD7003 airfoil presented in [47]. This testcase was also employed in the original P-ERK papers [45, 46].

The flow parameters for this Navier-Stokes-Fourier simulation are  $\text{Ma} = 0.2 = \frac{U_\infty}{c_\infty}$ ,  $\text{Re} = 10^4 = \frac{\rho_\infty U_\infty l}{\mu_\infty}$  with airfoil chord length  $l = 1.0$ , angle of attack  $\alpha = 4^\circ$ , non-dimensionalized speed of sound  $c_\infty = 1.0$ , pressure  $p_\infty = 1.0$ , and density  $\rho_\infty = 1.4$  corresponding to isentropic exponent  $\gamma = 1.4$ . The viscosity is kept constant at  $\mu = 2.8 \cdot 10^{-5}$  and the Prandtl number is set to  $\text{Pr} = 0.72$ . At the domain boundaries the freestream flow is weakly enforced [112] for both inviscid and viscous fluxes (gradients). The airfoil is modeled as a no-slip, adiabatic wall. The simulation is initialized with the freestream values.

We employ a two-dimensional mesh consisting of 7605 straight-sided quadrilateral elements. This mesh (with second-order elements) has been provided as electronic supplementary material to the second-order P-ERK paper [45]. The spatial derivatives are discretized using the DGSEM with  $k = 3$  polynomials and HLLC numerical flux [89] with volume flux differencing [21] and entropy-conservative volume flux [23]. The gradients required for the viscous fluxes are computed with the BR1 scheme [100, 101]. We optimize fourth-order,  $E = \{5, 6, 7, 8, 10, 12, 14\}$  P-ERK/P-ERRK schemes for the free-stream state. The distribution of the composing schemes of the near-airfoil grid is depicted in Fig. 12.

Lift and drag coefficients  $C_L, C_D$  are recorded over the  $t \in [30t_c, 35t_c]$  interval where  $t_c := t \frac{U_\infty}{c}$  is a non-dimensionalized convective time. The provided lift coefficient is solely due to the pressure difference:

$$C_L = C_{L,p} = \oint_{\partial\Omega} \frac{p \mathbf{n} \cdot \mathbf{t}^\perp}{0.5 \rho_\infty U_\infty^2 L_\infty} dS \quad (5.1)$$

with  $\mathbf{t}^\perp = (-\sin(\alpha), \cos(\alpha))$  being the unit direction perpendicular to the free-stream flow. The vector  $\mathbf{n}$  is the fluid-element outward-pointing normal, i.e., the normal pointing into the surface

Table 2: Time-averaged lift and drag coefficients  $\overline{C}_L$  and  $\overline{C}_D$  for the SD7003 airfoil over the  $[30t_c, 35t_c]$  interval.

Source	$\overline{C}_L$	$\overline{C}_D$
P-ERRK $p = 4, k = 3$	0.3827	0.04995
P-ERK $p = 2, k = 3$ [45]	0.3841	0.04990
P-ERK $p = 3, k = 3$ [46]	0.3848	0.04910
Uranga et al. [113]	0.3755	0.04978
López-Morales et al. [114]	0.3719	0.04940

of the airfoil. The drag coefficient incorporates also the viscous stress contribution:

$$C_D = C_{D,p} + C_{D,\mu} \quad (5.2a)$$

$$C_{D,p} = \oint_{\partial\Omega} \frac{p \mathbf{n} \cdot \mathbf{t}}{0.5 \rho_\infty U_\infty^2 L_\infty} dS \quad (5.2b)$$

$$C_{D,\mu} = \oint_{\partial\Omega} \frac{\boldsymbol{\tau}_w \cdot \mathbf{t}}{0.5 \rho_\infty U_\infty L_\infty} dS \quad (5.2c)$$

where  $\mathbf{t} = (\cos(\alpha), \sin(\alpha))$ . The wall shear stress vector  $\boldsymbol{\tau}_w$  is obtained from contracting the viscous stress tensor  $\underline{\underline{\boldsymbol{\tau}}}$  with the surface normal  $\hat{\mathbf{n}} = -\mathbf{n}$ :

$$\boldsymbol{\tau}_w = \underline{\underline{\boldsymbol{\tau}}} \hat{\mathbf{n}} = \begin{pmatrix} \tau_{xx} & \tau_{xy} \\ \tau_{yx} & \tau_{yy} \end{pmatrix} \begin{pmatrix} -n_x \\ -n_y \end{pmatrix}. \quad (5.3)$$

The unsteady lift and drag coefficients, cf. Fig. B.26, are sampled every  $\Delta t_c = 5 \cdot 10^{-3}$  and averaged to enable comparison with values from the literature, see Table 2. We observe good agreement with values reported in the literature [45, 46, 113, 114]. In particular, the lift and drag coefficients of the relaxed fourth-order P-ERRK scheme deviate only by  $\mathcal{O}(10^{-6})$  from the values of the plain fourth-order P-ERK scheme developed in [47].

### 5.1.2. Performance Comparison

To begin, we demonstrate performance improvements of the P-ERK scheme with relaxation over the plain P-ERK scheme. For the given configuration, the CFL number can be increased by roughly 20 %, which results in about  $25 \cdot 10^3$  fewer total simulation steps, which manifests in a 19 % decreased runtime, despite the additional overhead due to computation of the relaxation parameter  $\gamma$ . Similar values are obtained for the standalone  $S = E = 14$  P-ERRK scheme when compared to the non-entropy-stable  $S = 14$  P-ERK scheme. We attribute this observation to the increased robustness of the P-ERRK scheme compared to the standard scheme, cf. Section 3.2. This is particularly important given that the flow is not fully resolved, cf. Fig. B.25 which results in artifacts at the cell boundaries.

For the multirate P-ERRK scheme, the relaxation solver makes up for a total of 2.7 % of the total runtime, out of which 1.9 % are spent on computing the entropy difference  $\Delta H$  (3.2). This is a relatively expensive operation as it involves integration over the physical domain, which in turn demands the transform from reference to physical space for every element. Here, some code optimization could be possible e.g. by embodying this integration in the DG solution process.

Second, we compare the performance of the entropy-conservative, multirate scheme with entropy-stable, standalone schemes. Besides the natural comparison with the optimized  $S = E = 14$  P-ERRK scheme, we consider three other fourth-order accurate Runge-Kutta schemes which permit a low-storage implementation in Butcher form. This guarantees a fair comparison of the P-ERRK schemes to other entropy-stable methods. In particular, we consider two "purely

sub-diagonal” schemes, i.e., methods with Butcher tableau

$$\begin{array}{c|c|c}
 i & \mathbf{c} & A \\
 \hline
 1 & 0 & \\
 2 & c_2 & c_2 \\
 3 & c_3 & 0 & c_3 & \\
 \vdots & \vdots & \vdots & \ddots & \ddots \\
 S & c_S & 0 & \dots & 0 & c_S \\
 \hline
 & & \mathbf{b}^T
 \end{array} \quad (5.4)$$

The classic four-stage, fourth-order Runge-Kutta schemes can be classified as a purely sub-diagonal scheme of form (5.4). Furthermore, the six-stage, fourth-order low-dispersion, low-dissipation scheme proposed in [115] is also of this form.

In addition, we consider the five-stage, fourth-order Runge-Kutta scheme optimized for compressible Navier-Stokes equations from [116]. The method considered here is implemented in van-der-Houwen form [117], i.e., with Butcher tableau archetype

$$\begin{array}{c|c|c}
 i & \mathbf{c} & A \\
 \hline
 1 & 0 & \\
 2 & c_2 & a_{21} \\
 3 & c_3 & b_1 & a_{32} \\
 4 & c_4 & b_1 & b_2 & a_{43} \\
 \vdots & \vdots & \vdots & \vdots & \ddots & \ddots \\
 S & c_S & b_1 & b_2 & \dots & b_{S-2} & a_{S,S-1} \\
 \hline
 & & b_1 & b_2 & \dots & b_{S-2} & b_{S-1} & b_S
 \end{array} \quad (5.5)$$

For all considered methods, the relaxation equation (3.3) is solved with the Newton-Raphson method which stops after five iterations, for objective residual less or equal  $10^{-13}$  and stepsizes less or equal to  $10^{-13}$ . This set of parameters is motivated by our findings in section Section 4.1, in particular the two-dimensional examples. For this configuration, very few Newton iterations are required to reach the desired accuracy which mainly concentrate on the first few time steps after the initialization.

We compare the observed ratios of measured runtime to optimal (i.e., P-ERRK-Multi) runtime  $\tau/\tau^*$  and scalar (i.e., per degree of freedom (DoF)) RHS evaluations

$$N_{\text{RHS}} = N_t \cdot N_K \quad (5.6)$$

for the aforementioned schemes in Table 3. In (5.6),  $N_t$  the number of timesteps taken and  $N_K$  is the number of scalar RHS evaluations involving all stages. For the multirate schemes the latter is computed as

$$N_K = \sum_{r=1}^R E^{(r)} \cdot M^{(r)} \quad (5.7)$$

where  $M^{(r)}$  is the number of DoFs integrated with the  $r$ -th partition. For standard schemes,  $N_K = S \cdot M$  where  $M$  the dimension of the semidiscretization (2.2) and  $S$  is the number of stages. The values in Table 2 correspond to the run from  $t = 0$  to  $t = 30t_c$  to eliminate skewed results due to the frequent computation of the lift and drag coefficients.

The multirate P-ERRK scheme is the most efficient method both in terms of runtime and number of scalar RHS evaluations. In particular, the P-ERRK-Multi scheme is twice as fast

Table 3: Runtimes and number of scalar RHS evaluations (5.6) of different entropy conservation, relaxed fourth-order integrators compared to the optimized  $p = 4, E = \{5, 6, 7, 8, 10, 12, 14\}$  integrator for the laminar flow around the SD7003 airfoil. We also included the non-relaxed P-ERK $_{4;\{5,6,\dots,14\}}$  scheme.

Method	$\tau/\tau^*$	$N_{\text{RHS}}/N_{\text{RHS}}^*$
P-ERRK $_{4;\{5,6,\dots,14\}}$	1.0	1.0
P-ERRK $_{4;14}$	2.13	2.42
P-ERK $_{4;\{5,6,\dots,14\}}$	1.19	1.20
R-RK $_{4;4}$	2.55	2.77
R-TS $_{4;6}$ [115]	2.98	3.16
R-CKL $_{4;5}$ [116]	2.38	2.53

as the optimized  $p = 4, S = E = 14$  scheme, which is the most efficient standalone scheme. The number of RHS calls is reduced by a factor of 2.42, i.e., the P-ERRK-Multi scheme requires roughly 42 % of the scalar RHS evaluations of the optimized standalone scheme. The discrepancy between the saved computations and runtime is a consequence of the bookkeeping overhead for the multirate scheme and the loss of data locality which leads to suboptimal performance due to, e.g., cache misses. The other considered schemes require at least 2.5 times scalar RHS evaluations and are at least 2.3 times slower than the optimized P-ERRK-Multi scheme.

### 5.2. Visco-Resistive MHD Flow past a Cylinder

In this example we consider the VRMHD equations in two spatial dimensions. The VRMHD equations with divergence cleaning using the GLM methodology [95–97] read in  $d$  spatial dimensions [104, 105] (cf. (4.14))

$$\partial_t \mathbf{u} + \left[ \sum_{i=1}^d \partial_i (\mathbf{f}_i(\mathbf{u}) - \mathbf{f}_i^{\text{vr}}(\mathbf{u}, \nabla \mathbf{u})) \right] + \mathbf{g}(\mathbf{u}, \nabla \mathbf{u}) = \mathbf{0} \quad (5.8)$$

with unknown conserved variables  $\mathbf{u} = (\rho, \rho \mathbf{v}, E, \mathbf{B}, \psi)$ . The last variable  $\psi$  is due to the GLM extension of the system and corresponds to the propagation of the divergence errors. The visco-resistive fluxes  $\mathbf{f}_i^{\text{vr}}$  are given by [104, 105]

$$\mathbf{f}_x^{\text{vr}}(\mathbf{u}, \nabla \mathbf{u}) = \begin{pmatrix} 0 \\ \mu \tau_{xx} \\ \mu \tau_{xy} \\ \mu [\mathbf{v} \cdot \boldsymbol{\tau}_x - q_x] + \eta B_y [\partial_x B_y - \partial_y B_x] \\ 0 \\ \eta [\partial_x B_y - \partial_y B_x] \\ 0 \end{pmatrix}, \quad (5.9a)$$

$$\mathbf{f}_y^{\text{vr}}(\mathbf{u}, \nabla \mathbf{u}) = \begin{pmatrix} 0 \\ \mu \tau_{yx} \\ \mu \tau_{yy} \\ \mu [\mathbf{v} \cdot \boldsymbol{\tau}_y - q_y] + \eta B_x [\partial_y B_x - \partial_x B_y] \\ \eta [\partial_y B_x - \partial_x B_y] \\ 0 \\ 0 \end{pmatrix}. \quad (5.9b)$$

In the definitions above,  $\mu$  is the dynamic viscosity and  $\eta$  the magnetic resistivity. The symmetric stress tensor  $\underline{\underline{\tau}}$  is given by

$$\underline{\underline{\tau}} := \begin{pmatrix} \tau_x \\ \tau_y \end{pmatrix} = \begin{pmatrix} \frac{4}{3} \partial_x v_x - \frac{2}{3} \partial_y v_y & \partial_x v_y + \partial_y v_x \\ \partial_y v_x + \partial_x v_y & \frac{4}{3} \partial_y v_y - \frac{2}{3} \partial_x v_x \end{pmatrix}. \quad (5.10)$$

The heat flux  $\mathbf{q}$  is given by Fourier's law  $\mathbf{q} = -\kappa \nabla T$  with thermal conductivity  $\kappa = \frac{\gamma}{\gamma-1} \frac{1}{\text{Pr}}$  and temperature  $T$ . The Prandtl number  $\text{Pr}$  is a parameter of the considered gas and treated here as a constant with value  $\text{Pr} = 0.72$ . The conserved fluxes  $\mathbf{f}_i$  are given by (4.15) and the nonconservative Powell term  $\mathbf{g}$  is given by (4.16).

### 5.2.1. Setup

The flow of a magnetized fluid past a cylinder has been studied both numerically and experimentally [118–120]. The configuration employed here is loosely based on the setup described in [105]. Most importantly, we also set the Mach number  $\text{Ma} = 0.5$ , rendering the flow truly compressible. The ratio of specific heats is set to  $\gamma = \frac{5}{3}$  and the Reynolds number based on the diameter of the cylinder  $D = 1$  is set to  $\text{Re} = \frac{\rho_\infty v_\infty D}{\mu} = 200$ . Following [105], the Alfvénic Mach number  $A = \frac{v_A}{v_\infty}$  is set to  $A = 0.1$ . This defines the magnitude of the magnetic field  $B_\infty = v_A \sqrt{\rho_\infty}$ . With this Alfvénic Mach number the viscous Lundquist number is  $S_\mu = A \cdot \text{Re} = \frac{\rho_\infty v_\infty D}{\mu} = 50$ . We choose  $v_\infty = p_\infty = 1$ , thus  $\rho_\infty$  follows from the speed of sound  $c = \frac{v_\infty}{\text{Ma}}$  of an ideal gas as  $\rho_\infty = p_\infty \frac{\gamma}{c^2}$ . Again, as in [105] we use the same values for the viscous and resistive Lundquist numbers  $S_\mu = S_\eta$ . Then, the magnetic resistivity is given by  $\eta = \frac{v_A D}{S_\eta}$ .

The cylinder is placed at  $(0, 0)$  in the rectangular domain  $\Omega = [-5D, 60D] \times [-10D, 10D]$ . The computational mesh is generated using **HOHQMesh** [121] which enables the generation of conforming high-order, i.e., curved-boundary quadrilateral meshes. In this case, the mesh uses fourth-order boundaries, consists of 2258 elements and is symmetric around the  $y = 0$  axis, cf. Fig. B.27.

The hyperbolic boundary conditions imposed at  $\partial\Omega$  are weakly enforced Dirichlet conditions [112] based on the initial/freestream condition. At the cylinder surface a slip-wall boundary condition [122] with zero magnetic field is imposed. The parabolic boundary conditions of the cylinder are no-slip, adiabatic, and isomagnetic  $\mathbf{B} = \mathbf{0}$  walls. At the inlet, i.e., left boundary, the parabolic boundary condition imposes a moving, adiabatic, isomagnetic fluid with velocity  $v_x = v_\infty$  and purely horizontal magnetic field  $B_x = B_\infty$ . On the other boundaries, i.e., top, bottom and outlet/right boundary the gradients are just copied which corresponds to domain-extending boundary conditions. The simulation is initialized with the uniform inflow state.

The solution fields are approximated with  $k = 3$  DG solution polynomials. The Riemann problems due to the inviscid fluxes (4.15) are approximately solved with the Harten-Lax-Van Leer (HLL) two-wave solver [123] with Davis-type wave speed estimates [124]. As for the previous example, the viscous fluxes are computed with the BR1 scheme [100, 101]. The nonconservative Powell term (4.16) is solved with the specialized numerical flux described in [97, 104]. Opposed to the standard Navier-Stokes-Fourier equations the simulation of a magnetized fluid requires stabilization. To this end, we employ the entropy-stable shock-capturing technique by means of the first-order finite volume method on the subcells of the DG scheme [81, 125]. The required volume fluxes are the entropy conservation and kinetic energy preserving flux [87] which extends the flux by Ranocha [26] to the MHD equations. The nonconservative volume fluxes are treated with the same numerical flux as the nonconservative surface fluxes.

We simulate the flow until  $t_f = 120$  such that the vortex street is fully developed and reaches the outlet boundary. Upon inspection of the mesh (cf. Fig. B.27) it becomes apparent that roughly four base cell sizes (minimum edge length) are present: Cells with  $h \approx 0.25$  at the cylinder,  $h \approx 0.5$  in the near wake,  $h \approx 1$  in the far wake, and  $h \approx 2$  at the top and bottom boundary. Thus, we seek to find a four-member P-ERRK family for which the admissible timestep roughly doubles for each family member. For the fourth-order methods the  $E = \{5, 6, 8, 13\}$  scheme fulfills this requirement and is thus used.

To solve the relaxation equation (3.3) we employ the Newton-Raphson procedure which stops at 3 iterations or if the residual tolerance is less or equal  $10^{-14}$ . For this simulation we employ a linear ramp-up of the CFL number, cf. (2.8), from a small value  $\text{CFL}_0$  which is required to overcome the naive initial condition to a maximum value for the developed flow  $\text{CFL}_{\max}$ . Thus,



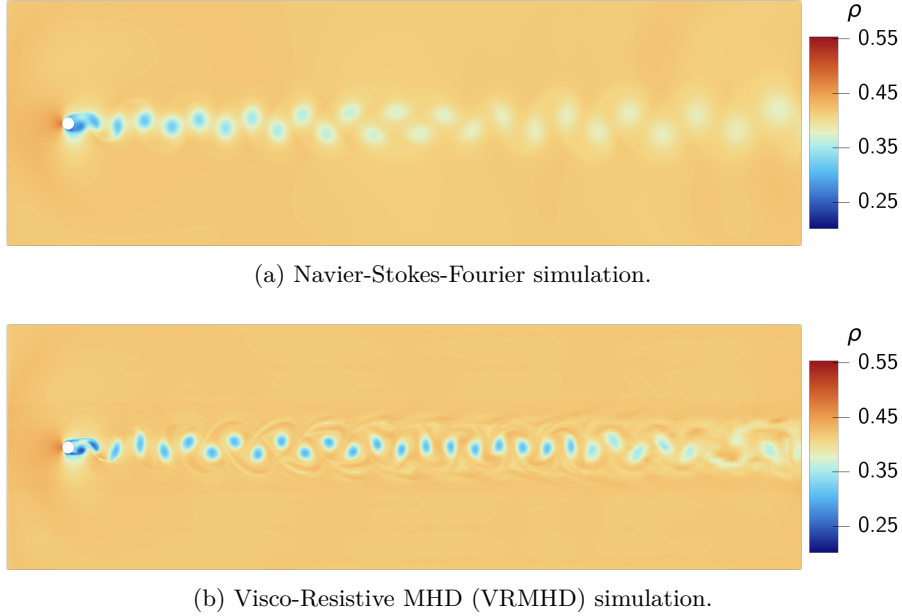


Figure 13: Density  $\rho$  at final time  $t_f = 120$  for the flow past a cylinder. In Fig. 13a the Navier-Stokes-Fourier simulation is shown, while Fig. 13b depicts the visco-resistive MHD simulation. Both results are obtained using fourth-order P-ERRK schemes optimized for the respective semidiscretization.

the CFL number as a function of time  $t$  is given by

$$\text{CFL}(t) = \min \left\{ \text{CFL}_{\max}, \text{CFL}_0 + (\text{CFL}_{\max} - \text{CFL}_0) \frac{t}{t_{\text{CFL}}} \right\} \quad (5.11)$$

where the ramp-up time  $t_{\text{CFL}}$  determines how quickly the maximum CFL number is reached. The maximum CFL numbers  $\text{CFL}_{\max}$  have been obtained by starting the simulations from a physical initial condition at  $t = 10$  and increasing the CFL number until the simulation produces unphysical results.

We plot the density  $\rho$  at final time  $t_f = 120$  for a standard Navier-Stokes-Fourier simulation and the visco-resistive MHD simulation in Fig. 13. As observed for instance in [105] the magnetic field alters the regular vortex structures in the wake of the cylinder. This is in contrast to the plain diffusion of the vortical structures observed in the Navier-Stokes-Fourier simulation.

### 5.2.2. Performance Comparison

For this example, the P-ERRK does not come with improved CFL numbers compared to the standard P-ERK. The additional work due to the relaxation process accounts for 3.6 % of the total runtime. Additionally, the multirate P-ERRK scheme requires one more timestep (4537 vs. 4536 steps corresponding to the base scheme.) Across schemes, we observe that on average a single Newton iteration is required to solve the relaxation equation (3.3) to the desired accuracy.

Turning to the comparison to the standalone relaxed entropy-stable schemes we observe that these require at least 76 % more scalar RHS evaluations, manifesting in 81 % to 207 % longer runtimes. As for the previous example, the five-stage scheme  $\text{CKL}_{4,5}$  [116] is the most efficient out of the non-optimized, off-the-shelf schemes.

Upon closer inspection of the results it is evident that the off-the-shelf schemes are over-proportionally slow in relation to the number of RHS evaluations. This is partly due to the dense weight vector  $\mathbf{b}$  of these schemes, which requires in turn more integrations to compute the entropy change  $\Delta H$ , cf. (3.2). Note that the  $p = 4$  P-ERRK schemes have only non-zero  $b_1$  and  $b_S$ , independent of the number of stages  $S$  [47]. In the present implementation, each stage is integrated on-the-fly, resulting for the standard schemes in  $S$  integrations per total timestep. This could be reduced, however, by accumulating the integrand of (3.2) in an additional vector.

Table 4: Runtimes and number of scalar RHS evaluations (5.6) of different entropy conservation, relaxed fourth-order integrators compared to the optimized  $p = 4, E = \{5, 6, 8, 13\}$  integrator for the VRMHD flow around a cylinder.

Method	$\tau/\tau^*$	$N_{\text{RHS}}/N_{\text{RHS}}^*$
P-ERRK $_{4;\{5,6,8,13\}}$	1.0	1.0
P-ERRK $_{4;13}$	1.81	1.76
R-RK $_{4;4}$	2.69	2.53
R-TS $_{4;6}$ [115]	3.07	2.73
R-CKL $_{4;5}$ [116]	2.01	1.76

This would then store the scalar product of the stage values  $\mathbf{W}_{n,i}$  and stages  $\mathbf{K}_i$  evaluated at every DG node  $j$ . In particular, one can not immediately accumulate each elements' contribution into a single scalar sum as in this case information on the geometry is lost which is required to compute the integral. Nevertheless, computing the integrand makes up for about only 5 % of the total runtime which could be reduced to 1 – 2% with the aforementioned optimization.

### 5.3. Inviscid Transonic Flow over NACA0012 Airfoil with Adaptive Mesh Refinement

As a first inviscid example we consider the transonic flow over the NACA0012 airfoil. We follow the C1.2 testcase of the third installment of the International Workshop on High-Order CFD Methods which took place in 2015 [109]. Furthermore, we demonstrate that the P-ERRK schemes can also be used efficiently in conjunction with AMR, following upon a previous study [68].

#### 5.3.1. Setup

For this testcase, the Mach number is set to  $\text{Ma} = 0.8$ , the ratio of specific heats is  $\gamma = 1.4$ , and the angle of attack is  $\alpha = 1.25^\circ$ . A range of uniformly refined fifth-order quadrilateral large meshes (farfield boundary placed 1000 cords from the airfoil center) are provided online [109] in `gmsh` [126] format. We employ the medium resolution mesh with 2240 cells truncated to second-order and  $k = 3$  solution polynomials for our computations. The surface fluxes are discretized using the Rusanov/Local Lax-Friedrichs flux [66] and we use the flux-differencing shock-capturing procedure [81] with the entropy-stable flux by Chandrashekar [23]. For time integration  $p = 4$ ,  $E = \{5, 6, 7, 8, 10, 12, 14\}$  P-ERRK schemes are constructed. The airfoil surface is modeled as a slip wall with no penetration [122] involving the analytic solution of the pressure Riemann problem [127]. At the outer boundaries the freestream flow is weakly enforced [112].

We split the overall simulation into two steps: First, we use the provided mesh to advance the simulation until the shock position is approximately constant. Here, we run the simulation until  $t_f = 100$  which corresponds to a convective time  $t_c = t \frac{U_\infty}{c} = t \cdot \text{Ma} = 80$ . As in the previous example, a ramp up of the CFL number (5.11) is used to avoid immediate breakdown after initialization the flow field with the freestream state and unnecessary small timesteps at later times. For all considered time integration schemes the ramp-up time is set to  $t_{\text{CFL}} = 1.5$ . This is then followed by a restarted run where we allow for cells to being refined up to three times, i.e., 8 times smaller than the base cell size which allows to resolve the shock much sharper, cf. Fig. B.28. As indicator we reuse the shock sensor that also governs the stabilization [81] which employs the product of density and pressure  $\rho \cdot p$  as indicator variable. The simulation with adaptive mesh refinement is run for 80 additional convective time units, i.e., until  $t_f = 200$ .

For both simulation runs we use the Newton method to solve the relaxation equation. The iterations are forced to stop after 5 steps, relaxation equation (3.3) residual less or equal to  $10^{-12}$ , or stepsize  $\Delta\gamma$  less or equal to  $10^{-13}$ . Interestingly, the entropy defect due to the considered Runge-Kutta methods is for this setup negligible, i.e., the unrelaxed ( $\gamma = 1$ ) Runge-Kutta

Table 5: Runtimes and number of scalar RHS evaluations (5.6) of different entropy conservation, relaxed fourth-order integrators compared to the optimized  $p = 4, E = \{5, 6, 7, 8, 10, 12, 14\}$  integrator for the transonic inviscid flow around the NACA0012 airfoil.

Method	1 <sup>st</sup> run (static)		2 <sup>nd</sup> run (AMR)	
	$\tau/\tau^*$	$N_{\text{RHS}}/N_{\text{RHS}}^*$	$\tau/\tau^*$	$N_{\text{RHS}}/N_{\text{RHS}}^*$
P-ERRK <sub>4;\{5,\dots,14\}</sub>	1.0	1.0	1.0	1.0
P-ERRK <sub>4;14</sub>	1.49	1.55	2.27	2.46
R-RK <sub>4;4</sub>	3.59	3.22	2.54	2.18
R-TS <sub>4;6</sub> [115]	4.08	3.55	2.95	2.68
R-CKL <sub>4;5</sub> [116]	2.54	2.33	1.64	1.88

scheme satisfies the relaxation equation to desired accuracy. This is in contrast to the previous viscous examples where usually some Newton-Raphson updates to the relaxation parameter were required.

### 5.3.2. Performance Comparison

Comparisons of recorded runtime and computational effort are provided in Table 5. For the first run on the static mesh we observe that the optimized standalone P-ERRK scheme is performing remarkably well, which is due to a comparatively high stable CFL number. For the second run on the adaptively refined mesh, however, R-CKL<sub>4;5</sub> [116] is the most efficient standalone scheme. Thus, linear stability is no longer the timestep-limiting factor in this case, but nonlinear stability, i.e., positivity preservation. We would like to remark that the re-initialization of the additional partitioning P-ERRK datastructures is of negligible cost, as it contributes only about 0.1% to the overall runtime. The entire AMR procedure is also very efficient, as it amounts to merely 3.3% of the recorded runtime.

We compute pressure-based lift (5.1) and drag (5.2b) coefficients  $C_{L,p}, C_{D,p}$  at final time  $t_f = 200$ , i.e., on the adapted mesh. These are compared to the data of Giangaspero et al. [128] who employ fifth-order SBP operators on a shock-fitted mesh with  $577 \times 513$  vertices. Thus, this mesh has about  $2.96 \cdot 10^5$  DoF per solution field which is significantly more than the  $\sim 4.2 \cdot 10^4$  DoF of the adaptively refined mesh used in our simulation. Reference values for the lift and drag coefficients given in [128] are  $C_{L,\text{ref}} = 3.51607 \cdot 10^{-1}$  and  $C_{D,\text{ref}} = 2.26216 \cdot 10^{-2}$ . Based on these, we compute relative errors of the lift and drag coefficients

$$e_{C_{\{L;D\}}} := \frac{|C_{\{L;D\}} - C_{\{L;D\},\text{ref}}|}{C_{\{L;D\},\text{ref}}} \quad (5.12)$$

at final time  $t_f = 200$  and averaged over the last 20 time units. For all time integrators, the final lift and drag coefficients match the given reference data quite well, with relative errors for  $e_{C_L} \sim 0.15\% - 0.26\%$  and  $e_{C_D} \sim 1.4\% - 2.3\%$ . For the averaged coefficients  $\bar{C}_{\{L;D\}}$  we obtained similar values for the relative errors of the mean values. Additionally, the pressure coefficient

$$C_p(x) := \frac{p(x) - p_\infty}{0.5 \rho_\infty U_\infty^2 L_\infty} \quad (5.13)$$

obtained from the multirate P-ERRK simulation is provided in Fig. 14. This is again in good agreement with the submitted data of the participants of the workshop [109, 128], except for a small defect at  $x \approx 0.08$  on the top surface where a higher resolution seems to be required.

### 5.4. Inviscid Transonic Flow over ONERA M6 Wing

We consider the transonic flow over the ONERA M6 wing, a well-known benchmark problem for compressible flow solvers. In our study we follow the geometry as presented in [110], although

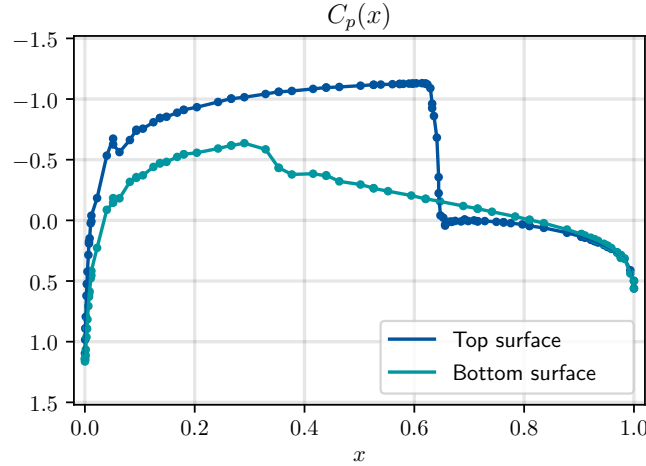


Figure 14: Pressure coefficient (5.13) recorded at top (blue) and bottom (petrol) NACA0012 airfoil surface. The dots correspond to the values recorded at the surface nodes.

we employ a rescaled variant with wingspan set to 1. A sketch of the wing geometry in the  $x-z$  plane is given by Fig. 15a. Details on the chamber of the wing are also provided in the cited reference.

#### 5.4.1. Setup

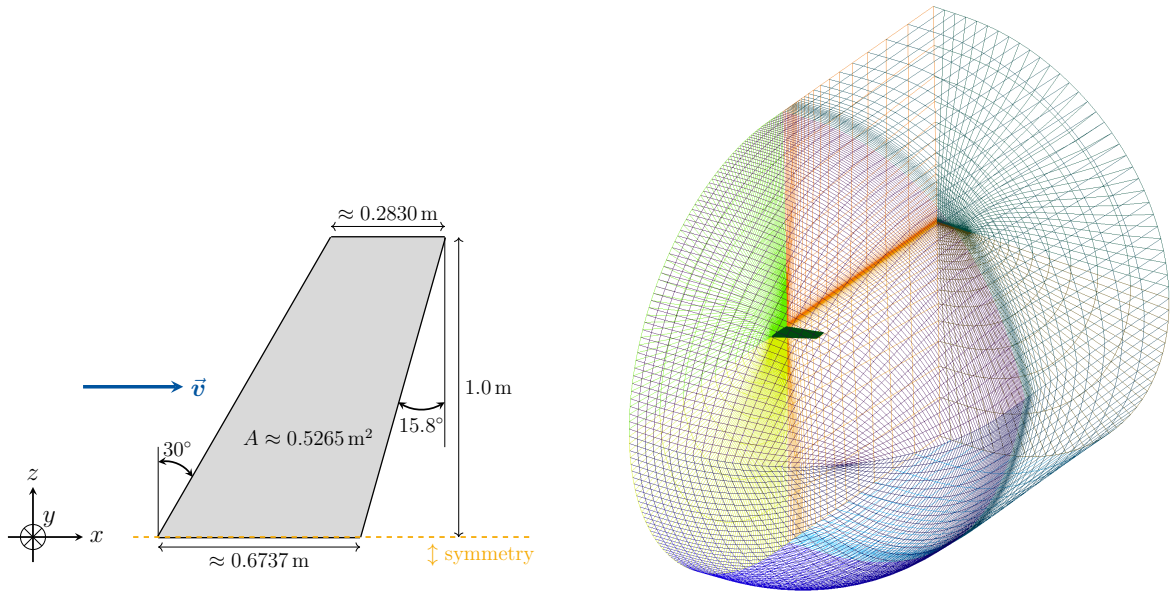
The classic configuration is given by  $Ma = 0.84$ , angle of attack of  $\alpha = 3.06^\circ$  and Reynolds numbers  $Re \sim \mathcal{O}(12 \cdot 10^6)$ . Here, we consider the purely hyperbolic scenario ( $Re = \infty$ ) to avoid any need for turbulence modeling.

For the geometry proposed in [110] a purely hexahedral mesh is available for download from publicly available NASA webpages as part of the NPARC Alliance Validation Archive [111]. The mesh as published is split into four different blocks (cf. edge coloring in Fig. 15b) where a united version in `gmsh` format is available from the HiSA repository [129]. Subsequently, we deleted duplicated nodes originating from different blocks and replaced node labels accordingly. Additionally, some mesh sanitizing was necessary to make this grid compatible with the DG methodology as implemented in `Trixi.jl`. In particular, 72 hexahedra are degenerated into prisms, i.e., neighboring hexahedra that share six instead of four nodes and edges. Those were easily sanitized by merging the two neighboring effective prisms into a single hexahedron. Unfortunately, two additionally elements on the wing surface were corrupted in a way that they share 5 nodes/edges, which prevents such an easy fix. To resolve this, we deleted the corrupted elements and remeshed locally using `gmsh` [126] which finally enabled us to use the mesh which consists now of 294838 straight-sided elements. The final sanitized mesh is publicly available as part of the reproducibility repository which we provide [86]. The mesh extends in  $x$ -direction from  $-6.373$  to  $7.411$ , in  $y$ -direction from  $-6.375$  to  $6.375$  and in  $z$ -direction from  $0$  to  $7.411$ . The 2D element edges are depicted for illustration in Fig. 15b.

At  $z = 0$  plane symmetry is enforced by rotating the symmetry-plane crossing velocity  $v_z$  to zero and copying density and pressure from the domain. At all other outer boundaries we weakly enforce [112] the freestream flow. The wing surface is modeled as a slip-wall [122] with an analytic solution of the pressure Riemann problem [127].

We represent the solution using  $k = 2$  degree element polynomials which results in about 40 million total DoF, i.e., roughly 8 million unknowns per solution field. The surface fluxes are computed with the Rusanov/Local Lax-Friedrichs flux [66]. To stabilize the simulation it suffices in this case to use the flux-differencing approach [7, 15, 16, 21, 22]. The arising volume fluxes are discretized using the entropy-stable and kinetic-energy preserving flux by Ranocha [26].

The simulation is initialized with the freestream values and we run the simulation until  $t_f = 6.05$  for which the timings are obtained from the last 0.01 time units.



(a) Rescaled ONERA M6 wing geometry following [110, 111]. (b) Computational mesh (2D/surface element edges).

Figure 15: ONERA M6 wing geometry Fig. 15a and used computational mesh Fig. 15b. The displayed mesh is the sanitized version of the mesh from [111]. Note that the  $y$ -axis points into the plane in Fig. 15a and correspondingly upwards in Fig. 15b.

We compute the lift coefficient (5.1) for  $\alpha = 3.06^\circ$  based on the reference area  $A_\infty \approx 0.5265$ . We obtain a lift coefficient of  $C_L \approx 0.2951$  which is about 3% larger of what is reported in one of the tutorials of the SU2 code [130]. This might be due to the fact that in the latter case the actual area of the wing is used which is necessarily larger than the projected referenced area  $A_\infty$  (which we employ) due to the curvature of the wing. In that tutorial a lift coefficient of  $C_L \approx 0.2865$  is reported, obtained from a second-order in space, first-order in time simulation on a  $\sim 5.8 \cdot 10^5$  element tetrahedral mesh. The classic lambda shock profile on the upper wing is displayed in Fig. 16.

#### 5.4.2. Performance Comparison

For multirate time integration third-order P-ERRK schemes with stage evaluations  $E = \{3, 4, \dots, 14, 15\}$  are optimized for the discretized freestream state. The Runge-Kutta tableaus are constructed using the variant described in [68] which avoids negative entries, i.e., stage-downwinding in contrast to the original formulation [46], see also (A.2).

As for the previous cases, we compare the P-ERRK schemes to low-storage, standalone relaxed entropy-stable schemes of matching order in Butcher form. A natural choice for the "subdiagonal" methods cf. (5.4) is the three-stage scheme RK<sub>3,3</sub> by Ralston [131] since it has the minimum error bound among the  $p = 3, S = 3$  methods [131]. In [116] a four-stage, third-order scheme with  $2N$ -storage van-der-Houwen (5.5) implementation is presented which we employ here for comparison. The multirate scheme is significantly more efficient than the considered standalone schemes, requiring only about a quarter of the number of RHS evaluations. This improvement compared to the fourth-order schemes is mainly due to the fact that here the minimum number of stage evaluations is  $\min_r E^{(r)} = 3$ , compared to 5 for the fourth-order schemes. In terms of runtime, however, we observe that the savings are unfortunately not as pronounced. This is mostly due to non-ideal parallel scaling of the partitioned Runge-Kutta solver, which is due to distribution of too few data across too many computing units (threads) on the finest levels. A possible remedy to this would be to use a constant ratio of DoFs per computing unit. Unfortunately, reducing the number of parallel computing units, i.e., threads

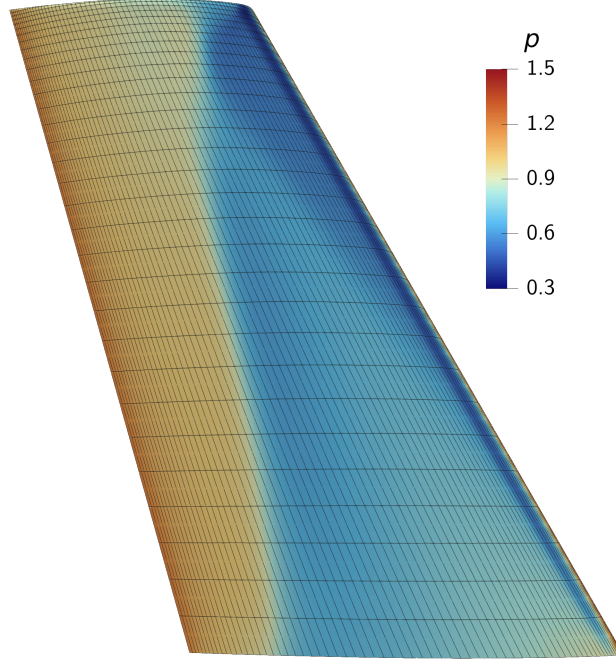


Figure 16: Pressure  $p$  on the ONERA M6 wing's upper surface at  $t_f = 6.05$ . The lambda shock pattern refers to the shape formed by the shock at the leading edge, where the pressure drops significantly below the ambient value of  $p = 1$ , and the standing shock across the wing across which the pressure increases again. Note that in contrast to Fig. 15a the  $y$ -axis points in this figure out of the view plane.

Table 6: Runtimes and number of scalar RHS evaluations (5.6) of different entropy conservation, relaxed third-order integrators compared to the optimized  $p = 3, E = \{3, 4, \dots, 14, 15\}$  integrator for the flow over the ONERA M6 wing.

Method	$\tau/\tau^*$	$N_{\text{RHS}}/N_{\text{RHS}}^*$
P-ERRK <sub>3;{3,...,15}</sub>	1.0	1.0
P-ERRK <sub>3;15</sub>	2.98	3.92
R-RK <sub>3;3</sub>	3.79	4.26
R-CKL <sub>3;4</sub> [116]	3.54	4.14

in certain parts of the program is currently not (natively) supported by the Julia programming language.

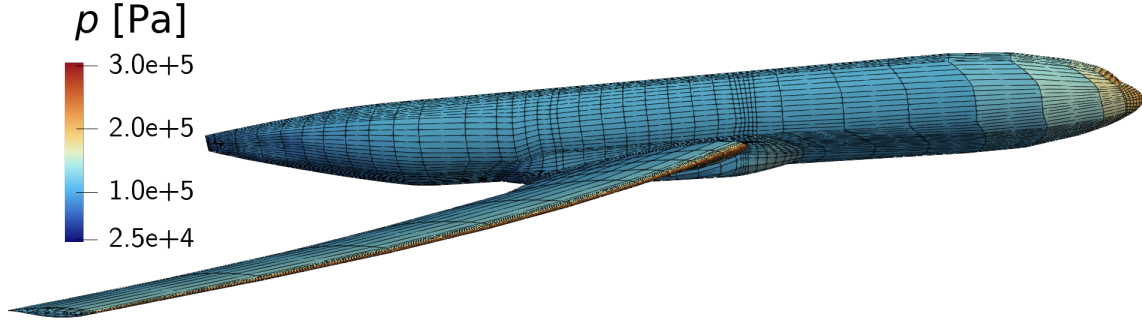
### 5.5. Viscous Transonic Flow over NASA Common Research Model (CRM)

As the final example we consider the viscous transonic flow over the NASA CRM [132] which was also considered in the 2015 International Workshop on High-Order CFD Methods [109]. Here, we also use the transonic Mach number  $\text{Ma} = 0.85$  but increase the Reynolds number to  $\text{Re} = 200 \cdot 10^6$  which is based on the wing reference chord of 7.005 m. This configuration allows us to demonstrate increased robustness of the P-ERRK schemes compared to the standard ones. As for the NACA0012 airfoil, a mesh consisting of 79505 hexahedra is provided online [109] which we use for our computations. This mesh is way too coarse to resolve the flow accurately, but yet allows us to demonstrate the benefit of the relaxation approach for the multirate P-ERK schemes.

#### 5.5.1. Setup

The solution fields are represented using  $k = 2$  polynomials, which results in about 2.1 million DoF per solution field. The surface fluxes are discretized using the HLL two-wave solver [123] with Davis-type wave speed estimates [124]. We stabilize the simulation using the subcell



Figure 17: Pressure  $p$  [Pa] and surface mesh for the NASA CRM at  $t_f = 1.5 \cdot 10^{-5}$  s.Table 7: Runtimes and number of scalar RHS evaluations (5.6) of different entropy conservation, relaxed third-order integrators compared to the optimized  $p = 3, E = \{3, 4, 5, 7, 8, 9, 10, 11, 12, 15\}$  integrator for the flow over the NASA CRM aircraft.

Method	$\tau/\tau^*$	$N_{\text{RHS}}/N_{\text{RHS}}^*$
P-ERRK $_{3;\{3,\dots,15\}}$	1.0	1.0
P-ERRK $_{3;15}$	3.67	3.02
R-RK $_{3;3}$	3.51	2.85
R-CKL $_{3;4}$ [116]	3.87	3.04

limiting approach [81] with the entropy-stable and kinetic energy preserving flux by Ranocha [26] for the volume fluxes. The viscous gradients are discretized with the BR1 scheme [100, 101]. The ratio of specific heats is set to  $\gamma = 1.4$ , the Prandtl number is set to 0.72, and the viscosity is computed from the Reynolds number and is constant across the domain. The aircraft is modeled as a no-slip adiabatic wall, the freestream values are weakly enforced at the farfield boundaries [112]. Symmetry across the  $z$ -plane is enforced by rotating the velocity component  $v_z$  to zero and eliminating heat transfer across the plane (adiabatic). No turbulence modeling is employed. For this semidiscretization a third-order P-ERRK scheme with  $E = \{3, 4, 5, 7, 8, 9, 10, 11, 12, 15\}$  is constructed and we compare against the  $S = 15$  optimized standalone, CKL $_{3;4}$  [116] and RK $_{3;3}$  [131] schemes. The relaxation equation is solved using Newton iterations, limited to five steps, objective residual less or equal to  $10^{-13}$ , and stepsize  $\Delta\gamma$  less or equal to  $10^{-13}$ .

### 5.5.2. Performance Comparison

To begin, we highlight that the relaxed scheme maintains positivity 22 % longer than the standard scheme ( $\sim 1.97 \cdot 10^{-5}$  s vs.  $\sim 1.61 \cdot 10^{-5}$  s). Restarting the simulation from  $1.5 \cdot 10^{-5}$  s with a smaller CFL number shows the same behaviour, where the relaxed scheme runs again about 20 % longer (after restart) than the plain P-ERK method before breaking down ( $3.26 \cdot 10^{-5}$  s vs.  $2.97 \cdot 10^{-5}$  s). Thus, we observe the same stabilizing effect of the relaxation methodology as encountered for the Kelvin-Helmholtz instability, recall Section 3.2.2. For illustration, we provide a snapshot of the pressure field and the surface mesh at  $t_f = 1.5 \cdot 10^{-5}$  s in Fig. 17.

In terms of improved performance compared to the standalone schemes, we observe significant savings in runtime and number of RHS evaluations for the multirate P-ERRK scheme. In particular, RHS evaluations are reduced by a factor of about three, while the runtime is decreased even further, with speedups ranging from 3.51 to 3.87.

## 6. Conclusions

In this work we presented a novel class of entropy conservation/stable high-order, optimized, multirate time integration schemes suitable for the integration of convection-dominated com-

pressible flow problems. These schemes are based on the P-ERK methods and allow for the same non-intrusive implementation based on a coefficient-based partitioned semidiscretization. The P-ERRK methods maintain the same order of accuracy as the corresponding P-ERK methods, preserve linear invariants such as mass, momentum, and energy, and introduce no defects in the global entropy. We have shown that the P-ERK schemes benefit significantly from the relaxation approach, as it enhances robustness of the multirate schemes. In particular, this is demonstrated for underresolved viscous flows, where the schemes with relaxation maintain positivity for longer time intervals or are stable for larger CFL numbers. This is due to the relaxation parameter  $\gamma$  acting as an adaptive timestep controller, which in turn has a limiting effect.

We have shown that the P-ERRK schemes outperform standard Relaxation-Runge-Kutta methods for a collection of problems, ranging from low Mach and low Reynolds number flow regimes to transonic inviscid and viscous flows. We highlight here the flow of a magnetized fluid around a cylinder governed by the VRMHD equations, the transonic inviscid flow over a NACA0012 airfoil with AMR and the simulation of the ONERA M6 wing. Depending on the problem, RHS evaluations are reduced by factors up to four and speedups in excess of three are observed.

In future work we will explore the application of the P-ERRK schemes to flows involving explicit turbulence modeling. In addition, the construction of implicit-explicit (IMEX) P-ERK/P-ERRK schemes is of interest, for instance for simulations involving chemical reactions.

## Data Availability

All data generated or analyzed during this study are included in this published article and its supplementary information files.

## Code Availability & Reproducibility

We provide a reproducibility repository publicly available on GitHub [86].

## Acknowledgments

Funding by German Research Foundation (DFG) under Research Unit FOR5409: "Structure-Preserving Numerical Methods for Bulk- and Interface-Coupling of Heterogeneous Models (SNuBIC)" (grant #463312734).

The authors are grateful for Andrew Winters' assistance in generation of the symmetric mesh for the visco-resistive MHD flow past a cylinder.

## Declaration of competing interest

The authors declare the following financial interests/personal relationships which may be considered as potential competing interests: Daniel Doebling's financial support was provided by German Research Foundation.

## CRedit authorship contribution statement

**Daniel Doebling:** Conceptualization, Methodology, Software, Validation, Investigation, Writing - original draft.

**Hendrik Ranocha:** Methodology, Software, Writing - review & editing.

**Manuel Torrilhon:** Conceptualization, Funding acquisition, Supervision, Writing - review & editing.



## Appendix A. P-ERK Butcher Tableau Archetypes

In Section 2.2 we discussed the central properties of the P-ERK schemes. Here, we present the structural archetypes for the P-ERK/P-ERRK schemes for orders of consistency  $p = 2, 3, 4$ .

### Appendix A.1. Second-Order Scheme

The archetype for the second-order P-ERK is given by (2.10).

### Appendix A.2. Third-Order Scheme

The archetype of the third-order P-ERK schemes as presented in [46] is given by

$i$	$\mathbf{c}$	$A^{(r)}$
1	0	
2	$c_2$	$c_2$
3	$c_3$	$c_3 - a_{3,2} \quad a_{3,2}$
$\vdots$	$\vdots$	$\vdots$
$S-2$	$c_{S-2}$	$c_{S-2} - a_{S-2,S-3} \quad \dots \quad a_{S-2,S-3}$
$S-1$	$1/3$	$1/3 - a_{S-1,S-2} \quad 0 \quad 0 \quad a_{S-1,S-2}$
$S$	1	$1 - a_{S,S-1} \quad 0 \quad 0 \quad 0 \quad a_{S,S-1}$
	$\mathbf{b}^T$	$0 \quad 0 \quad 0 \quad 0 \quad 3/4 \quad 1/4$

(A.1)

where the superscript  $(\cdot)^{(r)}$  has been truncated in the coefficients  $a_{i,j}$  of the  $A$ -matrix for the sake of compactness. While this scheme has the sparsest weight vector  $\mathbf{b}^T$ , it comes at the cost that the  $E = S = 3$  scheme has negative entry  $a_{3,1} = -1$  [68]. This corresponds to undesired downwinding [71] of the  $\mathbf{K}_1$  stage in the construction of the  $i = 3$  intermediate approximation  $\mathbf{U}_3$ , cf. (2.7b). Thus, we derived in [68] a new scheme which avoids this issue by basing the third-order scheme on the  $E = S = 3$  Shu-Osher scheme [69]. This leads to the following Butcher tableau

$i$	$\mathbf{c}$	$A^{(r)}$
1	0	
2	$c_2$	$c_2$
3	$c_3$	$c_3 - a_{3,2} \quad a_{3,2}$
$\vdots$	$\vdots$	$\vdots$
$S-2$	$c_{S-2}$	$c_{S-2} - a_{S-2,S-3} \quad \dots \quad a_{S-2,S-3}$
$S-1$	1	$1 - a_{S-1,S-2} \quad 0 \quad 0 \quad a_{S-1,S-2}$
$S$	$1/2$	$1 - a_{S,S-1} \quad 0 \quad 0 \quad 0 \quad a_{S,S-1}$
	$\mathbf{b}^T$	$1/6 \quad 0 \quad 0 \quad 0 \quad 1/6 \quad 2/3$

(A.2)

We emphasize that the usage of the first Runge-Kutta stage  $\mathbf{K}_1$  in the final update step does not increase storage requirements of the scheme as  $\mathbf{K}_1$  is always kept in memory to compute the intermediate approximations  $\mathbf{U}_i$ . Also, the computational costs per stage stay at two scalar-vector multiplications and one vector-vector addition.

We have not yet mentioned how to choose the free abscissae  $c_i, i = 2, \dots, S-2$ . In this work, we set

$$c_i = \frac{i-1}{S-3}, \quad i = 1, \dots, S-2 \quad (\text{A.3})$$

which corresponds to a linear distribution of timesteps between  $c_1 = 0$  and  $c_{S-2} = 1$ , similar to the second-order case [45]. We remark that more sophisticated choices of the abscissae  $\mathbf{c}$  are possible, for instance to improve the internal stability properties of the scheme [133].

*Appendix A.3. Fourth-Order Scheme*

In [47] we derived a fourth-order P-ERK scheme which is based on a  $S = 5$  method. In contrast to the second- and third-order schemes, additional coupling conditions in the order conditions arise which render the construction of the Butcher tableau more involved. We were able to find the one-parameter family

$i$	$\mathbf{c}$	$A^{(r)}$					
1	0						
2	$c_2$	$c_2$					
3	$c_3$	$c_3 - a_{3,2}$	$a_{3,2}$				
$\vdots$	$\vdots$	$\vdots$	$\ddots$				
$S-2$	$c_{S-2}$	$c_{S-2} - a_{S-2,S-3}$	$\dots$	$a_{S-2,S-3}$			
$S-1$	$0.5 + \frac{\sqrt{3}}{6}$	$0.5 + \frac{\sqrt{3}}{6} - a_{S-1,S-1}$	0	$\dots$	$a_{S-1,S-2}$		
$S$	$0.5 - \frac{\sqrt{3}}{6}$	$0.5 - \frac{\sqrt{3}}{6} - a_{S,S-1}$	0	$\dots$	0	$a_{S,S-1}$	
		0	0	0	0	0.5	0.5

(A.4)

with

$$c_{S-2} = 0.479274057836310 \tag{A.5a}$$

$$c_{S-1} = 0.5 + \frac{\sqrt{3}}{6} = 0.788675134594813 \tag{A.5b}$$

$$c_S = 0.5 - \frac{\sqrt{3}}{6} = 0.211324865405187 \tag{A.5c}$$

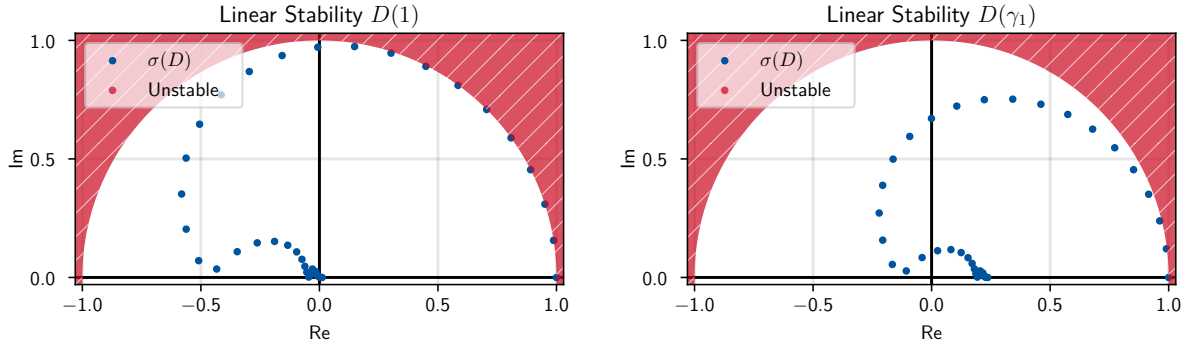
$$a_{S-2,S-3} = \frac{0.114851811257441}{c_{S-3}} \tag{A.5d}$$

$$a_{S-1,S-2} = 0.648906880894214 \tag{A.5e}$$

$$a_{S,S-1} = 0.0283121635129678 \tag{A.5f}$$

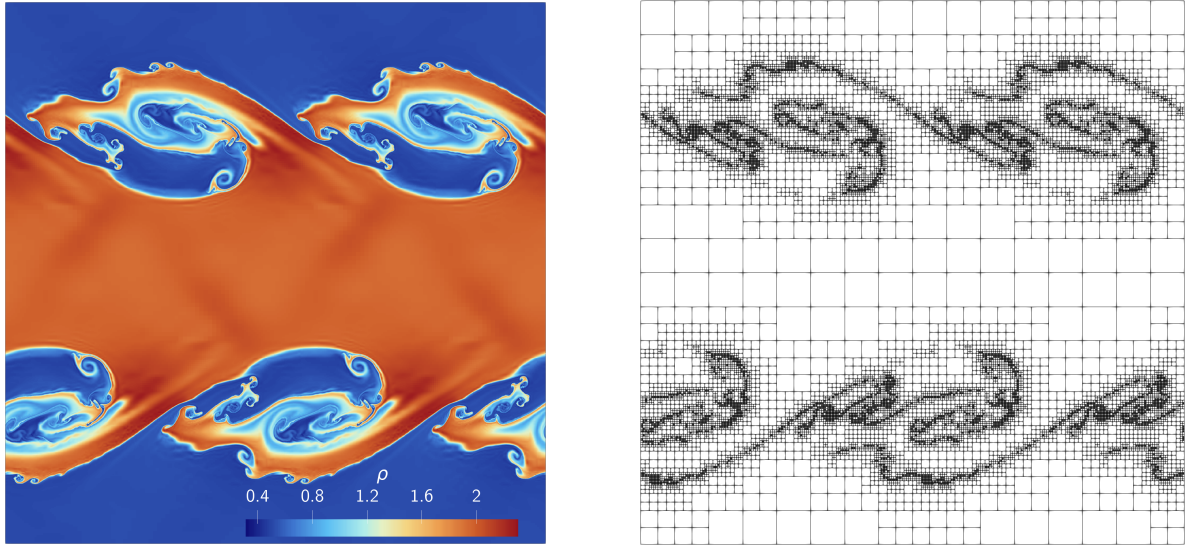
where  $c_{S-3}$  is a free parameter, as the remaining abscissae  $c_i, i = 2, \dots, S-3$ . In [47] we demonstrated that setting all of these to unity results in the scheme with the best internal stability properties, given the restriction that  $c_i \leq 1$ .

## Appendix B. Supplementary Figures



(a) Spectrum of the update matrix  $D$  corresponding to the standard P-ERK scheme. (b) Spectrum of the relaxed update matrix  $D(\gamma_1)$  corresponding to the relaxed P-ERK scheme.

Figure B.18: Section 3.2.1: Spectra  $\sigma(D)$  of the fully discrete matrices  $D(\gamma)$  of the P-ERK $_{2;\{8,16\}}$  scheme applied to (3.8). The unstable region with  $|\lambda| > 1$  is shaded in red. The spectrum of the update matrix  $D$  corresponding to the standard P-ERK scheme is shown in Fig. B.18a, while the spectrum of the relaxed update matrix  $D(\gamma_1)$  corresponding to the relaxed P-ERK scheme is shown in Fig. B.18b.



(a) Density  $\rho$  at final time  $t_f = 3.2$  for the Kelvin-Helmholtz instability test case.

(b) Adaptive mesh at final time  $t_f = 3.2$  for the Kelvin-Helmholtz instability test case.

Figure B.19: Section 3.2.2: Density  $\rho$  (Fig. B.19a) and adaptive mesh (Fig. B.19b) at final time  $t_f = 3.2$  for the Kelvin-Helmholtz instability test case obtained with the relaxed multirate P-ERRK scheme.

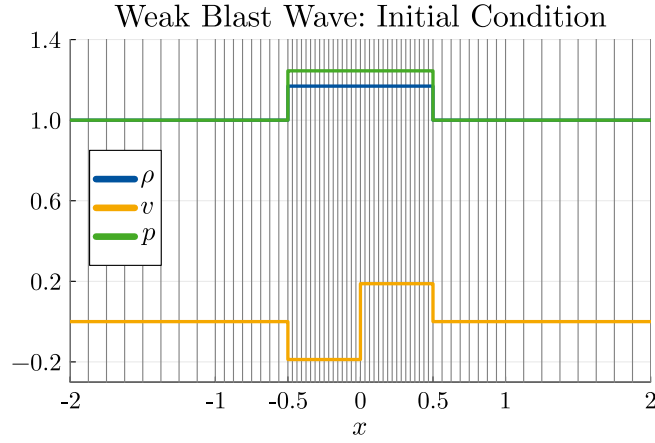


Figure B.20: Section 4.1.1: Initial hydrodynamic primal variables corresponding to the weak blast wave initial condition (4.1). The vertical lines depict the cell boundaries.

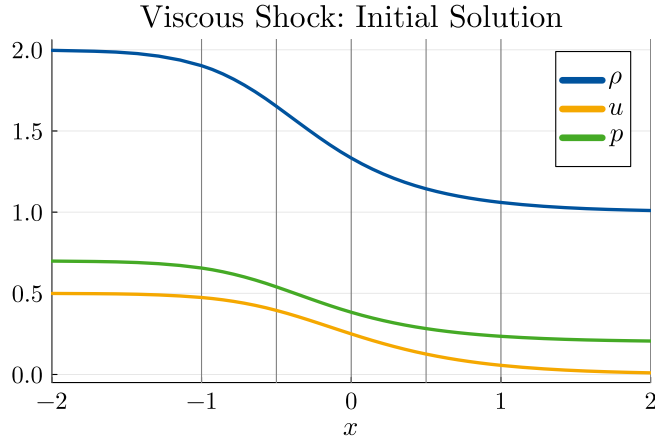


Figure B.21: Section 4.3.2: Initial primal variables corresponding to the viscous shock solution (4.13). The vertical lines depict the cell boundaries. Here, the coarsest mesh used in the convergence study with six cells only and  $k = 3$  solution polynomials is shown.

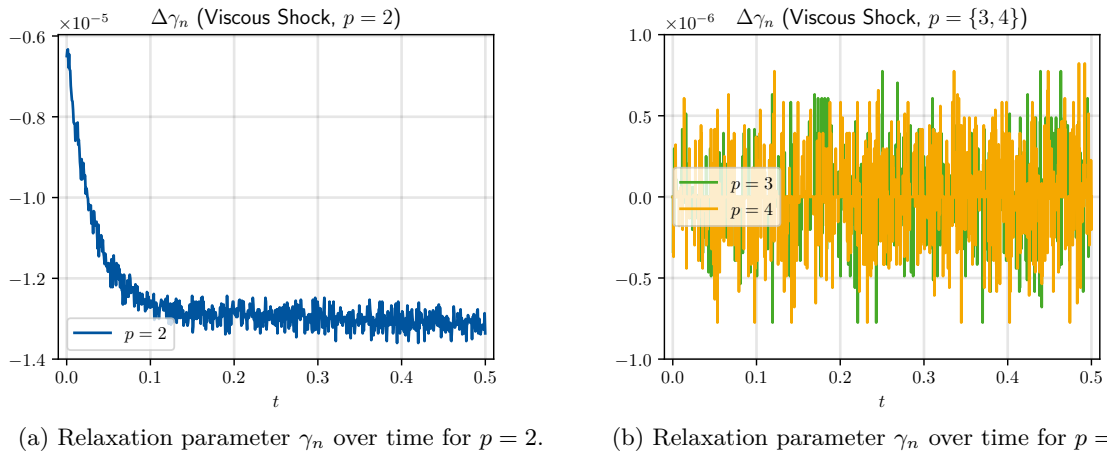


Figure B.22: Section 4.3.2: Evolution of the relaxation parameter  $\gamma_n$  for the viscous shock convergence testcase with  $N = 24$  grid cells for  $p = 2$  (Fig. B.22a) and  $p = 3, 4$  (Fig. B.22b) P-ERRK schemes. In the plots above, the deviation from unity, i.e.,  $\Delta\gamma_n := \gamma_n - 1$  is shown.

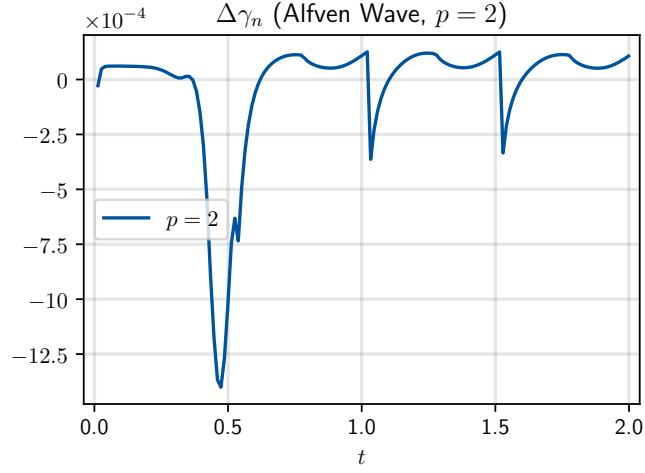
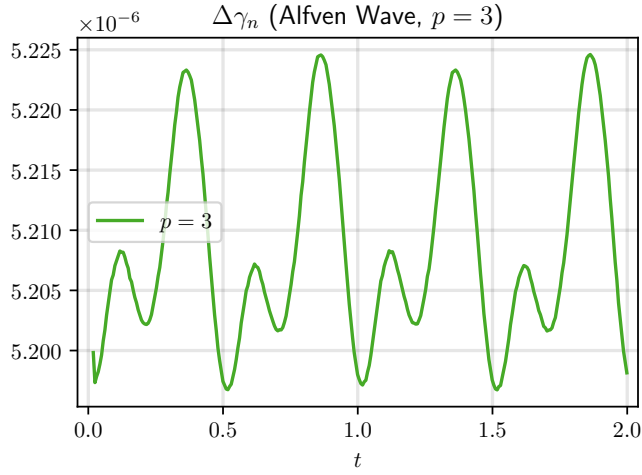
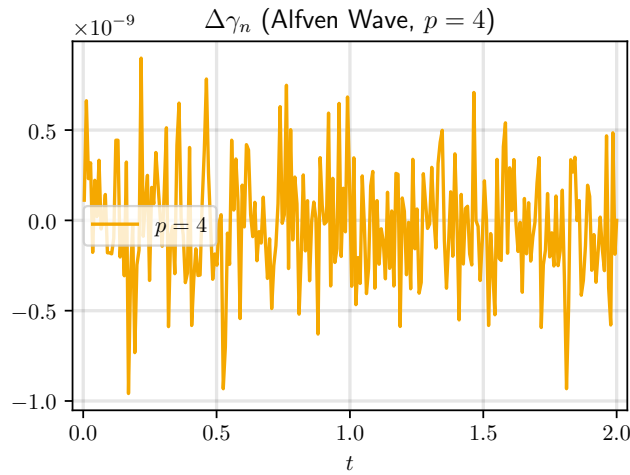
(a) Relaxation parameter  $\gamma_n$  over time for  $p = 2$ .(b) Relaxation parameter  $\gamma_n$  over time for  $p = 3$ .(c) Relaxation parameter  $\gamma_n$  over time for  $p = 4$ .

Figure B.23: Section 4.3.3: Evolution of the relaxation parameter  $\gamma_n$  for the Alfvén wave convergence test case with  $N = 64$  grid cells for  $p = 2$  (Fig. B.23a),  $p = 3$  (Fig. B.23b), and  $p = 4$  (Fig. B.23c) P-ERRK schemes. In the plots above, the deviation from unity, i.e.,  $\Delta\gamma_n := \gamma_n - 1$  is shown.

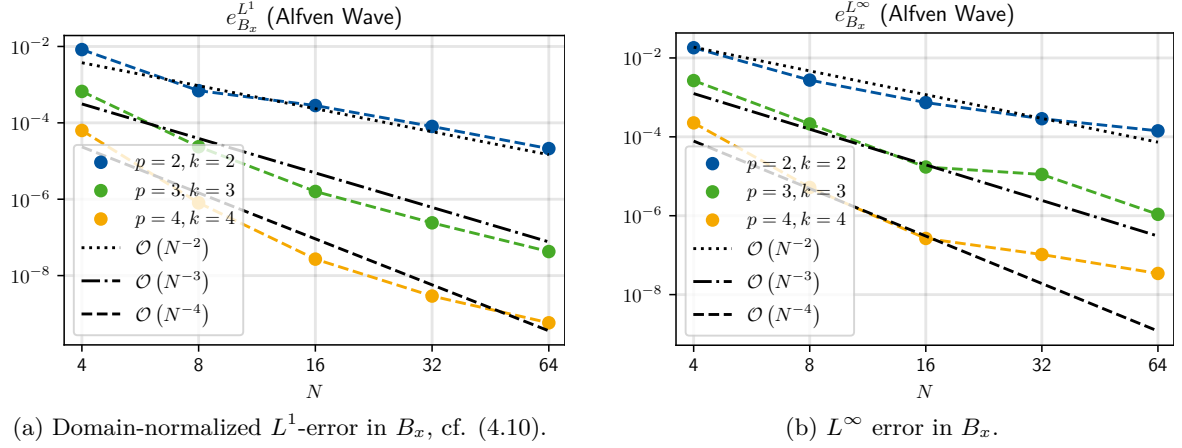


Figure B.24: Section 4.3.3:  $L^1$  (Fig. 8a) and  $L^\infty$  (Fig. 8b) errors of the  $x$ -component of the magnetic field  $B_x$  for the Alfvén wave testcase at  $t_f = 4.0$  for  $p = 2, 3, 4$  P-ERRK schemes assigned in a round-robin fashion.

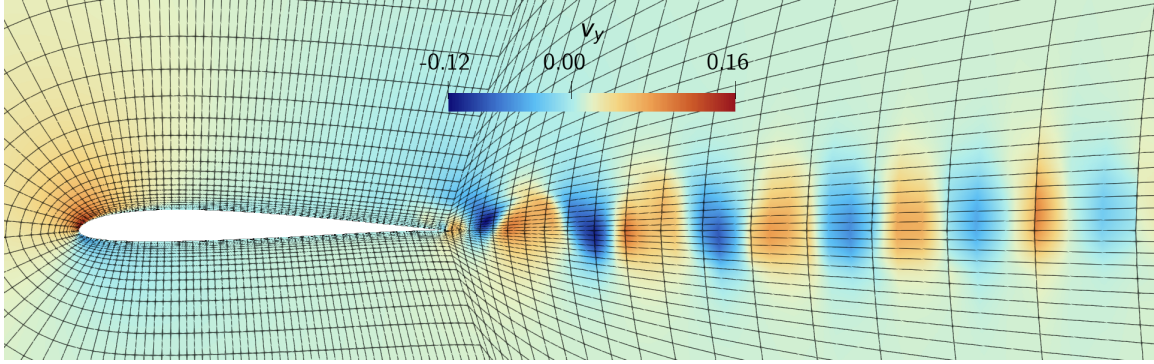


Figure B.25: Section 5.1: Vertical velocity  $v_y$  around the SD7003 airfoil and wake at  $t = 30t_c$  s.

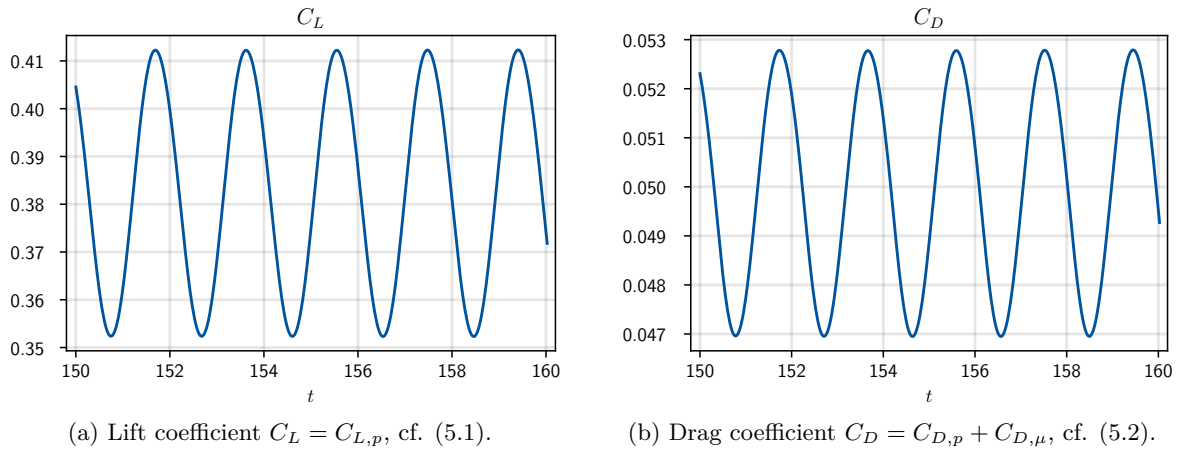


Figure B.26: Section 5.1: Unsteady lift (B.26a) and drag coefficient (B.26b) for the SD7003 airfoil over the  $[30t_c, 32t_c]$  time interval.

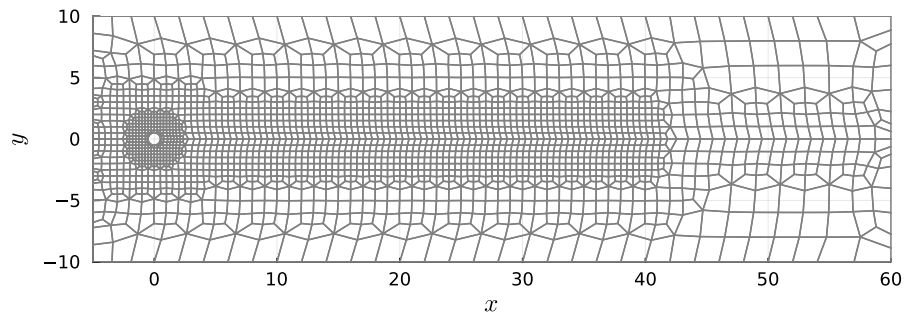
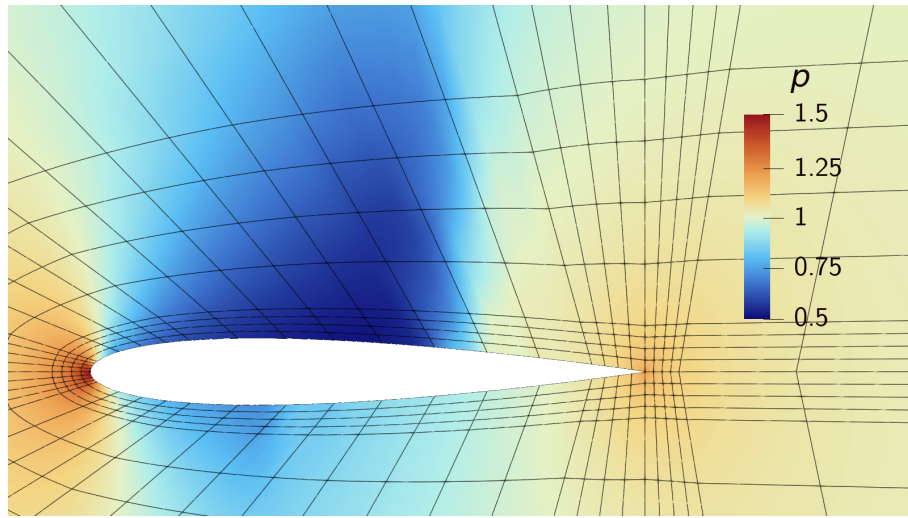
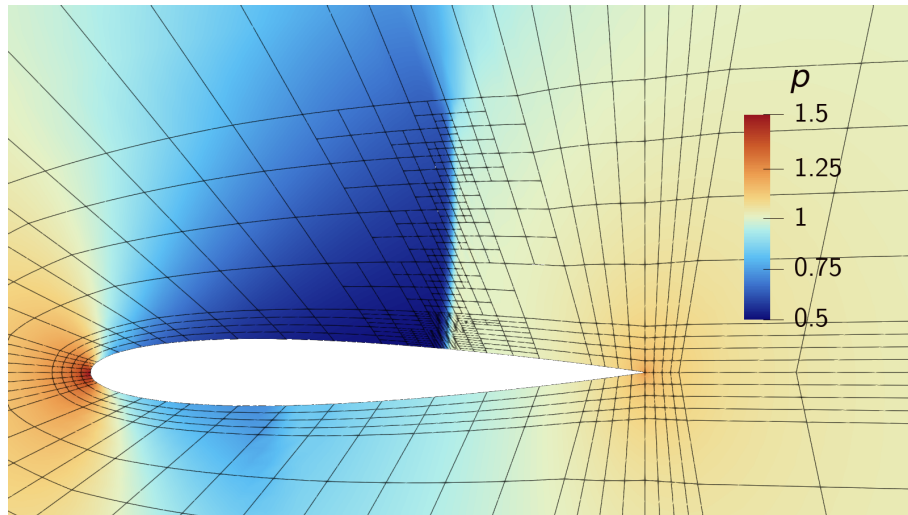


Figure B.27: Section 5.2: Non-uniform,  $y = 0$  symmetric computational mesh composed of 2258 quadrilateral elements employed for the VRMHD flow past a cylinder.



(a) NACA0012 airfoil simulation on static mesh until  $t_f = 100$ .



(b) NACA0012 airfoil simulation on adaptively refined mesh until  $t_f = 200$ .

Figure B.28: Section 5.3: Pressure  $p$  at times  $t_f = 100$  for the static mesh, cf. Fig. B.28a, and  $t_f = 200$  on dynamically adapted mesh, cf. Fig. B.28b for the transonic inviscid flow over the NACA0012 airfoil. The simulation with AMR is restarted from the static simulation at  $t_f = 100$  and then evolved until the final time  $t_f = 200$ .

## References

- [1] O. A. Oleĭnik, Uniqueness and stability of the generalized solution of the Cauchy problem for a quasi-linear equation, *Russian Mathematical Surveys* 14 (1959) 165–170. doi:10.1090/trans2/033/09, English translation: *Amer. Math. Soc. Trans., Series 2*, Volume 33, Pages 285–290.
- [2] P. D. Lax, Hyperbolic systems of conservation laws II, *Communications on Pure and Applied Mathematics* 10 (1957) 537–566. doi:10.1002/cpa.3160100406.
- [3] S. N. Kružkov, First order quasilinear equations in several independent variables, *Mathematics of the USSR-Sbornik* 10 (1970) 217. doi:10.1070/SM1970v010n02ABEH002156.
- [4] P. D. Lax, Hyperbolic systems of conservation laws and the mathematical theory of shock waves, *CBMS-NSF Regional Conference Series in Applied Mathematics*, SIAM, 1973. doi:10.1137/1.9781611970562.
- [5] C. M. Dafermos, *Hyperbolic conservation laws in continuum physics*, *Grundlehren der mathematischen Wissenschaften*, 4 ed., Springer Berlin, Heidelberg, 2005. doi:10.1007/978-3-662-49451-6.
- [6] R. Courant, K. O. Friedrichs, *Supersonic flow and shock waves*, volume 21 of *Applied Mathematical Sciences*, 1 ed., Springer New York, NY, 1976.
- [7] G. J. Gassner, A. R. Winters, D. A. Kopriva, Split form nodal discontinuous Galerkin schemes with summation-by-parts property for the compressible Euler equations, *Journal of Computational Physics* 327 (2016) 39–66. doi:10.1016/j.jcp.2016.09.013.
- [8] B. Sjögren, H. Yee, High order entropy conservative central schemes for wide ranges of compressible gas dynamics and MHD flows, *Journal of Computational Physics* 364 (2018) 153–185. doi:10.1016/j.jcp.2018.02.003.
- [9] J. Manzanero, G. Rubio, D. A. Kopriva, E. Ferrer, E. Valero, An entropy-stable discontinuous Galerkin approximation for the incompressible Navier–Stokes equations with variable density and artificial compressibility, *Journal of Computational Physics* 408 (2020) 109241. doi:10.1016/j.jcp.2020.109241.
- [10] D. Rojas, R. Boukharfane, L. Dalcin, D. C. D. R. Fernández, H. Ranocha, D. E. Keyes, M. Parsani, On the robustness and performance of entropy stable collocated discontinuous Galerkin methods, *Journal of Computational Physics* 426 (2021) 109891. doi:10.1016/j.jcp.2020.109891.
- [11] J. Chan, H. Ranocha, A. M. Rueda-Ramírez, G. Gassner, T. Warburton, On the entropy projection and the robustness of high order entropy stable discontinuous Galerkin schemes for under-resolved flows, *Frontiers in Physics* 10 (2022) 898028. doi:10.3389/fphy.2022.898028.
- [12] E. Tadmor, Entropy conservative finite element schemes, in: T. E. Tezduyar, T. J. R. Hughes (Eds.), *Proceedings of the winter annual meeting of the American Society of Mechanical Engineering*, volume 78, 1986, pp. 149–158.
- [13] E. Tadmor, The numerical viscosity of entropy stable schemes for systems of conservation laws. i, *Mathematics of Computation* 49 (1987) 91–103. doi:10.1090/S0025-5718-1987-0890255-3.



- [14] U. S. Fjordholm, S. Mishra, E. Tadmor, Arbitrarily high-order accurate entropy stable essentially nonoscillatory schemes for systems of conservation laws, *SIAM Journal on Numerical Analysis* 50 (2012) 544–573. doi:10.1137/110836961.
- [15] T. C. Fisher, M. H. Carpenter, High-order entropy stable finite difference schemes for nonlinear conservation laws: Finite domains, *Journal of Computational Physics* 252 (2013) 518–557. doi:10.1016/j.jcp.2013.06.014.
- [16] G. J. Gassner, A skew-symmetric discontinuous Galerkin spectral element discretization and its relation to SBP-SAT finite difference methods, *SIAM Journal on Scientific Computing* 35 (2013) A1233–A1253. doi:10.1137/120890144.
- [17] M. H. Carpenter, M. Parsani, E. J. Nielsen, T. C. Fisher, Towards an entropy stable spectral element framework for computational fluid dynamics, in: 54th AIAA Aerospace Sciences Meeting, 2016, p. 1058. doi:10.2514/6.2016-1058.
- [18] J. S. Hesthaven, T. Warburton, Nodal discontinuous Galerkin methods: Algorithms, analysis, and applications, *Texts in Applied Mathematics*, 1 ed., Springer New York, NY, 2007. doi:10.1007/978-0-387-72067-8.
- [19] K. Black, A conservative spectral element method for the approximation of compressible fluid flow, *Kybernetika* 35 (1999) 133–146.
- [20] D. A. Kopriva, Implementing spectral methods for partial differential equations: Algorithms for scientists and engineers, *Scientific Computation (SCIENTCOMP)*, 1 ed., Springer Science & Business Media, 2009. doi:10.1007/978-90-481-2261-5.
- [21] T. Chen, C.-W. Shu, Entropy stable high order discontinuous Galerkin methods with suitable quadrature rules for hyperbolic conservation laws, *Journal of Computational Physics* 345 (2017) 427–461. doi:10.1016/j.jcp.2017.05.025.
- [22] J. Chan, On discretely entropy conservative and entropy stable discontinuous Galerkin methods, *Journal of Computational Physics* 362 (2018) 346–374. doi:10.1016/j.jcp.2018.02.033.
- [23] P. Chandrashekar, Kinetic energy preserving and entropy stable finite volume schemes for compressible Euler and Navier-Stokes equations, *Communications in Computational Physics* 14 (2013) 12521286. doi:10.4208/cicp.170712.010313a.
- [24] A. R. Winters, G. J. Gassner, Affordable, entropy conserving and entropy stable flux functions for the ideal MHD equations, *Journal of Computational Physics* 304 (2016) 72–108. doi:10.1016/j.jcp.2015.09.055.
- [25] H. Ranocha, Comparison of some entropy conservative numerical fluxes for the Euler equations, *Journal of Scientific Computing* 76 (2018) 216–242. doi:10.1007/s10915-017-0618-1.
- [26] H. Ranocha, Entropy conserving and kinetic energy preserving numerical methods for the euler equations using summation-by-parts operators, in: S. J. Sherwin, D. Moxey, J. Peiró, P. E. Vincent, C. Schwab (Eds.), *Spectral and High Order Methods for Partial Differential Equations ICOSAHOM 2018*, Springer International Publishing, 2020, pp. 525–535. doi:10.1007/978-3-030-39647-3\_42.
- [27] E. Tadmor, Entropy stability theory for difference approximations of nonlinear conservation laws and related time-dependent problems, *Acta Numerica* 12 (2003) 451–512. doi:10.1017/S0962492902000156.

- [28] A. Hildebrand, S. Mishra, Entropy stable shock capturing space–time discontinuous Galerkin schemes for systems of conservation laws, *Numerische Mathematik* 126 (2014) 103–151. doi:10.1007/s00211-013-0558-0.
- [29] L. Friedrich, G. Schnücke, A. R. Winters, D. C. D. R. Fernández, G. J. Gassner, M. H. Carpenter, Entropy stable space–time discontinuous Galerkin schemes with summation-by-parts property for hyperbolic conservation laws, *Journal of Scientific Computing* 80 (2019) 175–222. doi:10.1007/s10915-019-00933-2.
- [30] E. Gaburro, P. Öffner, M. Ricchiuto, D. Torlo, High order entropy preserving ADER-DG schemes, *Applied Mathematics and Computation* 440 (2023) 127644. doi:10.1016/j.amc.2022.127644.
- [31] B. Cockburn, C.-W. Shu, Runge–Kutta discontinuous Galerkin methods for convection-dominated problems, *Journal of Scientific Computing* 16 (2001) 173–261. doi:10.1023/A:1012873910884.
- [32] E. Hairer, C. Lubich, G. Wanner, *Geometric numerical integration*, Springer Series in Computational Mathematics, 2 ed., Springer Berlin, Heidelberg, 2006. doi:10.1007/3-540-30666-8.
- [33] M. Calvo, M. Laburta, J. Montijano, L. Rández, Projection methods preserving Lyapunov functions, *BIT Numerical Mathematics* 50 (2010) 223–241. doi:10.1007/s10543-010-0259-3.
- [34] H. Kojima, Invariants preserving schemes based on explicit Runge–Kutta methods, *BIT Numerical Mathematics* 56 (2016) 1317–1337. doi:10.1007/s10543-016-0608-y.
- [35] M. R. Najafian, B. C. Vermeire, Quasi-orthogonal Runge-Kutta projection methods, *Journal of Computational Physics* 530 (2025) 113917. doi:10.1016/j.jcp.2025.113917.
- [36] M. Calvo, D. Hernández-Abreu, J. I. Montijano, L. Rández, On the preservation of invariants by explicit Runge–Kutta methods, *SIAM Journal on Scientific Computing* 28 (2006) 868–885. doi:10.1137/04061979X.
- [37] D. I. Ketcheson, Relaxation Runge–Kutta methods: Conservation and stability for inner-product norms, *SIAM Journal on Numerical Analysis* 57 (2019) 2850–2870. doi:10.1137/19M1263662.
- [38] H. Ranocha, M. Sayyari, L. Dalcin, M. Parsani, D. I. Ketcheson, Relaxation Runge–Kutta methods: Fully discrete explicit entropy-stable schemes for the compressible Euler and Navier–Stokes equations, *SIAM Journal on Scientific Computing* 42 (2020) A612–A638. doi:10.1137/19M1263480.
- [39] S. Kang, E. M. Constantinescu, Entropy–preserving and entropy–stable relaxation IMEX and multirate time–stepping methods, *Journal of Scientific Computing* 93 (2022) 23. doi:10.1007/s10915-022-01982-w.
- [40] H. Ranocha, L. Dalcin, M. Parsani, Fully discrete explicit locally entropy-stable schemes for the compressible Euler and Navier–Stokes equations, *Computers & Mathematics with Applications* 80 (2020) 1343–1359. doi:10.1016/j.camwa.2020.06.016.
- [41] H. Ranocha, L. Lóczi, D. I. Ketcheson, General relaxation methods for initial-value problems with application to multistep schemes, *Numerische Mathematik* 146 (2020) 875–906. doi:10.1007/s00211-020-01158-4.

- [42] J. M. Sanz-Serna, An explicit finite-difference scheme with exact conservation properties, *Journal of Computational Physics* 47 (1982) 199–210. doi:10.1016/0021-9991(82)90074-2.
- [43] J. Sanz-Serna, V. Manoranjan, A method for the integration in time of certain partial differential equations, *Journal of Computational Physics* 52 (1983) 273–289. doi:10.1016/0021-9991(83)90031-1.
- [44] K. Dekker, J. G. Verwer, Stability of Runge-Kutta methods for stiff nonlinear differential equations, *CWI monographs* 2 (1984) 307.
- [45] B. C. Vermeire, Paired explicit Runge-Kutta schemes for stiff systems of equations, *Journal of Computational Physics* 393 (2019) 465–483. doi:10.1016/j.jcp.2019.05.014.
- [46] S. H. Nasab, B. C. Vermeire, Third-order paired explicit Runge-Kutta schemes for stiff systems of equations, *Journal of Computational Physics* 468 (2022) 111470. doi:10.1016/j.jcp.2022.111470.
- [47] D. Doebling, L. Christmann, M. Schlottke-Lakemper, G. J. Gassner, M. Torrilhon, Fourth-order paired-explicit Runge-Kutta methods, *arXiv preprint arXiv:2408.05470* (2024). doi:10.48550/arXiv.2408.05470.
- [48] E. M. Constantinescu, A. Sandu, Multirate timestepping methods for hyperbolic conservation laws, *Journal of Scientific Computing* 33 (2007) 239–278. doi:10.1007/s10915-007-9151-y.
- [49] G. J. Gassner, A. R. Winters, D. A. Kopriva, A well balanced and entropy conservative discontinuous Galerkin spectral element method for the shallow water equations, *Applied Mathematics and Computation* 272 (2016) 291–308. doi:10.1016/j.amc.2015.07.014.
- [50] M. J. Castro, U. S. Fjordholm, S. Mishra, C. Parés, Entropy conservative and entropy stable schemes for nonconservative hyperbolic systems, *SIAM Journal on Numerical Analysis* 51 (2013) 1371–1391. doi:10.1137/110845379.
- [51] B. C. Vermeire, Embedded paired explicit Runge-Kutta schemes, *Journal of Computational Physics* 487 (2023) 112159. doi:10.1016/j.jcp.2023.112159.
- [52] P. Rentrop, Partitioned Runge-Kutta methods with stiffness detection and stepsize control, *Numerische Mathematik* 47 (1985) 545–564. doi:10.1007/BF01389456.
- [53] J. Bruder, K. Strehmel, R. Weiner, Partitioned adaptive Runge-Kutta methods for the solution of nonstiff and stiff systems, *Numerische Mathematik* 52 (1988) 621–638. doi:10.1007/BF01395815.
- [54] M. Günther, A. Kvaernø, P. Rentrop, Multirate partitioned Runge-Kutta methods, *BIT Numerical Mathematics* 41 (2001) 504–514. doi:10.1023/A:1021967112503.
- [55] E. Hairer, G. Wanner, S. P. Nørsett, Solving Ordinary Differential Equations I: Nonstiff Problems, *Springer Series in Computational Mathematics*, 2 ed., Springer Berlin, Heidelberg, 1993. doi:10.1007/978-3-540-78862-1.
- [56] M. J. Berger, J. Olinger, Adaptive mesh refinement for hyperbolic partial differential equations, *Journal of Computational Physics* 53 (1984) 484–512. doi:10.1016/0021-9991(84)90073-1.
- [57] C. Dawson, R. Kirby, High resolution schemes for conservation laws with locally varying time steps, *SIAM Journal on Scientific Computing* 22 (2001) 2256–2281. doi:10.1137/S1064827500367737.

- [58] F. Lörcher, G. Gassner, C.-D. Munz, A discontinuous Galerkin scheme based on a space–time expansion. I. inviscid compressible flow in one space dimension, *Journal of Scientific Computing* 32 (2007) 175–199. doi:10.1007/s10915-007-9128-x.
- [59] M. Dumbser, M. Käser, E. F. Toro, An arbitrary high-order discontinuous Galerkin method for elastic waves on unstructured meshes – V. Local time stepping and p-adaptivity, *Geophysical Journal International* 171 (2007) 695–717. doi:10.1111/j.1365-246X.2007.03427.x.
- [60] L. Krivodonova, An efficient local time-stepping scheme for solution of nonlinear conservation laws, *Journal of Computational Physics* 229 (2010) 8537–8551. doi:10.1016/j.jcp.2010.07.037.
- [61] M. J. Grote, M. Mehlin, T. Mitkova, Runge–Kutta-based explicit local time-stepping methods for wave propagation, *SIAM Journal on Scientific Computing* 37 (2015) A747–A775. doi:10.1137/140958293.
- [62] J. Luther, Y. Wang, P. Jenny, Adaptive conservative time integration for unsteady compressible flow, *Journal of Computational Physics* 517 (2024) 113324. doi:10.1016/j.jcp.2024.113324.
- [63] D. Ketcheson, A. Ahmadi, Optimal stability polynomials for numerical integration of initial value problems, *Communications in Applied Mathematics and Computational Science* 7 (2013) 247–271. doi:10.2140/camcos.2012.7.247.
- [64] D. Doehring, G. J. Gassner, M. Torrilhon, Many-stage optimal stabilized Runge-Kutta methods for hyperbolic partial differential equations, *Journal of Scientific Computing* 99 (2024). doi:10.1007/s10915-024-02478-5.
- [65] G. Wanner, E. Hairer, Solving ordinary differential equations II: Stiff and Differential-Algebraic Problems, volume 375 of *Springer Series in Computational Mathematics*, 2 ed., Springer Berlin, Heidelberg, 1996. doi:10.1007/978-3-642-05221-7.
- [66] V. Rusanov, The calculation of the interaction of non-stationary shock waves and obstacles, *USSR Computational Mathematics and Mathematical Physics* 1 (1962) 304–320. doi:10.1016/0041-5553(62)90062-9.
- [67] W. Hundsdorfer, D. I. Ketcheson, I. Savostianov, Error analysis of explicit partitioned Runge-Kutta schemes for conservation laws, *Journal of Scientific Computing* 63 (2015) 633–653. doi:10.1007/s10915-014-9906-1.
- [68] D. Doehring, M. Schlottke-Lakemper, G. J. Gassner, M. Torrilhon, Multirate time-integration based on dynamic ODE partitioning through adaptively refined meshes for compressible fluid dynamics, *Journal of Computational Physics* 514 (2024) 113223. doi:10.1016/j.jcp.2024.113223.
- [69] C.-W. Shu, S. Osher, Efficient implementation of essentially non-oscillatory shock-capturing schemes, *Journal of Computational Physics* 77 (1988) 439–471. doi:10.1016/0021-9991(88)90177-5.
- [70] S. Gottlieb, C.-W. Shu, E. Tadmor, Strong stability-preserving high-order time discretization methods, *SIAM Review* 43 (2001) 89–112. doi:10.1137/S003614450036757X.
- [71] S. Gottlieb, C.-W. Shu, Total variation diminishing Runge-Kutta schemes, *Mathematics of Computation* 67 (1998) 73–85. doi:10.1090/S0025-5718-98-00913-2.

- [72] S. Forth, A second order accurate, space-time limited, BDF scheme for the linear advection equation, in: E. F. Toro (Ed.), *Godunov Methods: Theory and Applications*, Springer, New York, NY, 2001, pp. 335–342. doi:10.1007/978-1-4615-0663-8\_35.
- [73] K. Duraisamy, J. D. Baeder, J.-G. Liu, Concepts and application of time-limiters to high resolution schemes, *Journal of Scientific Computing* 19 (2003) 139–162. doi:10.1023/A:1025395707090.
- [74] K. Duraisamy, J. D. Baeder, Implicit scheme for hyperbolic conservation laws using nonoscillatory reconstruction in space and time, *SIAM Journal on Scientific Computing* 29 (2007) 2607–2620. doi:10.1137/070683271.
- [75] T. Arbogast, C.-S. Huang, X. Zhao, D. N. King, A third order, implicit, finite volume, adaptive Runge–Kutta WENO scheme for advection–diffusion equations, *Computer Methods in Applied Mechanics and Engineering* 368 (2020) 113155.
- [76] G. Puppo, M. Semplice, G. Visconti, Quinpi: integrating conservation laws with CWENO implicit methods, *Communications on Applied Mathematics and Computation* 5 (2023) 343–369. doi:10.1007/s42967-021-00171-0.
- [77] G. Puppo, M. Semplice, G. Visconti, Quinpi: Integrating stiff hyperbolic systems with implicit high order finite volume schemes, *arXiv preprint arXiv:2307.14685* (2023). doi:10.48550/arXiv.2307.14685.
- [78] A. Harten, High resolution schemes for hyperbolic conservation laws, *Journal of Computational Physics* 135 (1997) 260–278. doi:10.1006/jcph.1997.5713.
- [79] A. M. Rueda-Ramírez, G. J. Gassner, A subcell finite volume positivity-preserving limiter for DGSEM discretizations of the Euler equations, *arXiv preprint arXiv:2102.06017* (2021). doi:10.48550/arXiv.2102.06017.
- [80] B. Einfeldt, On Godunov-type methods for gas dynamics, *SIAM Journal on Numerical Analysis* 25 (1988) 294–318. doi:10.1137/0725021.
- [81] S. Hennemann, A. M. Rueda-Ramírez, F. J. Hindenlang, G. J. Gassner, A provably entropy stable subcell shock capturing approach for high order split form DG for the compressible Euler equations, *Journal of Computational Physics* 426 (2021) 109935. doi:10.1016/j.jcp.2020.109935.
- [82] H. Ranocha, M. Schlottke-Lakemper, A. R. Winters, E. Faulhaber, J. Chan, G. Gassner, Adaptive numerical simulations with Trixi.jl: A case study of Julia for scientific computing, *Proceedings of the JuliaCon Conferences* 1 (2022) 77. doi:10.21105/jcon.00077. arXiv:2108.06476.
- [83] M. Schlottke-Lakemper, A. R. Winters, H. Ranocha, G. Gassner, A purely hyperbolic discontinuous Galerkin approach for self-gravitating gas dynamics, *Journal of Computational Physics* 442 (2021) 110467. doi:10.1016/j.jcp.2021.110467. arXiv:2008.10593.
- [84] M. Schlottke-Lakemper, G. Gassner, H. Ranocha, A. R. Winters, J. Chan, Trixi.jl: Adaptive high-order numerical simulations of hyperbolic PDEs in Julia, <https://github.com/trixi-framework/Trixi.jl>, 2021. doi:10.5281/zenodo.3996439.
- [85] J. Bezanson, A. Edelman, S. Karpinski, V. B. Shah, Julia: A fresh approach to numerical computing, *SIAM review* 59 (2017) 65–98. doi:10.1137/141000671.

- [86] D. Doehring, H. Ranocha, M. Torrilhon, Reproducibility repository for "paired explicit relaxation runge-kutta methods: Entropy conservative/stable high-order optimized multi-rate time integration", <https://github.com/DanielDoehring/paper-2025-perrk>, 2025. doi:10.5281/zenodo.15601890.
- [87] F. Hindenlang, G. Gassner, A new entropy conservative two-point flux for ideal MHD equations derived from first principles, Talk presented at HONOM: High Order Numerical Methods for Evolutionary PDEs (2019). URL: [https://eventos.emagister.com/\\_files/\\_event/\\_13680/\\_editorFiles/file/Abstracts/abstract\\_hindenlang.pdf](https://eventos.emagister.com/_files/_event/_13680/_editorFiles/file/Abstracts/abstract_hindenlang.pdf).
- [88] Z. J. Wang, K. Fidkowski, R. Abgrall, F. Bassi, D. Caraeni, A. Cary, H. Deconinck, R. Hartmann, K. Hillewaert, H. T. Huynh, et al., High-order CFD methods: Current status and perspective, *International Journal for Numerical Methods in Fluids* 72 (2013) 811–845. doi:10.1002/flid.3767.
- [89] E. F. Toro, M. Spruce, W. Speares, Restoration of the contact surface in the HLL-Riemann solver, *Shock Waves* 4 (1994) 25–34. doi:10.1007/BF01414629.
- [90] D. I. Ketcheson, Highly efficient strong stability-preserving Runge-Kutta methods with low-storage implementations, *SIAM Journal on Scientific Computing* 30 (2008) 2113–2136. doi:10.1137/07070485X.
- [91] C. Rackauckas, Q. Nie, Differentialequations.jl – a performant and feature-rich ecosystem for solving differential equations in julia, *The Journal of Open Research Software* 5 (2017). URL: <https://app.dimensions.ai/details/publication/pub.1085583166andhttp://openresearchsoftware.metajnl.com/articles/10.5334/jors.151/galley/245/download/>. doi:10.5334/jors.151.
- [92] R. Becker, Stosswelle und Detonation, *Zeitschrift für Physik* 8 (1922) 321–362. doi:10.1007/BF01329605, in German. English translations: Impact waves and detonation. Part I. <https://ntrs.nasa.gov/citations/19930090862> Part II. <https://ntrs.nasa.gov/citations/19930090863>.
- [93] M. Morduchow, P. A. Libby, On a complete solution of the one-dimensional flow equations of a viscous, heat-conducting, compressible gas, *Journal of the Aeronautical Sciences* 16 (1949) 674–684. doi:10.2514/8.11882.
- [94] L. G. Margolin, J. M. Reisner, P. M. Jordan, Entropy in self-similar shock profiles, *International Journal of Non-Linear Mechanics* 95 (2017) 333–346. doi:10.1016/j.ijnonlinmec.2017.07.003.
- [95] C.-D. Munz, P. Omnes, R. Schneider, E. Sonnendrücker, U. Voss, Divergence correction techniques for Maxwell solvers based on a hyperbolic model, *Journal of Computational Physics* 161 (2000) 484–511. doi:10.1006/jcph.2000.6507.
- [96] A. Dedner, F. Kemm, D. Kröner, C.-D. Munz, T. Schnitzer, M. Wesenberg, Hyperbolic divergence cleaning for the MHD equations, *Journal of Computational Physics* 175 (2002) 645–673. doi:10.1006/jcph.2001.6961.
- [97] D. Derigs, A. R. Winters, G. J. Gassner, S. Walch, M. Böhm, Ideal GLM-MHD: About the entropy consistent nine-wave magnetic field divergence diminishing ideal magnetohydrodynamics equations, *Journal of Computational Physics* 364 (2018) 420–467. doi:10.1016/j.jcp.2018.03.002.
- [98] D. A. Kopriva, A conservative staggered-grid Chebyshev multidomain method for compressible flows. II. A semi-structured method, *Journal of Computational Physics* 128 (1996) 475–488. doi:10.1006/jcph.1996.0225.

- [99] J. Chan, M. J. Bencomo, D. C. Del Rey Fernández, Mortar-based entropy-stable discontinuous Galerkin methods on non-conforming quadrilateral and hexahedral meshes, *Journal of Scientific Computing* 89 (2021) 1–33. doi:10.1007/s10915-021-01652-3.
- [100] F. Bassi, S. Rebay, A high-order accurate discontinuous finite element method for the numerical solution of the compressible Navier–Stokes equations, *Journal of Computational Physics* 131 (1997) 267–279. doi:10.1006/jcph.1996.5572.
- [101] G. J. Gassner, A. R. Winters, F. J. Hindenlang, D. A. Kopriva, The BR1 scheme is stable for the compressible Navier–Stokes equations, *Journal of Scientific Computing* 77 (2018) 154–200. doi:10.1007/s10915-018-0702-1.
- [102] B. Cockburn, C.-W. Shu, The local discontinuous Galerkin method for time-dependent convection-diffusion systems, *SIAM journal on numerical analysis* 35 (1998) 2440–2463. doi:10.1137/S0036142997316712.
- [103] B. Cockburn, B. Dong, An analysis of the minimal dissipation local discontinuous Galerkin method for convection–diffusion problems, *Journal of Scientific Computing* 32 (2007) 233–262. doi:10.1007/s10915-007-9130-3.
- [104] M. Böhm, A. R. Winters, G. J. Gassner, D. Derigs, F. Hindenlang, J. Saur, An entropy stable nodal discontinuous Galerkin method for the resistive MHD equations. Part I: Theory and numerical verification, *Journal of Computational Physics* 422 (2020) 108076. doi:10.1016/j.jcp.2018.06.027.
- [105] T. Warburton, G. E. Karniadakis, A discontinuous Galerkin method for the viscous MHD equations, *Journal of computational Physics* 152 (1999) 608–641. doi:10.1006/jcph.1999.6248.
- [106] K. G. Powell, P. L. Roe, T. J. Linde, T. I. Gombosi, D. L. De Zeeuw, A solution-adaptive upwind scheme for ideal magnetohydrodynamics, *Journal of Computational Physics* 154 (1999) 284–309. doi:10.1006/jcph.1999.6299.
- [107] G. Tóth, The  $\text{div}(\mathbf{b})=0$  constraint in shock-capturing magnetohydrodynamics codes, *Journal of Computational Physics* 161 (2000) 605–652. doi:10.1006/jcph.2000.6519.
- [108] D. Derigs, A. R. Winters, G. J. Gassner, S. Walch, A novel high-order, entropy stable, 3D AMR MHD solver with guaranteed positive pressure, *Journal of Computational Physics* 317 (2016) 223–256. doi:10.1016/j.jcp.2016.04.048.
- [109] H. T. Huynh, Third international workshop on high-order CFD methods, <https://www1.grc.nasa.gov/research-and-engineering/hiocfd/>, 2015.
- [110] V. Schmitt, F. Charpin, Pressure distributions on the ONERA-M6 wing at transonic Mach numbers, Technical Report Advisory Report AR-138, AGARD, 1979. Experimental Data Base for Computer Program Assessment.
- [111] J. W. Slater, ONERA M6 Wing: Study #1: Demonstrate computation for a 3D wing flow, Technical Report, NASA John H. Glenn Research Center, 2002. URL: <https://www.grc.nasa.gov/www/wind/valid/m6wing/m6wing.html>.
- [112] G. Mengaldo, D. De Grazia, F. Witherden, A. Farrington, P. Vincent, S. Sherwin, J. Peiro, A guide to the implementation of boundary conditions in compact high-order methods for compressible aerodynamics, in: 7th AIAA Theoretical Fluid Mechanics Conference, 2014, p. 2923. doi:10.2514/6.2014-2923.

- [113] A. Uranga, P.-O. Persson, M. Drela, J. Peraire, Implicit large eddy simulation of transition to turbulence at low Reynolds numbers using a Discontinuous Galerkin method, *International Journal for Numerical Methods in Engineering* 87 (2011) 232–261. doi:10.1002/nme.3036.
- [114] M. R. López-Morales, J. R. Bull, J. Crabill, T. D. Economon, D. E. Manosalvas, J. Romero, A. Sheshadri, J. E. Watkins, D. M. Williams, F. Palacios, A. Jameson, Verification and validation of HiFiLES: a high-order LES unstructured solver on multi-GPU platforms, in: 32nd AIAA Applied Aerodynamics Conference, 2014, pp. 1–27. doi:10.2514/6.2014-3168.
- [115] K. Tselios, T. E. Simos, Runge–Kutta methods with minimal dispersion and dissipation for problems arising from computational acoustics, *Journal of Computational and Applied Mathematics* 175 (2005) 173–181. doi:10.1016/j.cam.2004.06.012.
- [116] C. A. Kennedy, M. H. Carpenter, R. M. Lewis, Low-storage, explicit Runge–Kutta schemes for the compressible Navier–Stokes equations, *Applied numerical mathematics* 35 (2000) 177–219. doi:10.1016/S0168-9274(99)00141-5.
- [117] P. Van der Houwen, Explicit Runge-Kutta formulas with increased stability boundaries, *Numerische Mathematik* 20 (1972) 149–164. doi:10.1007/BF01404404.
- [118] C. Crawford, G. Karniadakis, Control of external flows via electro-magnetic fields, in: *Processings of the 26th AIAA Fluid Dynamics Conference*, 1995, p. 12. doi:10.2514/6.1995-2185.
- [119] T. Weier, G. Gerbeth, G. Mutschke, E. Platacis, O. Lielausis, Experiments on cylinder wake stabilization in an electrolyte solution by means of electromagnetic forces localized on the cylinder surface, *Experimental Thermal and Fluid Science* 16 (1998) 84–91. doi:10.1016/S0894-1777(97)10008-5.
- [120] N. Kanaris, X. Albets, D. Grigoriadis, S. Kassinos, Three-dimensional numerical simulations of magnetohydrodynamic flow around a confined circular cylinder under low, moderate, and strong magnetic fields, *Physics of Fluids* 25 (2013). doi:10.1063/1.4811398.
- [121] D. A. Kopriva, A. R. Winters, M. Schlottke-Lakemper, J. A. Schoonover, H. Ranocha, HOHQMesh: An all quadrilateral/hexahedral unstructured mesh generator for high order elements, *Journal of Open Source Software* 9 (2024) 7476. doi:10.21105/joss.07476.
- [122] J. J. W. van der Vegt, H. van der Ven, Slip flow boundary conditions in discontinuous Galerkin discretizations of the Euler equations of gas dynamics, Technical Report NLR-TP-2002-300, National Aerospace Laboratory NLR, 2002. URL: <https://core.ac.uk/download/pdf/53034515.pdf>.
- [123] A. Harten, P. D. Lax, B. v. Leer, On upstream differencing and Godunov-type schemes for hyperbolic conservation laws, *SIAM Review* 25 (1983) 35–61. doi:10.1137/1025002.
- [124] S. F. Davis, Simplified second-order Godunov-type methods, *SIAM Journal on Scientific and Statistical Computing* 9 (1988) 445–473. doi:10.1137/0909030.
- [125] A. M. Rueda-Ramírez, S. Hennemann, F. J. Hindenlang, A. R. Winters, G. J. Gassner, An entropy stable nodal discontinuous Galerkin method for the resistive MHD equations. Part II: Subcell finite volume shock capturing, *Journal of Computational Physics* 444 (2021) 110580. doi:10.1016/j.jcp.2021.110580.



- [126] C. Geuzaine, J.-F. Remacle, Gmsh: A 3-d finite element mesh generator with built-in pre- and post-processing facilities, *International Journal for Numerical Methods in Engineering* 79 (2009) 1309–1331. doi:10.1002/nme.2579.
- [127] E. F. Toro, *Riemann solvers and numerical methods for fluid dynamics: A practical introduction*, 3 ed., Springer Berlin, Heidelberg, 2013. doi:10.1007/b79761.
- [128] G. G., E. van der Weide, M. Svård, M. H. Carpenter, K. Mattson, Case C1.2: Flow over the NACA0012 airfoil, [https://www1.grc.nasa.gov/wp-content/uploads/C1.2\\_Twente.pdf](https://www1.grc.nasa.gov/wp-content/uploads/C1.2_Twente.pdf), 2015.
- [129] J. A. Heyns, O. F. Oxtoby, A. Steenkamp, Modelling high-speed flow using a matrix-free coupled solver, in: *Proceedings of the 9th OpenFOAM Workshop*, Zagreb, Croatia, 2014, pp. 23–26. Mesh provided at [https://gitlab.com/hisa/hisa/-/blob/master/examples/oneram6/mesh/p3dMesh/m6wing.msh?ref\\_type=heads](https://gitlab.com/hisa/hisa/-/blob/master/examples/oneram6/mesh/p3dMesh/m6wing.msh?ref_type=heads).
- [130] T. D. Economon, F. Palacios, S. R. Copeland, T. W. Lukaczyk, J. J. Alonso, SU2: An open-source suite for multiphysics simulation and design, *AIAA Journal* 54 (2016) 828–846. doi:10.2514/1.J053813, inviscid ONERA M6 tutorial: [https://su2code.github.io/tutorials/Inviscid\\_ONERAM6/](https://su2code.github.io/tutorials/Inviscid_ONERAM6/).
- [131] A. Ralston, Runge-Kutta methods with minimum error bounds, *Mathematics of Computation* 16 (1962) 431–437. doi:10.2307/2003133.
- [132] J. Vassberg, M. Dehaan, M. Rivers, R. Wahls, Development of a common research model for applied CFD validation studies, in: *26th AIAA Applied Aerodynamics Conference*, 2008, p. 6919. doi:10.2514/6.2008-6919.
- [133] D. I. Ketcheson, L. Lóczi, M. Parsani, Internal error propagation in explicit Runge-Kutta methods, *SIAM Journal on Numerical Analysis* 52 (2014) 2227–2249. doi:10.1137/130936245.